

AWARD NUMBER: W81XWH-13-1-0341

TITLE: Delivery of Nanotethered Therapies to Brain Metastases of Primary Breast Cancer Using a Cellular Trojan Horse

PRINCIPAL INVESTIGATOR: Susan E Clare, MD, PhD

CONTRACTING ORGANIZATION: Northwestern University
Evanston, IL 60208

REPORT DATE: December 2016

TYPE OF REPORT: Final

PREPARED FOR: U.S. Army Medical Research and Materiel Command
Fort Detrick, Maryland 21702-5012

DISTRIBUTION STATEMENT: Approved for Public Release;
Distribution Unlimited

The views, opinions and/or findings contained in this report are those of the author(s) and should not be construed as an official Department of the Army position, policy or decision unless so designated by other documentation.

REPORT DOCUMENTATION PAGE				Form Approved OMB No. 0704-0188	
Public reporting burden for this collection of information is estimated to average 1 hour per response, including the time for reviewing instructions, searching existing data sources, gathering and maintaining the data needed, and completing and reviewing this collection of information. Send comments regarding this burden estimate or any other aspect of this collection of information, including suggestions for reducing this burden to Department of Defense, Washington Headquarters Services, Directorate for Information Operations and Reports (0704-0188), 1215 Jefferson Davis Highway, Suite 1204, Arlington, VA 22202-4302. Respondents should be aware that notwithstanding any other provision of law, no person shall be subject to any penalty for failing to comply with a collection of information if it does not display a currently valid OMB control number. PLEASE DO NOT RETURN YOUR FORM TO THE ABOVE ADDRESS.					
1. REPORT DATE December 2016		2. REPORT TYPE Final		3. DATES COVERED 15 Sep 2013 - 14 Sep 2016	
4. TITLE AND SUBTITLE Delivery of Nanotethered Therapies to Brain Metastases of Primary Breast Cancer Using a Cellular Trojan Horse				5a. CONTRACT NUMBER	
				5b. GRANT NUMBER W81XWH-13-1-0341	
				5c. PROGRAM ELEMENT NUMBER	
6. AUTHOR(S) Susan E Clare, MD, PhD E-Mail: susan.clare@northwestern.edu				5d. PROJECT NUMBER	
				5e. TASK NUMBER	
				5f. WORK UNIT NUMBER	
7. PERFORMING ORGANIZATION NAME(S) AND ADDRESS(ES) Northwestern University 633 Clark Street Evanston, IL 60208-0001				8. PERFORMING ORGANIZATION REPORT NUMBER	
9. SPONSORING / MONITORING AGENCY NAME(S) AND ADDRESS(ES) U.S. Army Medical Research and Materiel Command Fort Detrick, Maryland 21702-5012				10. SPONSOR/MONITOR'S ACRONYM(S)	
				11. SPONSOR/MONITOR'S REPORT NUMBER(S)	
12. DISTRIBUTION / AVAILABILITY STATEMENT Approved for Public Release; Distribution Unlimited					
13. SUPPLEMENTARY NOTES					
14. ABSTRACT The purpose of this work is to utilize monocyte/macrophage-enabled delivery, a novel therapeutic delivery system that we pioneered, to increase the effectiveness and decrease the toxicity of the treatment of intracranial metastases from primary breast cancer. Our objective in this proposal is to deliver therapeutics to brain metastases using a nanoshell (NS)-double-stranded DNA (dsDNA)-drug complex loaded within monocytes/macrophages. Once present within the metastasis, we aim to release the drug by transcranial irradiation at near-infrared (NIR) wavelengths. Our studies have provided fundamental information on a number of aspects of the delivery of therapeutics by NS and NSdsDNA. 1. DNA duplexes are released from the nanoshell surface differently depending on type of laser. 2. Hydrophobic therapeutics can be complexed to nanoshells using protein scaffolds. 3. The amount and distribution of near infrared (NIR) light able to be delivered through the skull and brain tissue have been estimated. 4. The use of CT to map skull geometry and determine bone density enables a better understanding of the attenuation/scattering of NIR.					
15. SUBJECT TERMS					
16. SECURITY CLASSIFICATION OF:			17. LIMITATION OF ABSTRACT Unclassified	18. NUMBER OF PAGES	19a. NAME OF RESPONSIBLE PERSON USAMRMC
a. REPORT Unclassified	b. ABSTRACT Unclassified	c. THIS PAGE Unclassified			19b. TELEPHONE NUMBER (include area code)

Table of Contents

	<u>Page</u>
1. Introduction.....	4
2. Keywords.....	4
3. Overall Project Summary.....	4-26
4. Key Research Accomplishments.....	26
5. Conclusion.....	27
6. Publications, Abstracts, and Presentations.....	28-29
7. Inventions, Patents and Licenses.....	29
8. Reportable Outcomes.....	29
9. Other Achievements.....	29-30
10. References.....	30-31
11. Appendices.....	32-65

1. INTRODUCTION: The blood-brain barrier renders the central nervous system a sanctuary site for disease. In the era prior to the development of effective systemic therapies this fact was not of much clinical relevance as most patients succumbed to visceral metastatic disease before their brain metastases became symptomatic. However, as systemic breast cancer therapies improve and are able to successfully control non-Central Nervous System disease, the brain is increasingly the first site of relapse. Both conventional chemotherapeutic agents and targeted monoclonal antibodies do not cross the blood-brain barrier (BBB) at concentrations sufficient to successfully treat metastatic disease. The objective of the proposed work is to use an active form of transport of therapeutics across the BBB; a transport mechanism that does not rely on passive diffusion or receptor-mediated transcytosis. We hypothesize that monocytes/macrophages are actively recruited to metastases by cytokines elaborated by the tumors and that these cells can be utilized to transport therapeutics directly to brain metastases of breast cancer. This hypothesis is supported by a pilot study we published that demonstrated delivery of fluorescent microspheres to brain metastases by macrophages in a mouse model [1]. Our objective in this proposal is to deliver a therapeutic, doxorubicin, to brain metastases using a nanoshell-double-stranded DNA (dsDNA)-drug complex loaded within monocytes/macrophages. Once present within the metastasis, we aim to release the drug by transcranial irradiation at near-infrared (NIR) wavelengths.

2. KEYWORDS: *Brain metastases, nanoshells, macrophage, monocyte, blood-brain barrier, photothermal therapy, light triggered release, Adriamycin, doxorubicin, metastatic breast cancer, Trojan horse*

3. OVERALL PROJECT SUMMARY: *Summarize the progress during appropriate reporting period (single annual or comprehensive final). This section of the report shall be in direct alignment with respect to each task outlined in the approved SOW.*

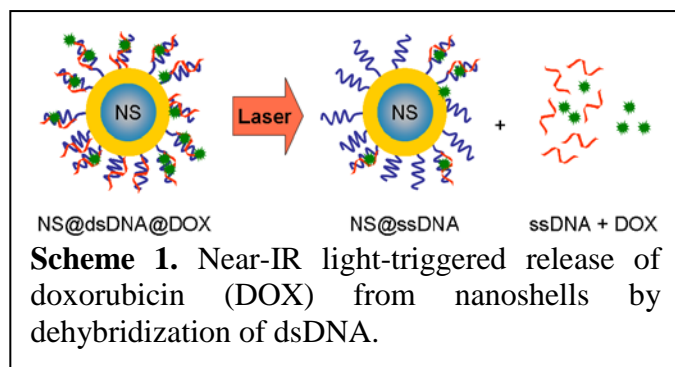
Task 1

a. *Current objectives*

The original proposal suggested the immobilization and near-IR triggered delivery of lapatinib from gold nanoshells. The goal was to load lapatinib onto the nanoshell surface by intercalating the drug within of dsDNA sequences bound to the nanoshell surface. The dsDNA sequences would have one strand that was thiolated and covalently linked to the particle surface, while the complementary strand was not. Upon irradiation, the complementary sequence would be released from the particle surface thereby releasing lapatinib locally. We proposed to load these nanocomplexes into macrophage/monocyte cells that could then be used to deliver them into the brain metastases.

In the first year's report, we detailed the difficulties we encountered with lapatinib solubility and light-triggered release. As a potential solution, we decided to focus on the delivery of doxorubicin (DOX). DOX is a chemotherapeutic agent, used in the conventional treatment of cancers including: Hodgkin's lymphoma, myeloma,

lung, ovarian, gastric, thyroid, breast, sarcoma, and pediatric cancers. Its mechanism of action is to intercalate between the double strands of DNA. Our modified approach is to intercalate DOX into a GC rich double-stranded DNA (dsDNA) sequence and under laser illumination at the plasmon resonance of the NS@DNA@DOX complex, dehybridize the dsDNA and release DOX (Scheme 1).

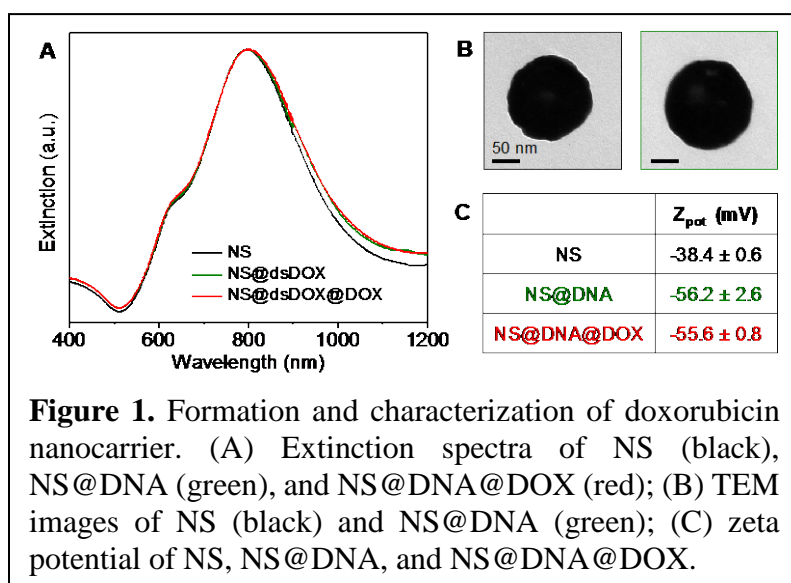


b. Results

In order to deliver DOX, we synthesized a nanocarrier from which DOX could be released by DNA dehybridization. The dsDNA sequences used in this study were engineered specifically to bind to the chemotherapeutic DOX: 5'-HS-(CH₂)₆-CAA TCA ATA GCT ATC GTT CG-3' and 3'-GTT AGT TAT CGA TAG CAA GC-5'. Prior to attachment to the nanoshell (NS) surface the DNA was hybridized by mixing equal moles of the two DNA strands with 33 mM NaCl, heating the mixture to 100 °C for 4 min and slowly cooling to room temperature overnight. Nanoshells were functionalized with double-stranded DNA (dsDNA) via a Au-S bond. The dsDNA-NS mixture was incubated overnight with continuous shaking. The solution was washed several times to remove the dsDNA excess. The NS@dsDNA complex was incubated with DOX for 24 h and excess DOX was removed via centrifugation.

Vis-NIR spectroscopy, transmission electron microscopy (TEM), zeta potential, and dynamic light scattering (DLS) measurements were utilized to provide evidence of the formation of the DOX nanocarrier. The extinction maximum of bare NS slightly red-shifted after dsDNA functionalization, due to the change in the dielectric environment around the NS (Fig. 1A). No changes in the peak shape or width of the extinction spectra was observed, indicating that the NS@dsDNA nanocomplexes do not aggregate during the functionalization process. TEM images

illustrate the thin layer of DNA formed on the nanoshell surface (Fig. 1B). Zeta potential measurements further confirm modification of the NS surface (Figure 1C). The zeta potential of the particles decreased ~18 mV after



DNA functionalization as a result of the negative charges on the DNA phosphate backbone. The zeta potential increased slightly after incubation with DOX due to screening of the DNA charges.

Cellular uptake of the NS@DNA complex was investigated using confocal and reflectance (emission and excitation at 640 nm) microscopy. For the initial experiments, RAW 264.7 a mouse macrophage cell line from an Abelson murine leukemia virus-induced tumor was utilized. This cell line has the advantage of being immortalized and is easy to propagate in cell culture in comparison to the monocytes isolated from human blood and utilized previously [1, 2]. Briefly, the RAW 264.7 macrophage cells were cultured for 24 h in an 8- well micro-chamber slide and then incubated with the NS@dsDNA. After 20 h, the cells were rinsed three times with PBS and fixed in a 4% paraformaldehyde solution. The cells were washed twice with PBS and incubated with a Hoechst 33342 solution to stain the cell nucleus. After 10 min of incubation and protected from light, the cells were rinsed twice with PBS. All images were collected on a Nikon A1-Rsi Confocal microscope and the particles were imaged in the reflection mode. The 3D maximum intensity projection image, corresponding to a slice from the middle of the cell, confirms internalization of the NS@DNA nanoparticles (red dots, Fig. 2). The details in the orthogonal YZ and XZ planes illustrate the location of the nanoparticles within the cell boundary, around but not inside the nucleus.

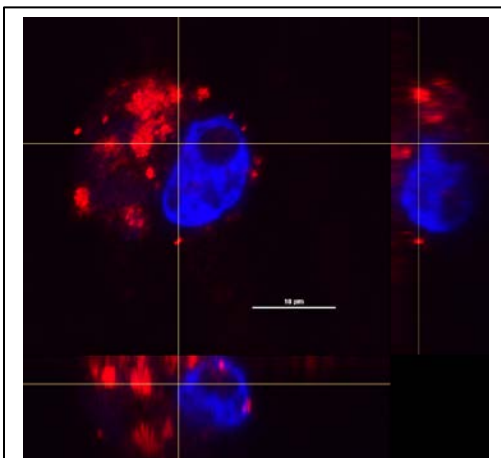


Figure 2. Confocal image of cellular uptake of the nanoshell-DNA nanocomplex in a RAW 264.7 macrophage cell. Orthogonal view of the 3D maximum intensity projection image of cells incubated overnight with nanocarrier. Nucleus is stained blue with Hoechst 33342. Nanoparticles were located by reflection (emission and extinction at 640 nm). Scale bar = 10 μ m; 60x oil immersion objective; NA = 1.4.

In response to the previous challenges we encountered with regard to demonstrating light-triggered release of lapatinib, we decided to take a step back and investigate in greater detail the mechanism of light-triggered release in order to better control and tailor the release for various molecular cargos. In this study, we used NS functionalized with dsDNA; one strand was thiolated and the complementary strand tagged with fluorescein [5'HS-(CH₂)₆-TAT GAT CTG TCA CAG CTT GA-3' and 5'- ATA CTA GAC AGT GTC GAA CT-Fluor-3']. The dsDNA dehybridization process was investigated by fluorescence spectroscopy. It had previously been demonstrated that when a high concentration of nanoparticles was present, release of cargo using a continuous wave (CW) laser could be achieved at temperatures below the DNA dehybridization temperature [3]. Based on this observation, a non-thermal release mechanism by hot-electrons was proposed. In this study, we reduced the particle concentration to better simulate the concentration of particles that is realistically achievable within a tumor. We found by heating the nanoparticle solution with a temperature-controlled stage that thermally induced dehybridization of our specific dsDNA sequence occurred at 61.1 ± 2.3 °C (Fig. 3A). Dehybridization of the same

sequence using CW light occurred at 59.4 ± 5.1 °C (Figure 3B). In these experiments, we observed that release does not occur until the laser power is high enough to increase the bulk temperature above the dehybridization temperature. This is evidence that the dsDNA dehybridization occurs as a result of the heating from the nanoparticles as opposed to hot-electrons, which would be linearly dependent on the laser power. The high nanoparticle concentrations used in earlier experiments resulted in optical light trapping due to multiple scattering of the nanoparticles, allowing the local temperature to increase and dehybridize the DNA before a significant rise in the global/bulk temperature was measured. Unfortunately, that nanoparticle concentration is not achievable in a tumor. Alternatively, a femtosecond pulsed wave laser enables significant temperature increases on the nanoparticle surface without heating the solution (Figure 3C). By irradiating our nanoparticle solution with an ultrafast laser, we were able to demonstrate release at 43.9 ± 1.1 °C, ~ 16 °C below the dehybridization temperature.

We followed up these observations by embarking on an in depth investigation of the specific mechanisms of DNA release from gold-silica nanoshell complexes using the two lasers: continuous wave (CW) and femtosecond pulsed. As detailed in our recently published paper entitled: “Understanding Resonant Light-Triggered DNA Release from Plasmonic Nanoparticles” (Appendix)[4], CW laser illumination enables photothermal by dehybridizing the doubled-stranded DNA and, thereby, releasing single-stranded DNA, while pulsed-laser excitation results in double stranded DNA release by cleavage of the Au–S bond at the nanoshell surface, with negligible local heating.[4]

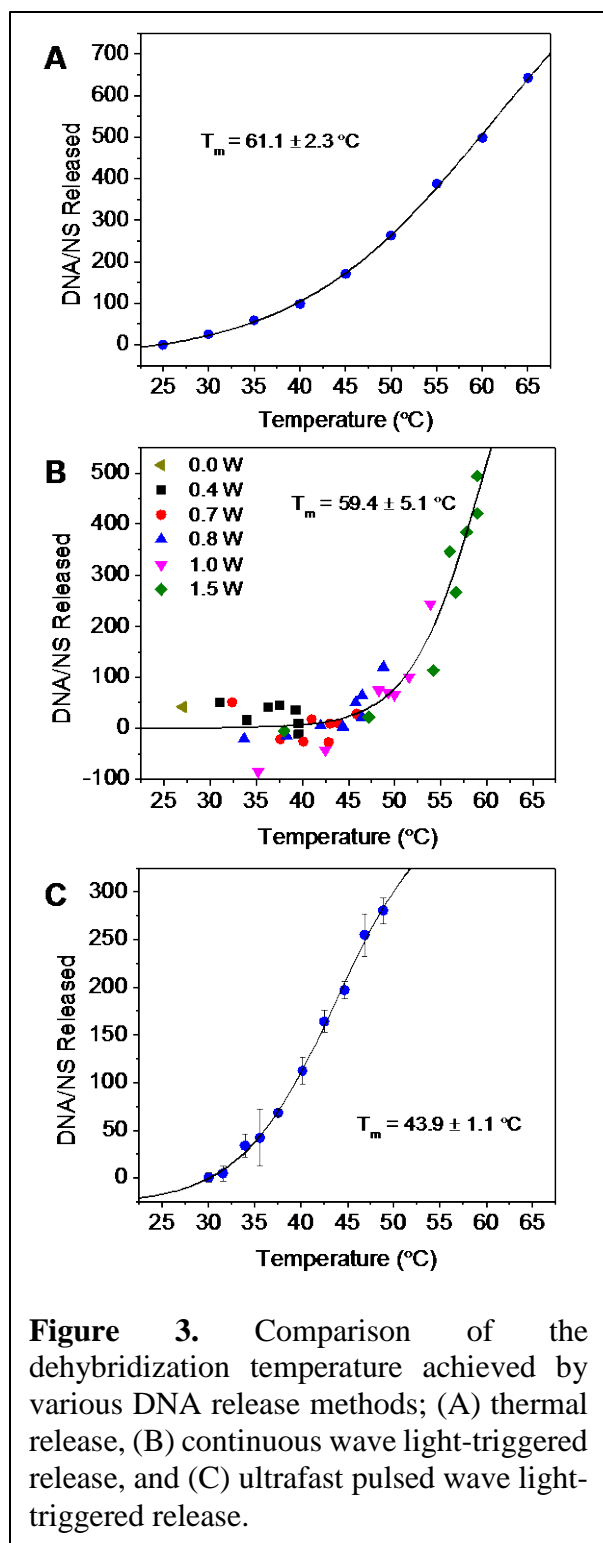


Figure 3. Comparison of the dehybridization temperature achieved by various DNA release methods; (A) thermal release, (B) continuous wave light-triggered release, and (C) ultrafast pulsed wave light-triggered release.

Subsequently, we examined the intracellular release of DOX by both CW and pulsed lasers. Also, armed with our better understanding of DNA release as a function of the laser, we revisited lapatinib release and cytotoxicity. DOX and HER2-targeted lapatinib, were delivered to MDA-MB-231 and SKBR3 (over expresses HER2) breast cancer cells and compared to release in non-cancerous RAW 264.7 macrophage cells. Continuous wave laser-

induced release of DOX from a DNA scaffold showed increased cell death, but also resulted in non-specific cell death from the laser itself (Figure 4A). For lapatinib release, the pulsed laser treatment using a human serum albumin protein scaffold to envelope the drug showed increased cell death in cancerous cells, while non-cancerous macrophages were unaffected. These results show that a pulsed laser can induce drug release in vitro using low levels of near-IR light without causing non-specific cell death, unlike continuous wave light-triggered release. Using the hydrophobic pocket of a protein scaffold to load and release hydrophobic drug molecules is a favorable strategy for controlled drug delivery that can be extended to myriad of cancers and chemotherapy drugs. We have now come full circle and have devised a method in which to deliver lapatinib using gold-silica nanoshells.

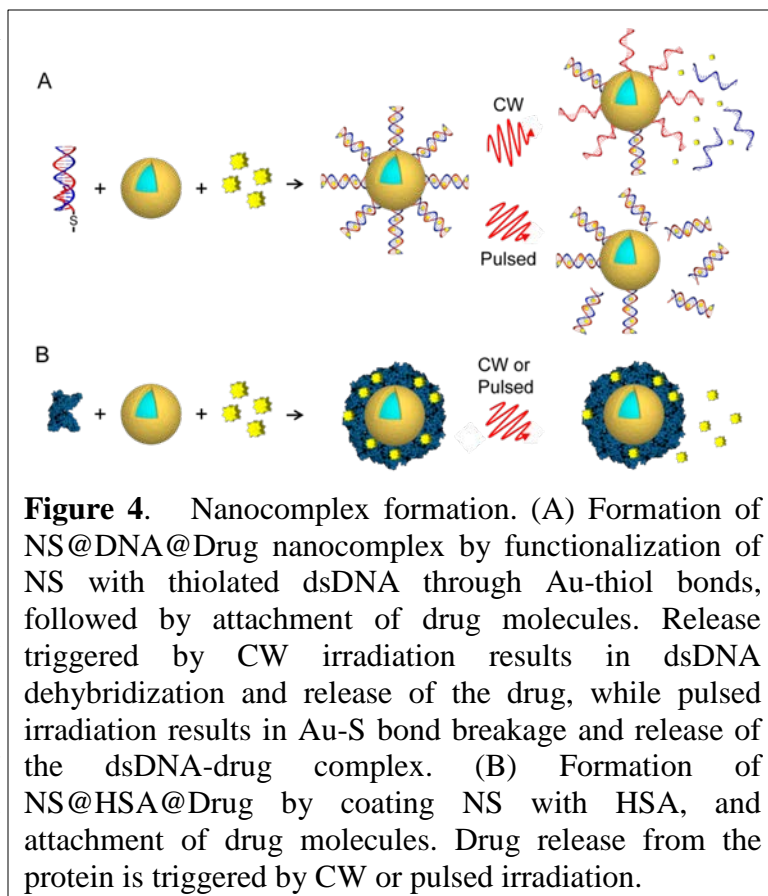


Figure 4. Nanocomplex formation. (A) Formation of NS@DNA@Drug nanocomplex by functionalization of NS with thiolated dsDNA through Au-thiol bonds, followed by attachment of drug molecules. Release triggered by CW irradiation results in dsDNA dehybridization and release of the drug, while pulsed irradiation results in Au-S bond breakage and release of the dsDNA-drug complex. (B) Formation of NS@HSA@Drug by coating NS with HSA, and attachment of drug molecules. Drug release from the protein is triggered by CW or pulsed irradiation.

Task 2

a. *Current objective*

To optically release the drug attached to the surface of the gold nanoparticle, it is necessary to deliver and validate the *instantaneous* fluence (the radiant energy per unit surface area) at the location of the tumor. Given that, there is little data on the amount and distribution of near infrared light through the skull and brain tissue. To provide an estimate of the energy transport of near infrared light through the skull and within brain tissue, a number of diagnostic tools were developed. First, a nearly isotropic optical dosimetry probe was fabricated to obtain local photon fluence measurements with 1.5 mm spatial resolution and high sensitivity. Calibration of the probe was performed in air and water-based phantoms using a calorimeter (considered a Gold Standard). Second, a voxel-based Monte Carlo simulation code written in CUDA for GTX Nvidia (Dr. Fang, Harvard) was further developed for different optical beam properties, such as super Gaussian beams with parallel, converging, and diverging beam profiles, and with the ability to run on multiple Nvidia cards (n=3). Third, an empirical method to simulate photon transport was developed to provide sufficiently accurate solution at accelerated rates. Monte Carlo simulations for photon transport are computational intensive and therefore are typically not practical for clinical use. These

codes provide solutions in real-time during the developmental stage of the treatment plan. These tools were used to:

2a. Estimate of the attenuation of near infrared irradiation by the skull using the fluence probe; and

2b. Estimate of the attenuation of near infrared irradiation by the skull and brain tissue phantom using the fluence probe.

b. Results

i. Calibration of the Optical Dosimetry Probe (ODP) [5, 6]: The objective was to fabricate and calibrate the optical dosimetry probe (ODP) to a calorimeter (Nova II; Ophir). The ODP consists of a 1.5 mm diameter sphere (epoxy and titanium dioxide) molded onto the end of a 200 μ m optical fiber. The output of the fiber was coupled to a photodiode (ET-2030, Electro Optics Technology Inc), the output of which was recorded by a digital oscilloscope (Tektronix TDS3052B). The digitized signal was uploaded to a PC, where the signal was passed through a high-pass butterworth filter to reduce background noise and the area underneath the pulse calculated to determine the photon fluence. To calibrate the ODP, the photon fluence in air was measured by both the ODP and calorimeter using a uniform laser beam formed by passing the output of the laser/OPO system (Nd:YAG class 4 laser/ MagicPRISM OPO, Opotek Inc.) (tuned to 800nm) through an integrating sphere (Melles Griot). The results are displayed in Figure 1. To determine the fluence in water (or tissue), the change in the index of refraction causes the reflective properties between the probe media and water to change, thus requiring an additional correction factor. The probe was placed within a macrocuvette, a plexiglass container which was approximately 5.0 x 5.0 x 5.0 cm³ (5mm thick walls). The ODP signal and calorimeter measurements were acquired in air as before. The macrocuvette was then filled with water, and the ODP was positioned along the central axis of the uniform beam. From this data, a conversion factor was applied to the ODP signal to convert the calibration curves in air (Figure 1) to tissue. This conversion factor also took into account the variation in the beam width when traversing from plexiglass-to-air versus plexiglass-to-water and photon attenuation for optical path lengths within water, both of which were relative small (~3%, the average error in the laser output power).

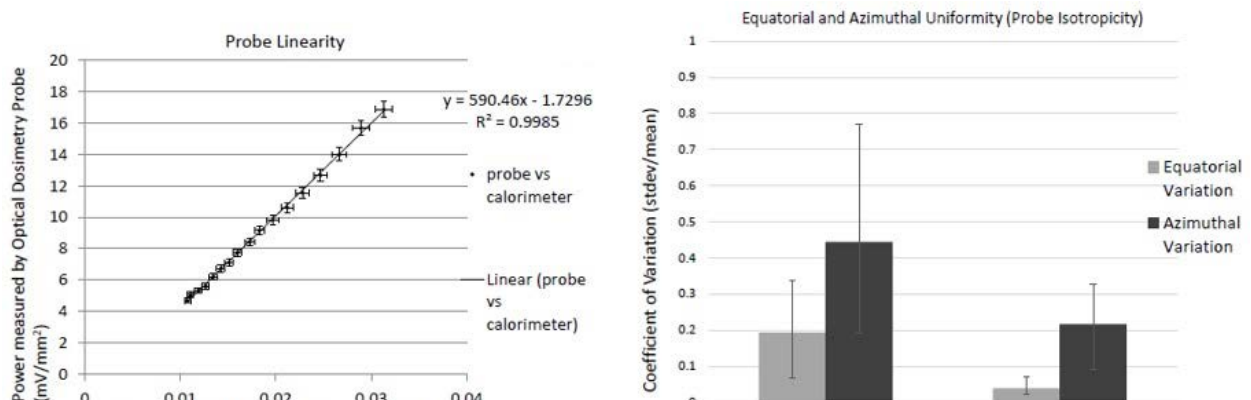


Figure 1: (Left) The output of the ODP in mVolts plotted as a function of laser fluence measured by a calorimeter. **(Right)** The angular dependency (azimuthal and rotation) of the ODP to the direction of laser light was calculated as a function of the absolute value of the residuals and how it compares to nylon probes.

ii. Phantoms Reproducing the Optical Properties of the Head: The objective was to develop a formula that could be used to create water-based (and agar-based) phantoms with the desired optical properties (μ_a and μ_s') for the skull, white matter and gray matter (at 800nm, the wavelength of stimulated drug release). India ink was used as the absorber (with some but little scattering), while intralipid was used as a scatterer (with some but little absorption). To determine the absorption coefficient, various concentrations of india ink in water were placed within the photospectrometer, from which a calibration curve plotted: $15.07 \times \% (\text{india ink}) + 0.0049$ ($r^2=0.99$) (data not shown). The reduced scattering coefficient was determined by placing different concentrations (from 1 to 7%) of intralipid in water, exposing the solution to a uniform (1cm diameter) laser beam using an integrating sphere as described in the previous section. The photon fluence was measured using the ODP at various path lengths (or depths) along the central axis of the beam. To determine the reduced scattering coefficient in each sample, Monte Carlo simulations were performed for various reduced scattering coefficients until a minimum in the chisquare was

Table I: Optical properties of the skull bone, white matter, and gray matter.

	μ_a	μ_s	g	μ_s'	intralipid	ink
	[cm^{-1}]	[cm^{-1}]		[cm^{-1}]	[%]	[%]
white	0.05	550	0.85	82.5	7.5	0
gray	0.35	700	0.965	24.5	2.36	0.023
skull	0.24	184	0.9	18.4	1.82	0.0156

reached. The data was plotted and fit to a line: $11.30 \times (\% \text{intralipid}) - 2.17$ ($r^2=0.99$) (data not shown). From these measurements, the white and gray matter phantoms were fabricated based the optical properties measured by Van der Zee *et al* [7], and the skull phantom optical properties were based on measurements by Firbank *et al* [8], see Table I.

iii. Simulating Photon Transport in Phantoms/Tissue [5, 6, 9]: The objective was to develop and validate a voxel-based Monte Carlo code of photon transport in the head and brain. A voxel-based 3-D Monte Carlo (MC) code (Fang *et al* [10]) developed in CUDA for NVidia cards was modified to allow the user to create laser sources with various aperture profiles, such as uniform and super-Gaussian, and directionality, such as diffusive, converging, and diverging beams. Supporting code (Matlab) was developed to allow the user to design their own objects, which in this study was based on phantom designs and medical images (CT).

A critical advantage of a voxel-based code is not only to include tissue heterogeneities but to integrate medically acquired images into the simulations. To date, the MC code has not been validated with measured data; therefore, a number of experiments were performed. First, the photon fluence distribution was measured using the ODP in phantoms representing white matter, gray matter, and skull bone. The ODP probe was secured to a 3-D stage micrometer to obtain measurements along the central axis of the beam at various depths in the phantom (axial

profile) and perpendicular to the central axis (lateral profile). These measurements were taken using a uniform and a super Gaussian laser beam. Next, Monte Carlo simulations were performed and compared to measurement.

In

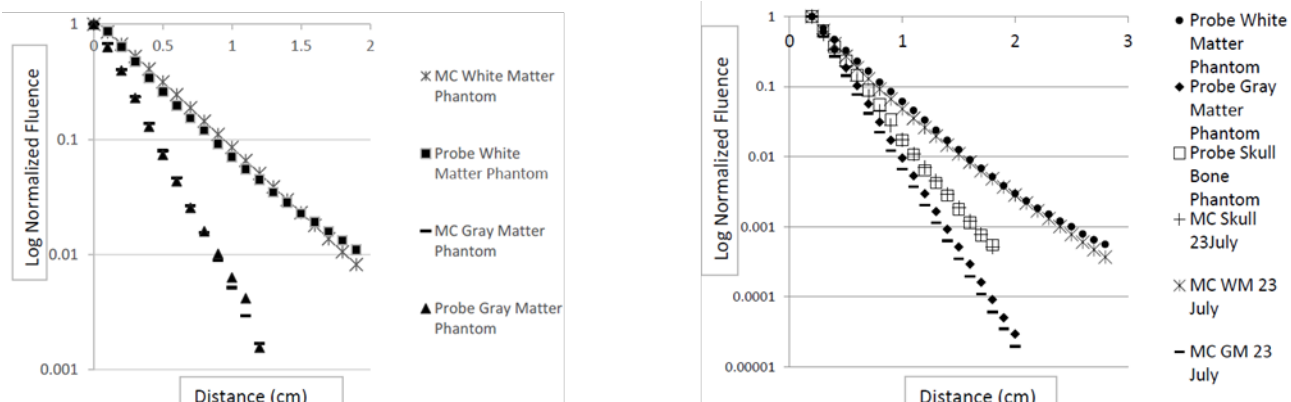


Figure 2. The fraction of the input fluence as measured by the ODP at different depths in white and gray matter phantoms for a uniform laser beam (1.0cm in diameter) (left) and a super Gaussian beam profile (right). Included in these plots are the Monte Carlo simulated results, which agree to within 3.0% of the measured values.

Figure 2, the normalized fluence along the central axis of the flat beam was plotted for both white and gray and for ODP and MC data. For depths up to 2 cm, the agreement is within 3%. Similar experiments were performed for the super Gaussian beam, where for depths up to 3 cm, the MC simulated results matched the ODP measurements. The comparison of the lateral profiles for the super Gaussian beam is shown in Figure 3, and demonstrates the excellent agreement between ODP and MC results.

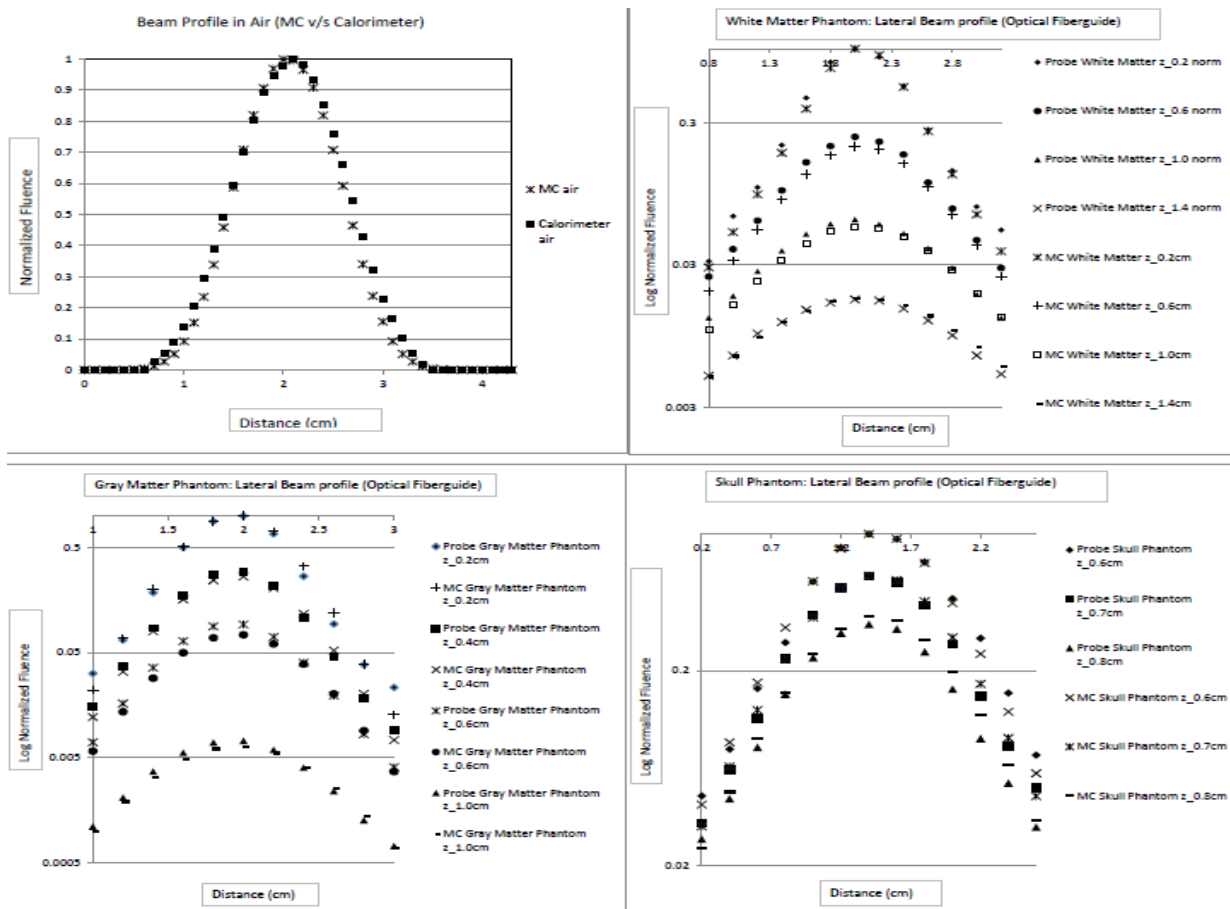


Figure 3. Plotted are the relative photon fluence as measured by the ODP and as simulated by the MC code for a super Gaussian laser beam in air (top left), white matter (top-right), gray matter (bottom-left), and skull (bottom-right).

iv. Sheep Skull and Brain Phantom: In combination with the phantom study from the previous section, an estimate of the attenuation of near infrared irradiation by the skull and brain tissue phantom was made. The laser beam emanating from the optical fiber bundle was measured in air using the ODP and used to determine the beam profile, e.g., super Gaussian function, and laser fluence. This laser beam was positioned as close to normal to the sheep skull as possible. The thickness of the bone where the laser beam was exposed was measured to be 1.1cm using calipers and validated by CT scans. To measure the laser beam profile at the inner surface of the skull, the dosimetry probe was axially positioned within 4 mm of this inner surface, and using a 3-D micrometer, the ODP was translated perpendicular to the laser beam to measure the fluence profile and along the axis of the beam profile to determine the peak beam intensity as a function of the distance from the inner surface (see Figure 4). After applying the calibration factors (Section: Calibration of ODP), **the percent of the laser fluence transmitted through the skull was measured to 4.41% (SA2.A).** MC simulated data were consistent with these ODP measurements (see Figure 4).

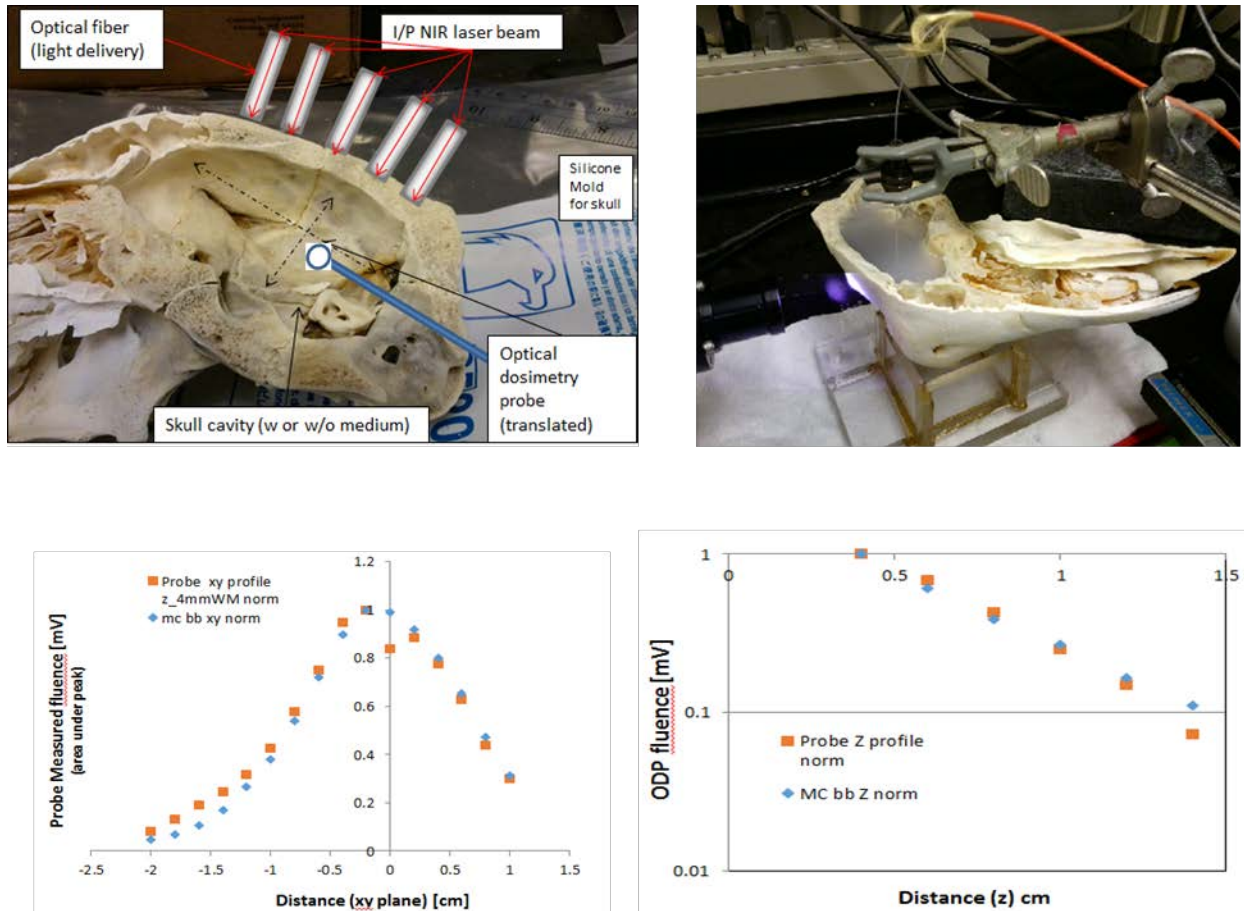


Figure 4. (Top row) Displayed are the photos of the sheep skull and the ODP used in the phantom experiments. The picture on the right has the laser beam exposing the frontal bone (left to right) and the ODP embedded in the brain tissue phantom. **(Bottom row)** Plotted are the lateral profile near the inner surface of the skull and the axial profile along the central axis of the laser beam as measured by the ODP probe and simulated using the MC code.

With this same setup, the skull cavity was filled with a 4% intralipid solution. The ODP was used to measure the attenuation of the beam (Figure 4. Top right, bottom right): the transmitted fluence was measured to be 7.25% per cm, which is consistent with Figure 2. If a 7.5% of intralipid (white matter) was used, the measured

transmitted fluence was 3.1% per cm, and gray matter was measured to be 0.31% per cm (see Figure 2). To relate these measurements to a human patient, average values for the thickness of the cortical gray matter and skull bone is determined. Cortical gray matter thicknesses can range from 2.0 to 5.0 mm, averaging around 4.7-4.85 mm [11, 12]. Skull bone thickness can range from 5.0 to 11.0 mm in an adult human head, averaging around 7.8 mm. **Based on the above measurements, the average fluence transmitted through 8.0 mm of the skull bone would be 10.3% and through 4.8mm of gray matter would be 9.1%, or 0.93% on average through both tissues. Therefore, a tumor 4.5cm deep within the brain would receive approximately 8.5×10^{-9} of the laser fluence (SA2.B).** Depending on the location of the tumor, the positioning of the optical sources could take into account the heterogeneity of the skull and gray matter. Optimally, a region of the skull and gray matter that that is 5mm (24.3% transmitted) and 2.5mm (20.0% transmitted) thick would increase the fluence to 1.9×10^{-8} , an improvement of a factor of 4.4. This suggests that a multiple number of sources optimally positioned for treatment based on the patient's anatomy may be beneficial.

v. Empirical Model of Photon Transport [6, 9]: An empirical method was developed to simulate photon transport in tissue based on the acquired medical images of an individual patient (CT and MRI) with sufficient accuracy and at accelerated rates for clinical use. This approach is based on the assumption that the photon fluence in a voxel within a particular layer (or slice of an image) is the weighted sum of the fluence from its neighboring voxels in the previous layer. These weights determine the fraction of photons within a photon packet that is transported from one voxel to its neighbors relative to its average (or weighted) direction of propagation. It depends not only on a voxel-based geometry of the image but the voxel size and optical properties of the medium. It has been shown to faithfully reproduce the local shadowing effects from high absorbers (e.g., blood vessels) and high contrast media (gold nanoparticles), and general attenuation in homogeneous tissue types. To determine the weights, MC simulations were performed in known media, such as white matter, gray matter, skull bone, and an Astrocytoma (tumor). Using these fluence profiles, the weights were modified until the photon fluence distribution from the empirical model matched (minimum in Chisquare) MC simulated results for different voxel sizes. A comparison between the photon fluence within each individual tissue type and for a

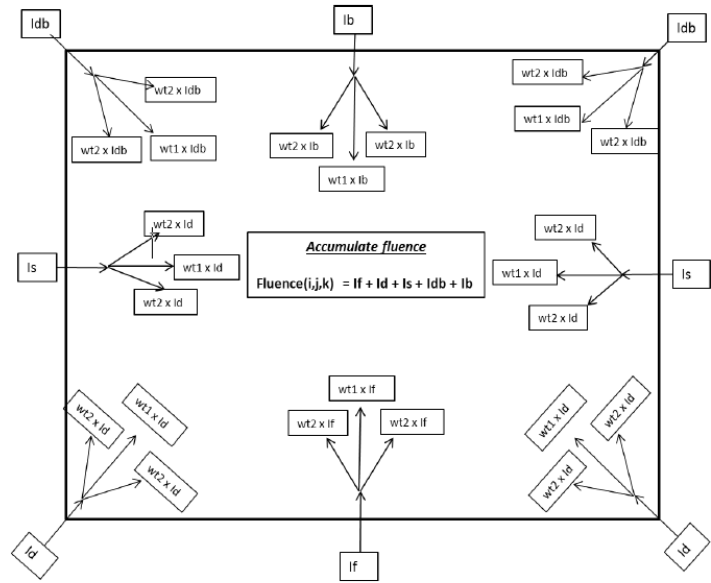


Figure 5. Displayed is a diagram depicting the local photon transport of the empirical model for a voxel within tissue. Note, this takes into account the general direction of the photon packet and the scattering properties of the tissue.

software phantom of the skull and brain are shown in Figure 6. There remains a relative small systematic effect (over estimate) of the photon fluence which requires further investigation, but the agreement is very good to develop and optimize delivery systems based on an individual patient's anatomy. When implemented on CUDA, the time it takes to simulate a human head with a broad beam source (e.g., super Gaussian beam) was on the order of seconds to low minutes where the MC would run in excess of 24 hours.

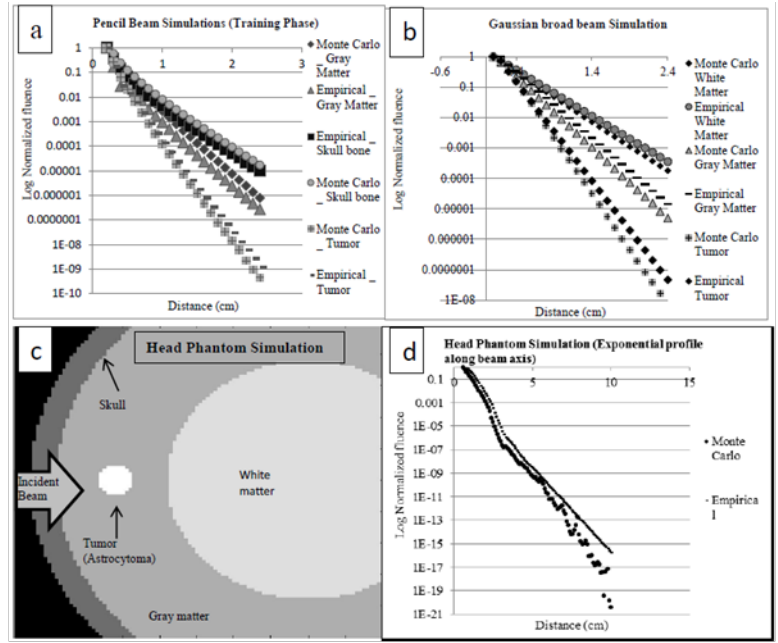


Figure 6. Comparison of the Empirical algorithm with MC simulations in homogenous (a,b) and heterogeneous (c,d) phantoms that resemble white matter, gray matter and astrocytoma. The plots in panels (a), (b), and (d) display the exponential decrease in fluence along the central axis of a Gaussian beam.

vi. NIR transmission in the human skull as a function of the thickness and density of bone

(1) Introduction

The skull forms an optical attenuator (absorber and scatterer) in the transmission of near-Infra-red light to the brain. The success of any NIR based imaging or therapeutic technique depends on an accurate and precise determination of the optical transmission properties of the skull. The skull bone consists of osteocytes and calcium deposits in complex geometries that result in large density variations (or heterogeneities) at different anatomical locations within the skull. Previous studies have looked at the optical transmission properties of different tissues [13-19] using collimated laser beams with powers ranging from 10mW/cm² to 25mW/cm²[13, 14]. These studies included NIR transmission through human cadaver skulls.[14] In our study, we used an NIR laser source (17.64mW/cm²) with a complex super-Gaussian broad beam profile. Our objective is to investigate if the relationship between voxel-based HU and the optical attenuation in the skull bone exists, allowing NIR-based treatment planning of drug release based on CT scans. Simulated Monte Carlo data was compared to measured beam intensity and distribution implementing the TiO₂-based optical dosimetry probe. This data was used to investigate the relationship between the HU from CT images and the optical attenuation by measuring the transmitted NIR light through human cadaver skulls. Critical to these measurements is the ability to quantify low power fluence transmitted through the skull afforded with the TiO₂ optical dosimetry probe compared to the calorimeter used in previous bone transmission studies [15, 16].

To date, studies [8, 20-22] have measured the optical properties of the brain tissues, mapped their heterogeneity and determined their inter-sample variations. In these studies, a comparison of the optical properties of skull bone [8, 20-22] is shown in Table II. It shows a wide variation in the optical properties reported for the human skull bone. A comprehensive work by Bashkatov *et al* [20] mapped these variations in optical properties of the skull bone at different wavelengths. Note, these studies assume an average overall measure of the skull's attenuation. Our aim is to further understand this complexity caused by variations, or heterogeneity, in the bone density and bone thickness to map out an accurate fluence map of the Monte Carlo in the brain. The use of Computed Tomography images provides a 3D map of the heterogeneous bone structure and allows us to accurately generate the boundary conditions and density maps using the Monte Carlo.

Table II Optical properties of skull bone measured at 800nm wavelength in different studies.[8, 20-22] The anisotropy factor (g) is 0.9.

Study By:	Absorption Coefficient (μ_a) (cm^{-1})	Scattering Coefficient (μ_s) (cm^{-1})
Firbank <i>et al</i>	0.24	18.4
Bashkatov <i>et al</i>	0.11	19.48
Pifferi <i>et al</i>	0.07	12.5
Ugryumova <i>et al</i>	0.25	21

(2) Materials and Methods

(a) Optical Bone Dosimetry Setup

10 Different skull bone samples were used for the optical transmission study. The light source consisted of the optical fiberguide connected to a laser source. The NIR output of the fiberguide was measured using a calorimeter to be 19.94mW or (17.64 mW/cm²) at 800nm wavelength. For transmission studies, the optical fiberguide was placed against the outer surface of the skull bone, such that its aperture was flat against the bone surface, thus providing a normal exposure. The fluence transmitted through the bone was measured using the TiO₂ dosimetry probe by placing it against the inner surface of the skull bone, opposite the fiberguide on the other side of the skull, which was ensured by locating the point of maximum fluence. The energy fluence for 5 points or locations per skull was acquired, and at each location the measurement was repeated three times. A total of 10 cadaver skull bones were measured, which gave a total of 50 measurement data points. The setup for these experiments is shown in figures 7.1 and 7.2.

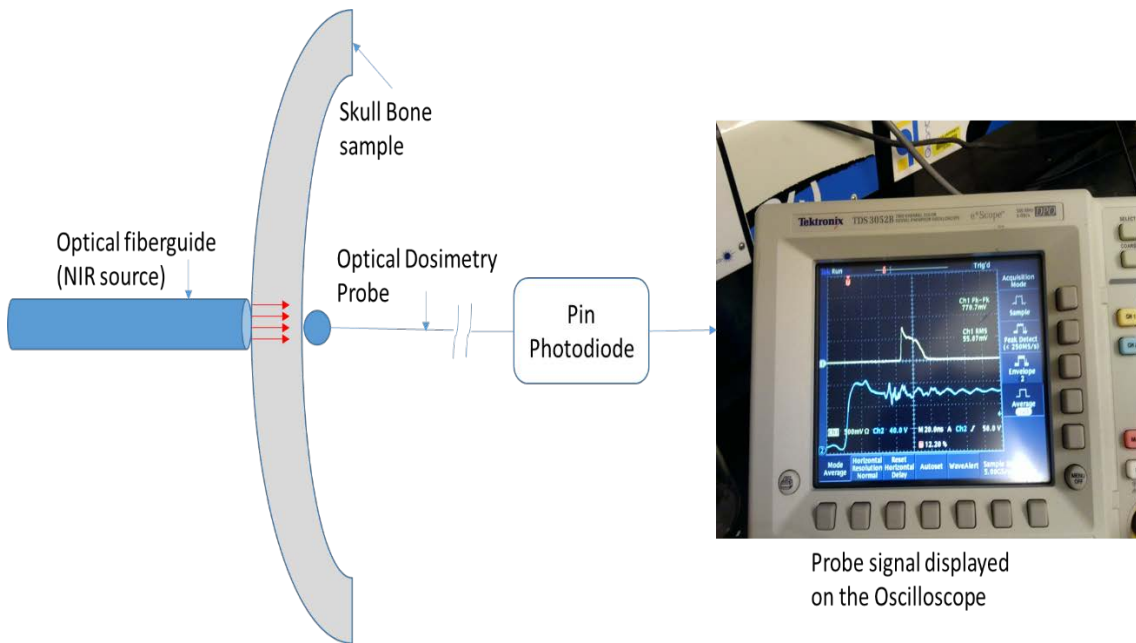


Figure 7.1 Setup to measure the optical transmission of NIR light through the skull bone. The source used is an optical fibreguide connected to a laser. The NIR fluence collected by the probe tip is carried by an optical fiber to a PIN photodiode circuit, whose electrical output is read using an oscilloscope (right).

For the lateral beam profile measurements, each skull was placed in a large Plexiglas cuvette, such that the point of illumination (marked previously on the skull surface) was directly in contact with the cuvette bottom. The transparent optical bench helped in accurately aligning the skull with the source. The experimental setup is shown in figures 7.2 and 7.3. The lateral profile was first measured in air and in water 0.5cm from the inner skull surface. While measurement in air was for further validation of optical transmission, the measurement in water was for a more realistic scenario, where the refractive index of water is similar to that of soft tissue.

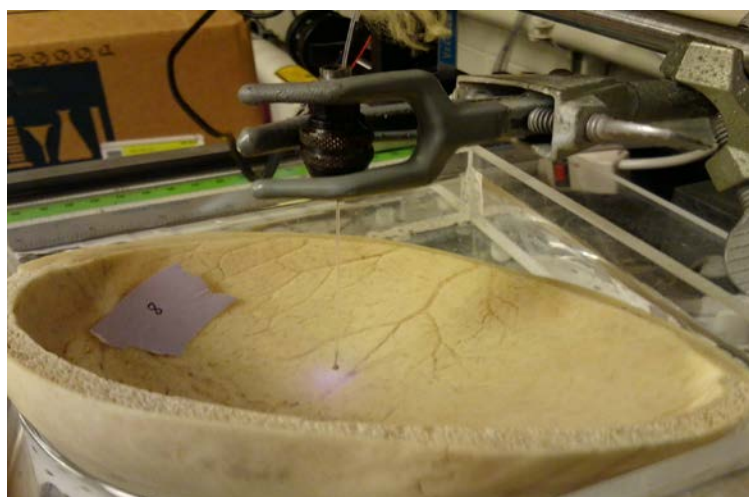


Figure 7.2 Skull bone sample (top portion) used in the experiment. The dosimetry probe is also seen.

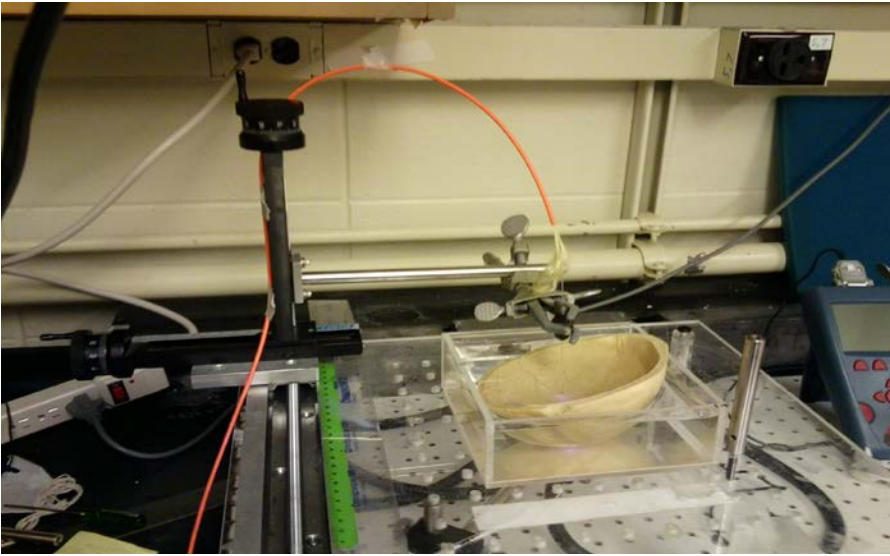


Figure 7.3 Optical dosimetry setup for lateral beam profile measurement in skull sample.

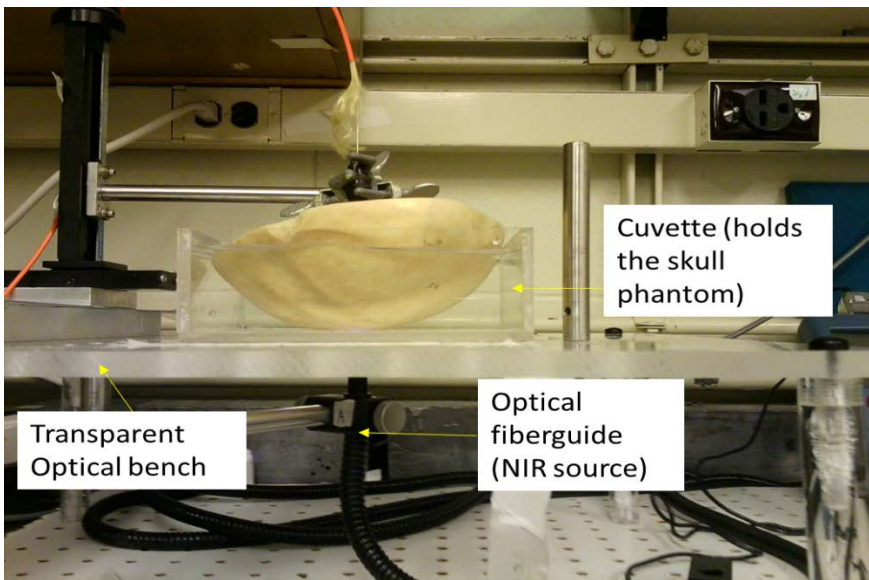


Figure 7.4 Optical dosimetry setup for lateral beam profile measurement in a skull sample. This shows the illumination setup using the optical fiberguide source.

(b) Acquisition and Processing of CT Images of the Skull Bone

Computed Tomography (CT) was used to map optical boundaries and density of the bone on a Philips Brilliance clinical CT scanner. The CT images were acquired at 300 mAs and 120 kVp, and reconstructed with a slice thickness of 0.67mm, a pixel size (xy plane) of 0.2344mm, and using the bone kernel. The points on each skull phantom at which the laser source was applied were labeled using CT contrast beads and marked with a pencil (see Figure 7.5).

Figure 7.5 shows the use of CT contrast beads to mark the point of illumination on the skull samples. The CT images were displayed and processed using Matlab based software, which was custom developed to identify the source and detector positions and simulate the bone boundaries on CT images, as shown in figure 7.5. The point

of measurement for optical transmission lies on the inner skull boundary on the line while lateral profile is measured at 0.5 cm from the inner skull surface.

In order to identify the source voxel for illumination, another line was drawn tangential to the skull surface, passing through the intersection point of the bead and the outer skull surface as shown in figure 7.5 (B). The cross product of the illumination vector and the source tangential vector is the other vector which also lies tangential to the skull surface along the z axis $[0 \ 0 \ 1]$. The source voxels are then identified as those lying on the 3D circle defined by the two tangential vectors. The parametric equation used of a 3D circular disk [23] can be then used to represent the fiberguide source surface as described by the two tangential vectors. Thus one can accurately represent any broad source in the Monte Carlo at any arbitrary angle as used in the experimental setup.

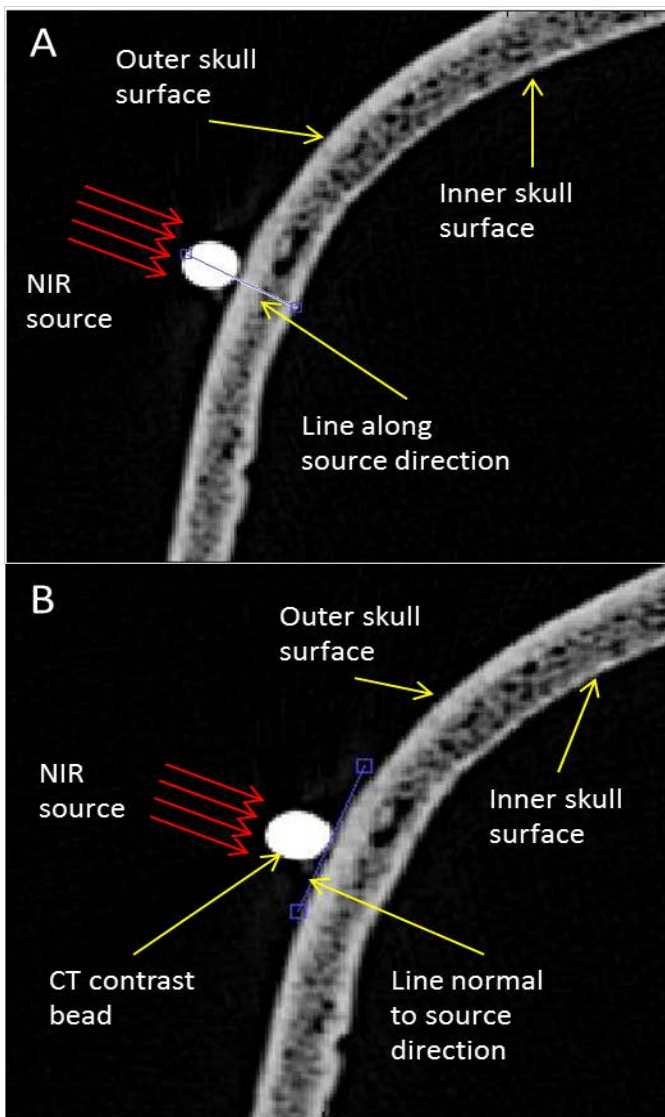


Figure 7.5 The CT image of a skull bone is processed in Matlab to extract the source directional vector (A) and in-plane source vector (B) by drawing lines (blue) on the image and extracting the end points of the lines to calculate the vectors. The third vector is the cross product of these two vectors and is in the plane of the source.

(3) Results

(a) Optical Transmission Measurements in the Skull

The result for the optical transmission for 10 different phantoms is shown in figures 7.6, 7.7 and 7.8. Note that the phantoms are numbered from 1-4 and 6-11 as phantom 5 was not used (incomplete CT scan). The optical transmission measurements show a wide variation in the optical power transmitted, due to variation in skull thickness and (heterogeneity in) bone densities. In order to map the Monte Carlo fluence to the % transmission measurements of the probe, we used CT images to determine the optical path-length through the bone (i.e. skull thickness in the direction of illumination). The skull thicknesses measured using CT images showed different skull thicknesses both within and across the skull samples. The measured skull thicknesses from the CT images are shown in figure 7.9. We also measured the lateral beam profiles in the skull phantoms in air and water as shown in figure 7.10.

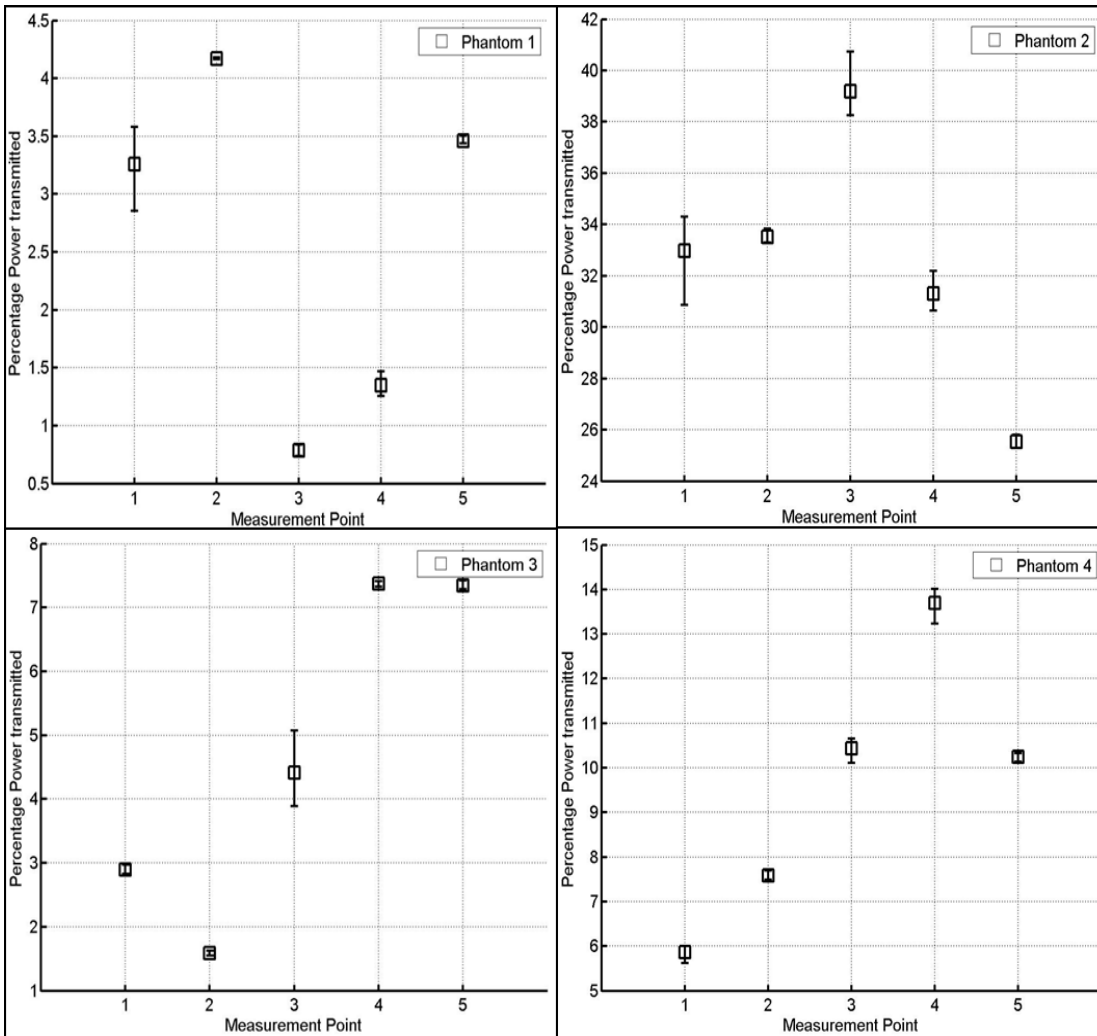


Figure 7.6 Percentage fluence transmitted for phantoms 1-4 measured using the probe calorimeter setup.

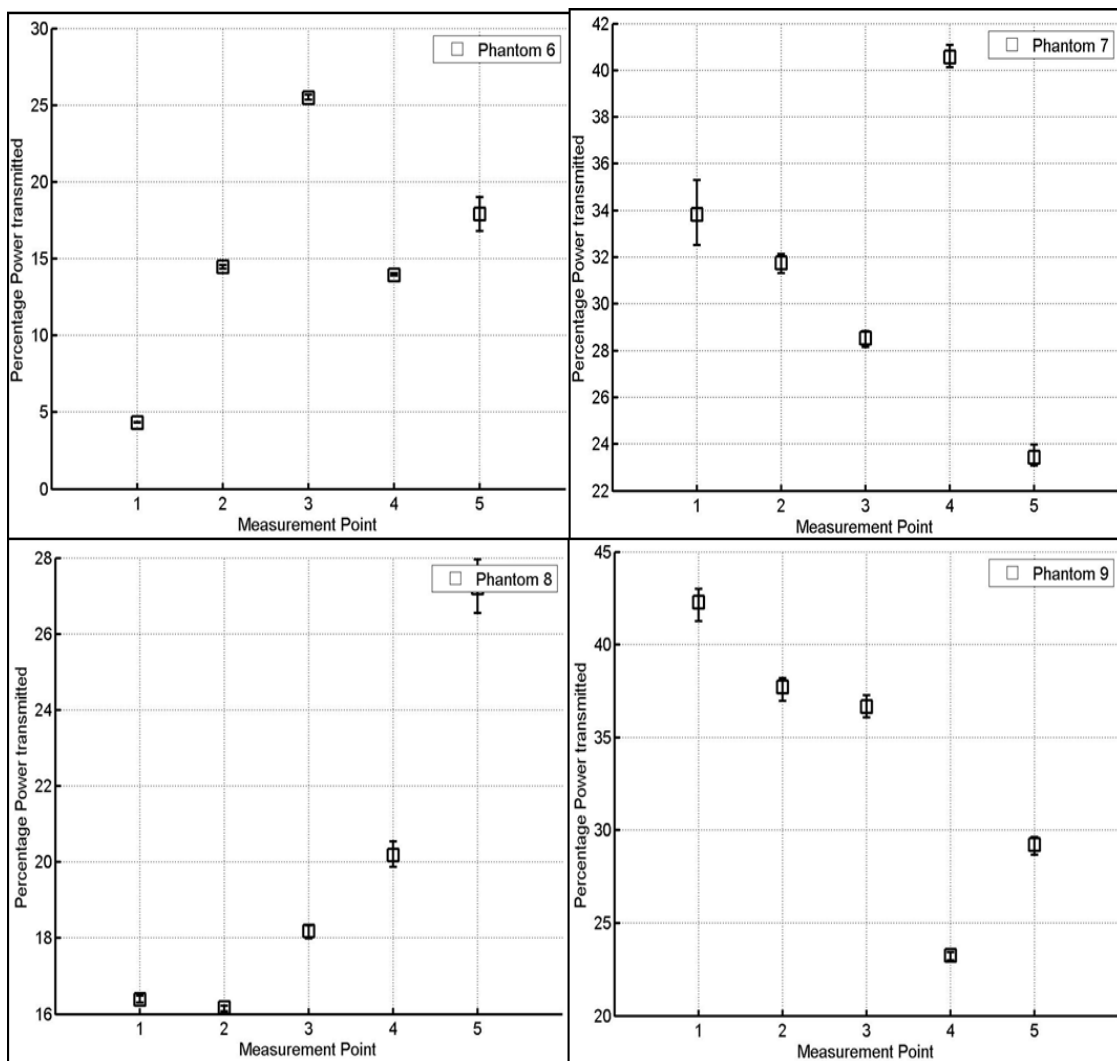


Figure 7.7 Percentage fluence transmitted for phantoms 6-9 measured using the probe calorimeter setup.

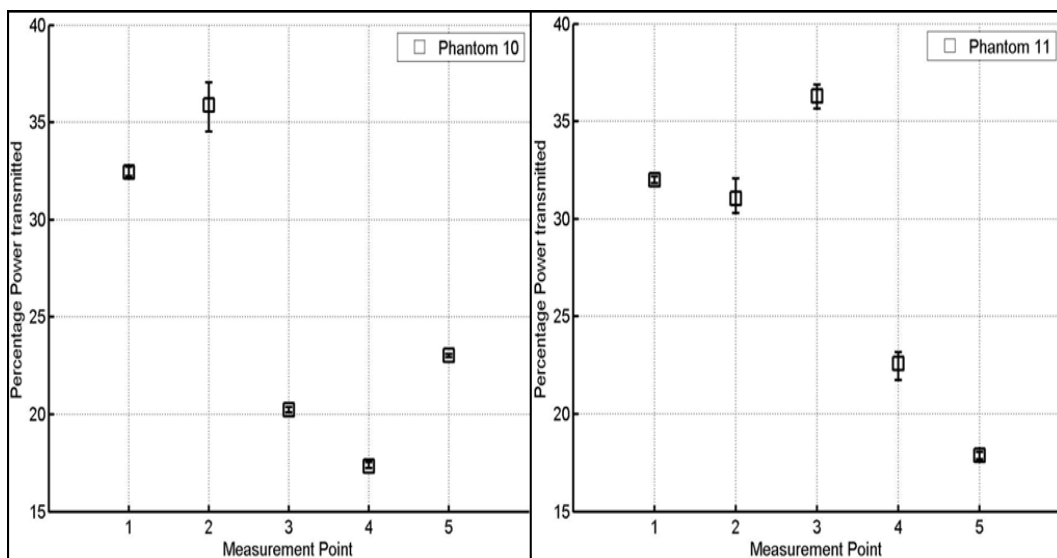


Figure 7.8 Percentage fluence transmitted for phantoms 10-11 measured using the probe calorimeter setup.

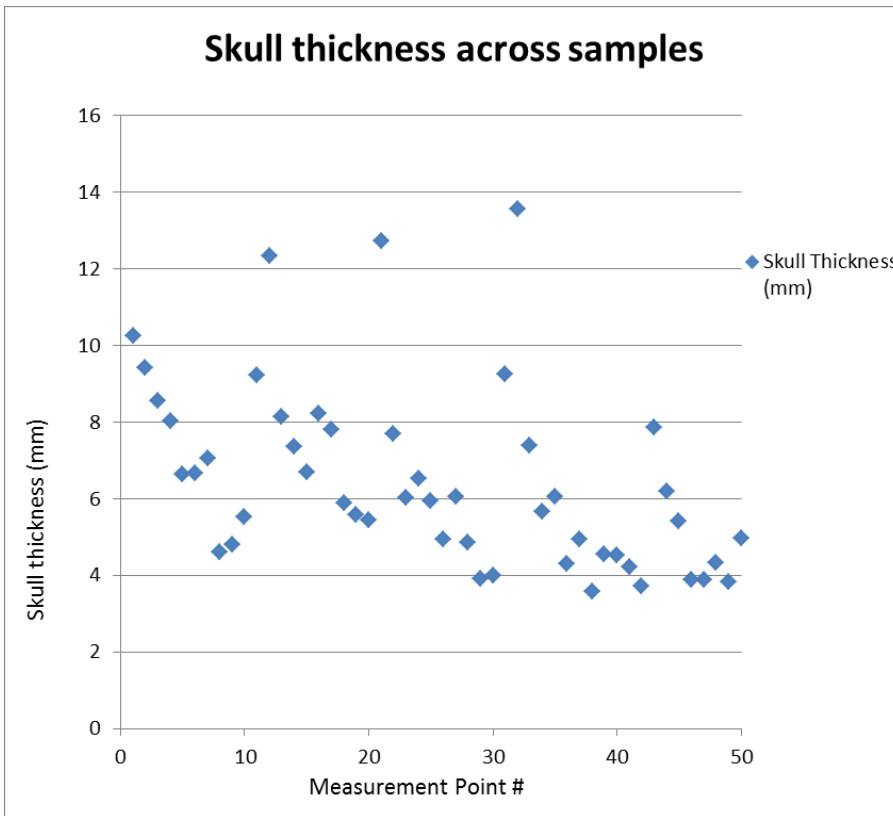


Figure 7.9 Skull thicknesses measured across skull samples using CT image data. Measurement points are categorized as follows: Phantom1 (1-5), Phantom2 (6-10), Phantom3 (11-15), Phantom4 (16-20), Phantom5 (21-25), Phantom6 (26-30), Phantom7 (31-35), Phantom8 (36-40), Phantom9 (41-45), Phantom10 (46-50).

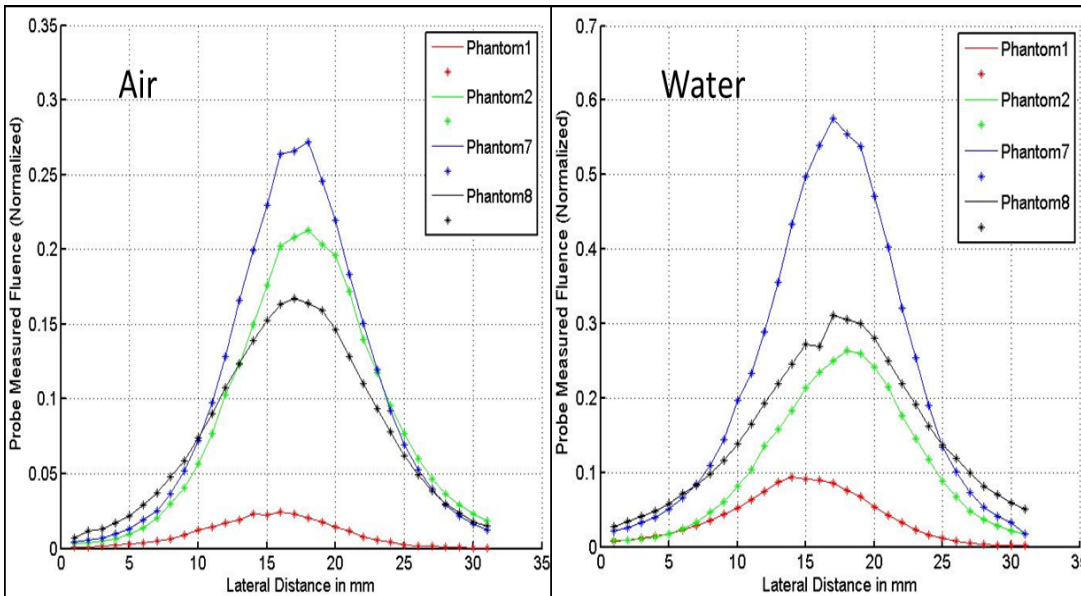


Figure 7.10 Lateral beam profile (fraction transmitted) measured using the dosimetry probe in air and water 0.5mm from the inner skull surface.

(b) Comparison with the Monte Carlo

Based on the three different sets of optical properties of the skull bone shown in Table II, three Monte Carlo profiles were obtained with a super-Gaussian beam distribution. The fluence profiles along and perpendicular (lateral profile) are shown in figures 7.11 and 7.12 respectively. The Monte Carlo simulations show that different

optical properties of the skull bone will give rise to different transmission characteristics, which could result in different transmission factors and lateral beam profiles. The lateral beam profiles due to different optical properties also show the variations between the four models.

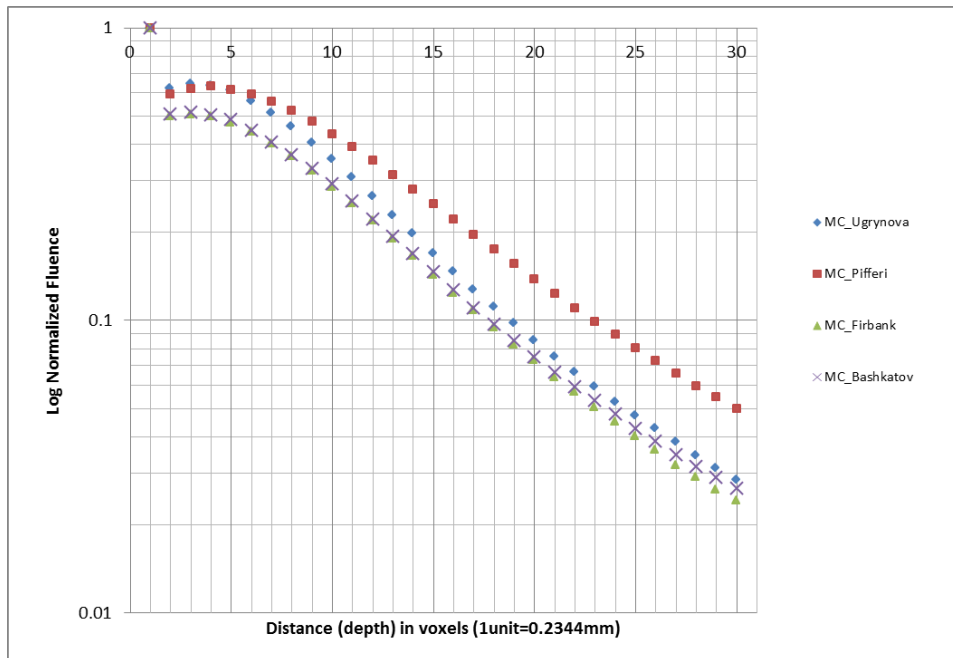


Figure 7.11 MC simulated fluence profiles along beam axis for a homogeneous skull medium generated using Monte Carlo simulations for three sets optical properties of the skull bone (Ugrynova *et al*, Pifferi *et al*, Firbank *et al*, and Bashkatov *et al*). A broad beam super-Gaussian NIR source (800nm wavelength) was simulated.

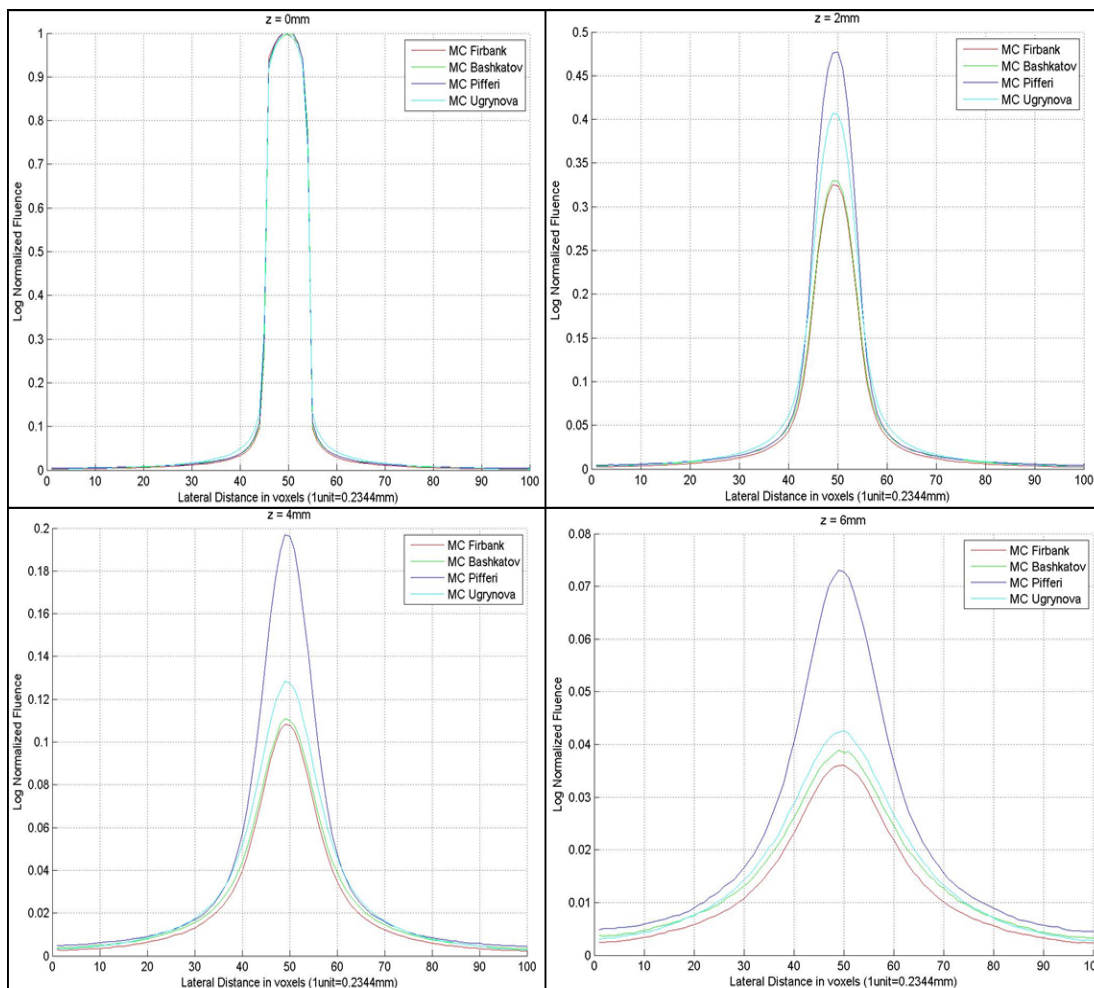


Figure 7.12 MC simulated lateral fluence profiles at different depths ($z=0,2,4,6\text{mm}$) for a homogeneous skull medium generated using Monte Carlo simulations for three sets optical properties of the skull bone (Ugrynova *et al*, Pifferi *et al*, Firbank *et al*, and Bashkatov *et al*). A broad beam super-Gaussian NIR source (800nm wavelength) was simulated.

The % power transmitted using the probe-calorimeter setup was then compared to the % power transmitted using the Monte Carlo simulations. The simulations in the homogeneous skull phantom were used in the form of a lookup table to derive the MC generated fluence using interpolation. The skull thicknesses measured using CT images were used to look up and interpolate the corresponding normalized fluences in the MC table. The percentage power transmitted is the normalized fluence on the beam axis at that specific depth multiplied by 100. Figure 7.13 shows the comparison between the transmitted values measured by the probe and those simulated by the Monte Carlo code.

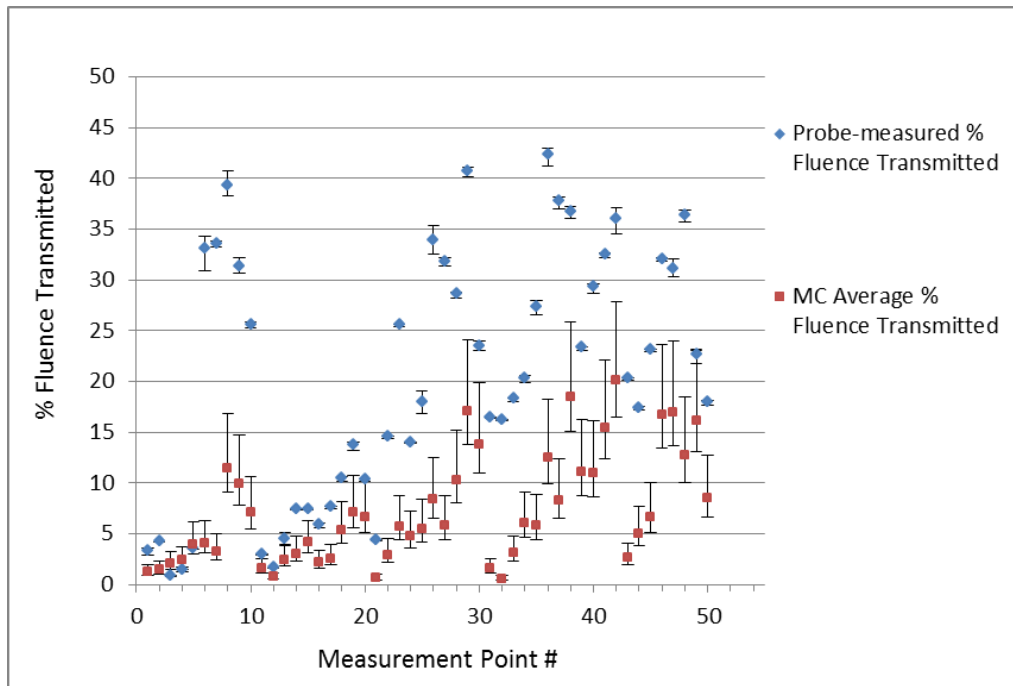


Figure 7.13 Comparison of % transmitted fluence between the calorimeter-probe measurements and the Monte Carlo. The error bars in the probe measurements represent the maximum and minimum intensities in the 3 averages, while the error bars in the Monte Carlo are the minimum and maximum fluences between the 3 optical models (see Table II).

Figure 7.13 shows that the Monte Carlo simulations compare closely to some of the probe measurement (example points 1-5 in phantom 1) while underestimating the transmission % for other points. Thus Monte Carlo overestimates the attenuation of fluence in the skull, while probe readings show a higher % power transmitted through the skull. The reason behind this difference is due to the differences in the bone density in the skull samples which were not included in the MC simulations. The MC simulations were done in a homogeneous brain phantom and assumed uniform density.

In order to demonstrate the feasibility of using CT image-guided skull boundaries for Monte Carlo simulation, we used the CT images to map the heterogeneity in distribution of bone voxels along with the geometry of boundaries. Figure 7.14 shows the comparison between the lateral fluence profiles (transmitted through the skull immersed in water) measured using the probe versus the Monte Carlo. The boundary conditions derived from the CT images is shown in figure 7.15. The fluence profiles were normalized to the maximum value measured at a depth of 5mm from the inner surface of the skull bone. The results show a close match between the beam spread simulated by the Monte Carlo and measured by the probe. This demonstrates the accuracy with which the

scattering properties of the bone were modelled, along with the CT image enhanced boundary conditions. The CT images of the skull sample also show the changing Hounsfield CT numbers across the bone which is the result of varying density of the bone structure. Thus compared to previous studies, we have used the CT images to account for the different optical path lengths along with boundary conditions. We have however, not accounted for the varying densities of the bone, which results in differences between the probe and the Monte Carlo fluences.

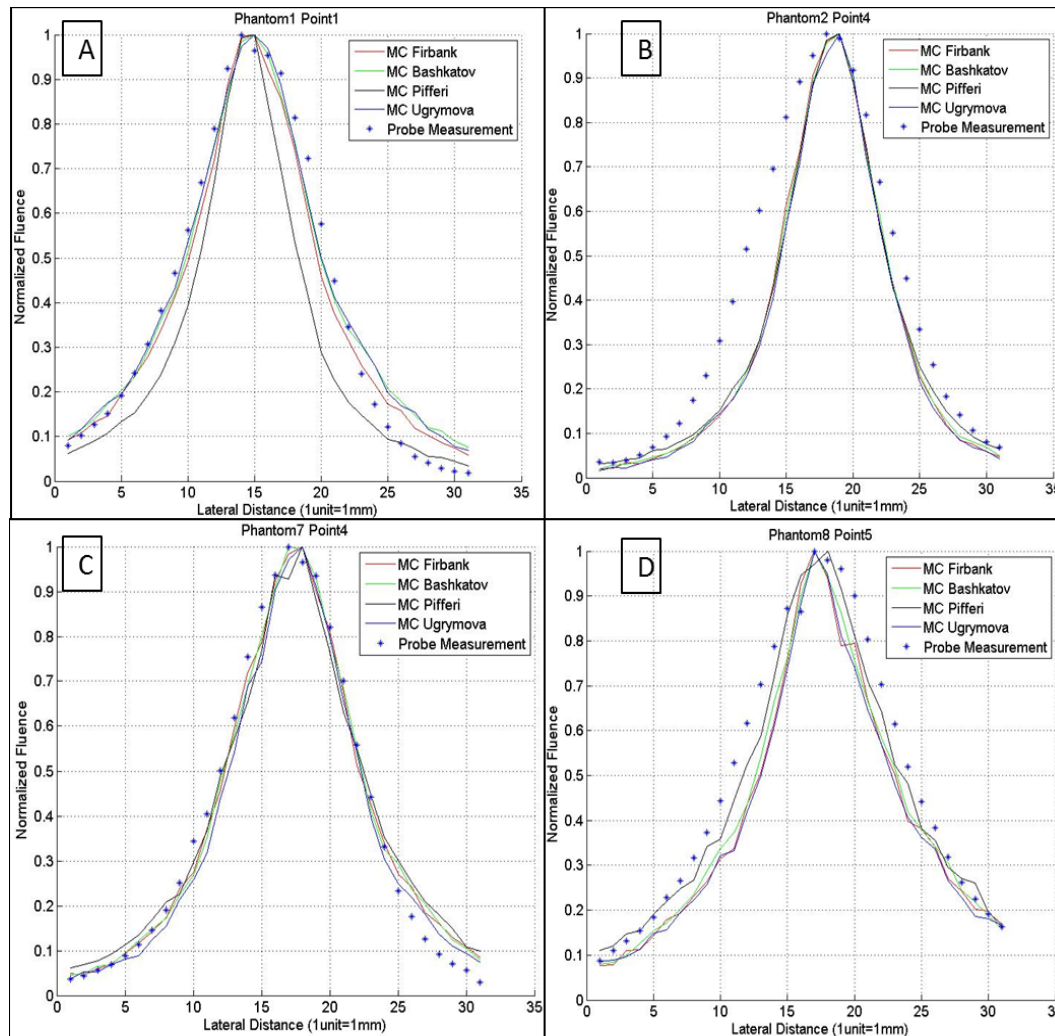


Figure 7.14 Comparison of lateral profiles measured using dosimetry probe with the Monte Carlo in water.

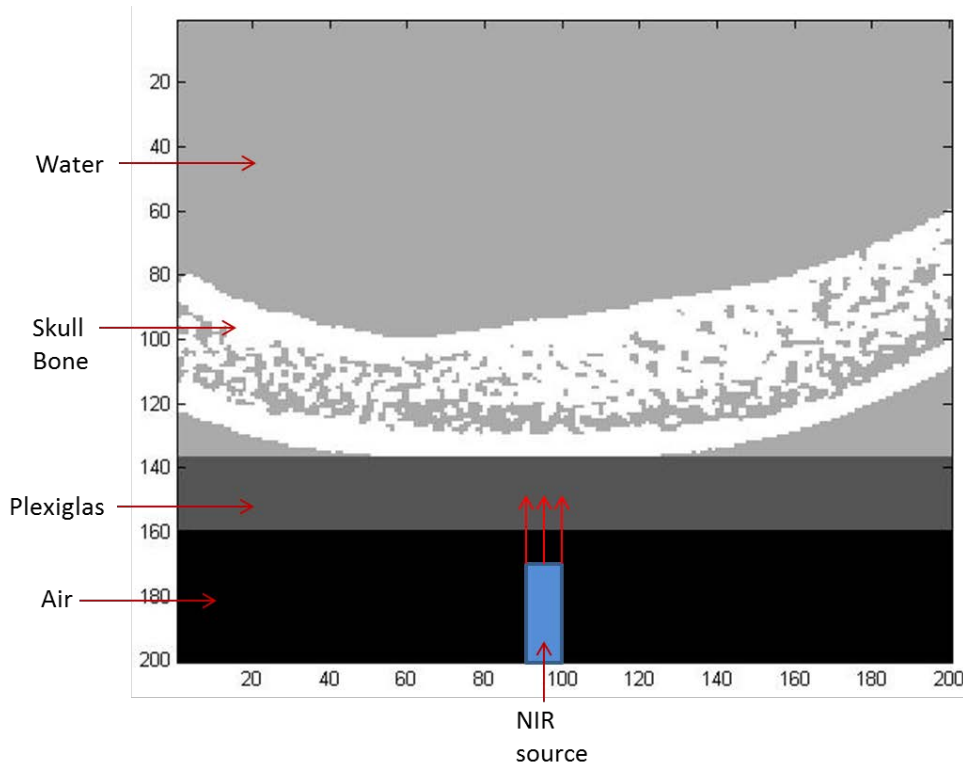


Figure 7.15 Boundary conditions simulated using the CT image-guided Monte Carlo.

(4) Discussion

The optical transmission study demonstrates the difficulties encountered in optical bone transmission studies. The Monte Carlo can accurately simulate photon attenuation in the skull only when all the optical properties and boundary conditions are simulated correctly. While the skull bone has been measured and modeled as a relatively homogeneous medium in optical simulation studies, the use of CT images shows that it is far from homogeneous with wide variations in bone densities at different anatomical regions and across subjects. This presents a complicated scenario to model the optical propagation of photons through the skull.

We demonstrated the accuracy of boundary conditions determined using CT images by comparing the lateral profiles between the Monte Carlo and the dosimetry probe. The close match between the profiles shows the accuracy of our simulations. Our study thus also reduced the error in measuring skull thicknesses using calipers, which often goes unnoticed in complex tissue structure. For example: an error in correctly measuring the skull thickness by a millimeter can result in errors of up to 40% in magnitude (seen from our MC data in figures 7.11, 7.12), depending on the boundary and illumination conditions. Thus any imaging or therapeutic technique needs to reduce the errors due to mismatch in the boundary conditions by using an anatomical imaging technique (such as CT) which can map different tissue boundaries.

To improve the match between the Monte Carlo and the measured fluence in skull models, we hypothesize that using bone density measurement technique such as quantitative CT can significantly improve the localization of high scattering bone voxels in the skull bone. The mapping of Hounsfield values of CT number can be directly linked to the bone density values by imaging bone density phantoms in the CT scanner. This would provide volumetric images of bone densities which can be converted (scaled) to the corresponding scattering absorption coefficients. The optical coefficient scaling will also need to be calibrated by measuring the optical properties of bone samples of known density.

Currently, we are developing iterative techniques to identify a relationship between HU and reduced scattering coefficient in bone on a voxel-wise basis. This is anticipated to improve the accuracy and precision in the transmission and lateral beam profile through the skull bone. A second line of investigation is the change in wavelength. This has the potential to reduce the effects of scattering but at the cost of water absorption. This tradeoff may help focus the beam for smaller depths beyond the skull within the brain tissue. However, the nanoparticle geometry will significantly change in order to provide stimulated drug release, and whether this is possible within macrophages is yet unexplored.

Tasks 1 d & e, 2c, and Task 3: These goals were unable to be met because of the issues with drug solubility (laptinib), light-triggered release, and probable leakage of doxorubicin from the NS@DNA@DOX nanocarriers. They all required the delivery of NS@DNA with stably loaded drug (DOX), which could be released by laser irradiation. The work around with the protein scaffold and femtosecond laser was not realized until late in the grant cycle.

4. KEY RESEARCH ACCOMPLISHMENTS: *Bulleted list of key research accomplishments emanating from this research. Project milestones, such as simply completing proposed experiments, are not acceptable as key research accomplishments. Key research accomplishments are those that have contributed to the major goals and objectives and that have potential impact on the research field. If there is nothing to report, simply state "Nothing to report."*

- Nanocarriers

Earlier experiments by the Rice Nanophotonics Group suggest that DNA dehybridization and cargo release occurred by a non-thermal release mechanism involving hot-electrons.[3] The collective oscillation of surface conduction electrons in metallic nanoparticles induced by light at a resonant frequency is known as a localized surface plasmon. Upon excitation, surface plasmons can decay radiatively by re-emitting photons of light or non-radiatively by the generation of local heat and/or energetic electrons. These energetic electrons are known as “hot-electrons” and the Rice group had hypothesized that the two DNA strands on the NS surface, which are negatively charged, were dehybridized by electrostatic interaction with the hot-electrons. It is now clear

from the experiments conducted as a part of this research that at particle concentrations achievable within a tumor, dehybridization of the DNA double helix is a thermal phenomenon. This resolves a fundamental question as to how the NS@DNA nanocarriers function to release cargo. It has also led to the testing of the femtosecond pulsed laser as a work-around, which releases cargo by breaking the Au-S bond at the nanoshell surface but results insufficient bulk heating to cause protein denaturation and subsequent tissue damage.

Many targeted therapies are small hydrophobic molecules; of note-this includes almost the entire family of tyrosine kinase inhibitors. We have developed a new strategy which uses the hydrophobic pocket of a protein scaffold on the nanoshell to load and from which to release hydrophobic drug molecules for controlled drug delivery that can be extended to myriad of cancers and chemotherapy drugs.

- Delivery of infrared irradiation to brain

As pointed out earlier, prior to our work there was little data on the amount and distribution of near infrared light able to be delivered through the skull and brain tissue. We have been able to model this using both the sheep skull and phantom as well as the Monte Carlo simulations. This has led us to proposing that multiple simultaneous sources of IR irradiation with or without intracranial intervention methods is likely to be required to deliver a sufficient fluence of irradiation to effect drug release.

We have demonstrated that using CT to map skull geometry and determine bone density enables a better understanding of the attenuation/scattering of NIR transmission through the skull. Based on our preliminary data and NIR transmission results, MC simulated results utilizing the average optical properties of the skull (accounting for thickness) obtained from literature underestimated the measured light distribution, primarily due to the heterogeneity in bone. Further work will be performed to provide a voxel-based method to account for this heterogeneity and improve our ability to predict the photon fluence rate distribution within the brain.

5. CONCLUSION: *Summarize the importance and/or implications with respect to medical and /or military significance of the completed research including distinctive contributions, innovations, or changes in practice or behavior that has come about as a result of the project. A brief description of future plans to accomplish the goals and objectives shall also be included.*

The delivery of effective therapeutics across the blood-brain barrier remains as critical a clinical challenge as it was when we first proposed our study. We remain convinced that the active delivery by macrophages of nanobound therapeutics to intracerebral malignancies is a promising strategy. Our studies have provided fundamental information on a number of aspects of the delivery of therapeutics by NS@DNA. 1. It is of key importance that the therapeutic is soluble and stable in aqueous solution if the DNA duplex is to be used as a carrier; 2. Dehybridization of DNA duplexes on the nanoshell surface is a thermal phenomenon when the NIR

source is a continuous wave laser. A femtosecond pulsed laser cleaves the Au-S at the nanoshell surface releasing the DNA. 3. Although doxorubicin is a DNA intercalating agent, it may distort the double helix such that it is not a secure cargo. 4. Other strategies are required to complex to the nanoshells small molecules that are poorly soluble in water. We have demonstrated that the combination of a protein scaffold in which to envelope the drug on the nanoshell and a femtosecond pulsed laser is a promising strategy for controlled drug delivery. 5. We have estimated, to the best of our knowledge for the first time, the amount and distribution of near infrared light able to be delivered through the skull and brain tissue. We have also begun to understand how inhomogeneity of the skull bone with regard to thickness and density scattering NIR and how this may be modeled to optimize transmission. While we have demonstrated substantial attenuation of the IR irradiation on its pathway through the skull and brain phantom, our results have prompted us to consider utilizing multiple NIR sources.

Although this marks the end of our DoD funding, we hope to continue to pursue this novel delivery method. Should we secure future funding, we will determine if and to what extent DOX is leaking from the DNA duplex; presuming that DNA duplex distortion is responsible for the leakage, we will search for an alternate drug that can be maintained within the dsDNA@NS complex until release is triggered; and we will follow up on our observation that hydrophobic drugs can be delivered in and released from protein pockets. With regard to delivering sufficient IR irradiation to the brain, the following are strategies and fields of investigation that we hope to pursue:

- (1) Place multiple sources to avoid thicker regions of gray matter and overall skull density.
- (2) Increase the number of sources around the skull in order to get the fluence to plateau (instead of exponentially decay) at larger depths in the brain.
- (3) Examine the possibility of directional scattering in neuronal fibers as a means to increase NIR depth penetration.
- (4) Given the diffusive nature of light, the beam surface area can be increased to reduce surface heating near the surface of the brain without too much loss in the fluence at depth.
- (5) Examine different wavelengths. For example, look at some IR windows. The advantage is less scattering at the cost of water absorption. The goal is to determine how much of an improvement on fluence localization can be achieved.
- (6) Continue to study the dispersive effects for pulse laser pulses.

6. PUBLICATIONS, ABSTRACTS, AND PRESENTATIONS

a. List all manuscripts submitted for publication during the period covered by this report resulting from this project. Include those in the categories of lay press, peer-reviewed scientific journals, invited articles, and abstracts. Each entry shall include the author(s), article title, journal name, book title, editors(s), publisher, volume number, page number(s), date, DOI, PMID, and/or ISBN. Journal publications

1. Lay Press: Nothing to report

2. *Peer-Reviewed Scientific Journals:*

- [1] Verleker AP, Fang Q, Choi M-R, Clare S, Stantz KM. An empirical approach to estimate near-infra-red photon propagation and optically induced drug release in brain tissues. Proc SPIE BiOS 9308-29: 1-8, 2015 (doi: 10.1117/12.2079991)
- [2] Verleker AP, Fang Q, Choi M-R, Clare S, Stantz KM. An Optical Therapeutic Protocol to treat brain metastasis by mapping NIR activated drug release: a Pilot Study. Proc IEEE MIC (M19-96): 107, 2014.
- [3] Verleker AP, Shaffer M, Fang Q, Choi MR, Clare S, Stantz KM: Optical dosimetry probes to validate Monte Carlo and empirical-method-based NIR dose planning in the brain. Appl Opt 2016, 55(34):9875-9888.
- [4] Goodman AM, Hogan NJ, Gottheim S, Li C, Clare SE, Halas NJ: Understanding Resonant Light-Triggered DNA Release from Plasmonic Nanoparticles. ACS Nano 2017, 11(1):171-179.

3. *Invited Articles: Nothing to report*

4. *Abstracts: Nothing to report*

b. *List presentations made during the last year (international, national, local societies, military meetings, etc.).*

Use an asterisk () if presentation produced a manuscript.*

Nothing to report

7. **INVENTIONS, PATENTS AND LICENCES**

Nothing to report

8. **REPORTABLE OUTCOMES:**

Nothing to report

9. OTHER ACHIEVEMENTS: *This list may include degrees obtained that are supported by this award, development of cell lines, tissue or serum repositories, funding applied for based on work supported by this award, and employment or research opportunities applied for and/or received based on experience/training supported by this award.*

This project has directly contributed to the research thesis of Akshay Verleker at Purdue University, who will be graduating with a doctorate in 2016. It provided him the opportunity to submit and obtain a Purdue Research Foundation Grant (2014-2015), a Center for Cancer Research Travel Award (2014), and the Graduate Student Travel (Compton) Award from the College of Health and Human Sciences (HHS) (2015). These latter awards provided Akshay the opportunity to present this research at the IEEE Medical Imaging (NSS/MIC 2014) and SPIE BiOS (2015) conferences, where, at the former meeting, he was awarded the Nuclear and Plasma Sciences Society Phelps continuing education grant to pursue continuing education courses in the field of particle and photon transport and imaging sciences.

This project also directly contributed to the doctoral thesis of Amanda Goodman, who graduated with a Ph.D. in Chemistry from Rice University in May of 2016.

10. REFERENCES

1. Choi M-R, Bardhan R, Stanton-Maxey KJ, Badve S, Nakshatri H, Stantz KM, Cao N, Halas NJ, Clare SE: **Delivery of nanoparticles to brain metastases of breast cancer using a cellular Trojan horse.** *Cancer Nanotechnology* 2012.
2. Choi MR, Stanton-Maxey KJ, Stanley JK, Levin CS, Bardhan R, Akin D, Badve S, Sturgis J, Robinson JP, Bashir R *et al*: **A cellular Trojan Horse for delivery of therapeutic nanoparticles into tumors.** *Nano Lett* 2007, **7**(12):3759-3765.
3. Huschka R, Zuloaga J, Knight MW, Brown LV, Nordlander P, Halas NJ: **Light-induced release of DNA from gold nanoparticles: nanoshells and nanorods.** *J Am Chem Soc* 2011, **133**(31):12247-12255.
4. Goodman AM, Hogan NJ, Gottheim S, Li C, Clare SE, Halas NJ: **Understanding Resonant Light-Triggered DNA Release from Plasmonic Nanoparticles.** *ACS Nano* 2017, **11**(1):171-179.
5. Verleker AP, Fang Q, M-R. C, Clare S, Stantz KM: **An empirical approach to estimate near-infra-red photon propagation and optically induced drug release in brain tissues.** *Proc SPIE BiOS* 2015, **9308-29**:1-8.
6. Verleker AP, Shaffer M, Fang Q, Choi MR, Clare S, Stantz KM: **Optical dosimetry probes to validate Monte Carlo and empirical-method-based NIR dose planning in the brain.** *Appl Opt* 2016, **55**(34):9875-9888.
7. Van der Zee P, Essenpreis M, Delpy DT: **Optical properties of brain tissue.** In: *OE/LASE'93: Optics, Electro-Optics, & Laser Applications in Science & Engineering International Society for Optics and Photonics 1993*; 1993.
8. Firbank M, Hiraoka M, Essenpreis M, Delpy DT: **Measurement of the Optical-Properties of the Skull in the Wavelength Range 650-950 Nm.** *Phys Med Biol* 1993, **38**(4):503-510.
9. Verleker AP, Fang Q, Choi M-R, Clare S, Stantz KM: **An Optical Therapeutic Protocol to treat brain metastasis by mapping NIR activated drug release: a Pilot Study.** *Proc IEEE MIC* 2014, **(M19-96)**:107.
10. Fang Q, Boas DA: **Monte Carlo simulation of photon migration in 3D turbid media accelerated by graphics processing units.** *Opt Express* 2009, **17**(22):20178-20190.
11. Narr KL, Bilder RM, Toga AW, Woods RP, Rex DE, Szeszko PR, Robinson D, Sevy S, Gunduz-Bruce H, Wang YP *et al*: **Mapping cortical thickness and gray matter concentration in first episode schizophrenia.** *Cereb Cortex* 2005, **15**(6):708-719.
12. Ajilore O, Narr K, Rosenthal J, Pham D, Hamilton L, Watari K, Elderkin-Thompson V, Darwin C, Toga A, Kumar A: **Regional cortical gray matter thickness differences associated with type 2 diabetes and major depression.** *Psychiat Res-Neuroim* 2010, **184**(2):63-70.
13. Jagdeo JR, Adams LE, Brody NI, Siegel DM: **Transcranial red and near infrared light transmission in a cadaveric model.** *PLoS One* 2012, **7**(10):e47460.
14. Lychagov VV, Tuchin VV, Vilensky MA, Reznik BN, Ichim T, De Taboada L: **Experimental study of NIR transmittance of the human skull.** In: *Proc SPIE 6085, Complex Dynamics and Fluctuations in Biomedical Photonics III*, 60850T: 2006; 2006.
15. Stolik S, Delgado JA, Perez A, Anasagasti L: **Measurement of the penetration depths of red and near infrared light in human "ex vivo" tissues.** *J Photochem Photobiol B* 2000, **57**(2-3):90-93.
16. Tauber S, Baumgartner R, Schorn K, Beyer W: **Lightdosimetric quantitative analysis of the human petrous bone: experimental study for laser irradiation of the cochlea.** *Lasers Surg Med* 2001, **28**(1):18-26.
17. von Wedel H, Calero L, Walger M, Hoenen S, Rutwalt D: **Soft-laser/Ginkgo therapy in chronic tinnitus. A placebo-controlled study.** *Adv Otorhinolaryngol* 1995, **49**:105-108.

18. Plucinski J, Frydrychowski AF, Kaczmarek J, Juzwa W: **Theoretical foundations for noninvasive measurement of variations in the width of the subarachnoid space.** *J Biomed Opt* 2000, **5**(3):291-299.
19. Young AE, Germon TJ, Barnett NJ, Manara AR, Nelson RJ: **Behaviour of near-infrared light in the adult human head: implications for clinical near-infrared spectroscopy.** *Br J Anaesth* 2000, **84**(1):38-42.
20. Bashkatov AN, Genina EA, Kochubey VI, Tuchin VV: **Optical properties of human cranial bone in the spectral range from 800 to 2000 nm.** In: *Saratov Fall Meeting 2005: Optical Technologies in Biophysics and Medicine VII*: 2006; 2006: 616310-616311 to 616310-616310.
21. Pifferi A, Torricelli A, Taroni P, Bassi A, Chikoidze E, Giambattistelli E, Cubeddu R: **Optical biopsy of bone tissue: a step toward the diagnosis of bone pathologies.** *J Biomed Opt* 2004, **9**(3):474-480.
22. Ugryumova N, Matcher SJ, Attenburrow DP: **Measurement of bone mineral density via light scattering.** *Phys Med Biol* 2004, **49**(3):469-483.
23. <http://demonstrations.wolfram.com/ParametricEquationOfACircleIn3D/>.

11. APPENDICIES: *Attach all appendices that contain information that supplements, clarifies or supports the text. Examples include original copies of journal articles, reprints of manuscripts and abstracts, a curriculum vitae, patent applications, study questionnaires, and surveys, etc.*

- a. Manuscript: Proc SPIE BiOS 9308-29: 1-8, 2015
- b. Manuscript: Proc IEEE MIC (M19-96): 107, 2014.
- c. Manuscript: Appl Opt 2016, 55(34):9875-9888.
- d. Manuscript: ACS Nano 2017, 11(1):171-179.

An empirical approach to estimate near-infra-red photon propagation and optically induced drug release in brain tissues

Akshay Prabhu Verleker^{*a}, Qianqian Fang^b, Mi-Ran Choi^c, Susan Clare^c and Keith M. Stantz^a

^aDepartment of Health Sciences, HAMP 1263, 550 Stadium Mall Drive, West Lafayette, IN, USA

47907-2051; ^bMartinos Ctr. for Biomedical Imaging, Harvard Medical School, Charleston, MA

USA, ^cFeinberg School of Medicine, Northwestern University, Chicago, IL.

ABSTRACT

Purpose: The purpose of this study is to develop an alternate empirical approach to estimate near-infra-red (NIR) photon propagation and quantify optically induced drug release in brain metastasis, without relying on computationally expensive Monte Carlo techniques (gold standard). Targeted drug delivery with optically induced drug release is a non-invasive means to treat cancers and metastasis. This study is part of a larger project to treat brain metastasis by delivering lapatinib-drug-nanocomplexes and activating NIR-induced drug release. The empirical model was developed using a weighted approach to estimate photon scattering in tissues and calibrated using a GPU based 3D Monte Carlo. The empirical model was developed and tested against Monte Carlo in optical brain phantoms for pencil beams (width 1mm) and broad beams (width 10mm). The empirical algorithm was tested against the Monte Carlo for different albedos along with diffusion equation and in simulated brain phantoms resembling white-matter ($\mu_s'=8.25\text{mm}^{-1}$, $\mu_a=0.005\text{mm}^{-1}$) and gray-matter ($\mu_s'=2.45\text{mm}^{-1}$, $\mu_a=0.035\text{mm}^{-1}$) at wavelength 800nm. The goodness of fit between the two models was determined using coefficient of determination (R-squared analysis). Preliminary results show the Empirical algorithm matches Monte Carlo simulated fluence over a wide range of albedo (0.7 to 0.99), while the diffusion equation fails for lower albedo. The photon fluence generated by empirical code matched the Monte Carlo in homogeneous phantoms ($R^2=0.99$). While GPU based Monte Carlo achieved 300X acceleration compared to earlier CPU based models, the empirical code is 700X faster than the Monte Carlo for a typical super-Gaussian laser beam.

Keywords: Empirical algorithm for light propagation, NIR photon propagation, Monte Carlo simulation, Optical therapy, Optically induced drug release, Tissue Optics, Light Scattering

1. INTRODUCTION

Optical therapy using NIR light delivery requires the estimation of photon fluence in tissues and heterogeneous media. This study is a part of a larger project which seeks to selectively deliver macrophages laden with lapatinib-gold-nanocomplex drug molecules to brain metastasis with over-expressed HER2+ receptors and activate targeted drug release using NIR photons.^{1,2} The effectiveness of achieving a targeted drug delivery and optically activated drug release with a Monte Carlo based optical therapeutic protocol has been demonstrated in previous studies.¹⁻⁵ The design of an optical therapeutic protocol requires the evaluation of various illumination conditions such as the angles of incidence and source positions for optimum drug release in the metastatic lesions of the brain.⁵ While the Monte Carlo is the gold standard for photon estimation in 3D media, it is computationally expensive to be used over a large number of iterations. Hence there is a need for a computationally efficient evaluation algorithm which can reduce the possible illumination conditions to a few iterations, while minimizing error in fluence estimation. This algorithm should also be able to interface seamlessly with any imaging modality system to effectively localize fluence distributions with respect to anatomical and physiological information provided by imaging modalities such as CT, Ultrasound, PET, MRI, etc. In the current work we have developed a fast voxel based empirical approach which can estimate photon fluence in the brain and evaluate different illuminations before using Monte Carlo as a final tool for validation. Being a 3D voxel based method; this algorithm can be easily integrated with other imaging modalities to evaluate fluence distributions in the brain and other tissues, by co-registering 3D fluence images with images from CT, MR, Ultrasound, etc.

Light propagation studies in 3D media rely on the use of Monte Carlo simulations as the gold standard, to estimate the photon fluence distribution in three dimensional units of volume known as voxels. The Monte Carlo model uses probability distribution to generate a random walk of photons in three dimensional media and relies on generating a large number of events to produce statistically significant fluence distributions in optical media with specific absorption and

scattering properties.⁶⁻¹⁰ The photon fluence deposited (and traversing) within each voxel depends on the specified optical properties assigned by the user, such as the absorption coefficient (μ_a), scattering coefficient (μ_s), anisotropy factor (g) and refractive index (n). The traditional Monte Carlo software is computationally expensive as it relies on generating millions of photons and tracking each photon as it propagates through the medium. Recent research in GPU based Monte Carlo by the Fang group has resulted in speeds up to 300X faster than the traditional CPU based versions.⁶ However for large optical datasets, such as those obtained and translated from CT or MR images, and under wide beam illumination conditions, the Monte Carlo suffers from slow computation speeds due to large photon propagation times in highly scattering tissues. This results in a drawback and slowdown in the process of planning targeted light delivery to specific regions within the human body. In this study we have designed an alternate empirical approach to light propagation which can estimate the photon fluence in tissues in complex three dimensional media to provide a fast preliminary approach to light estimation while planning targeted NIR light delivery. The purpose of this study is to devise a fast means to estimate NIR photon fluence under different illumination conditions in an optical treatment plan before using Monte Carlo for final verification and corrections.

The empirical approach estimates the fluence distribution in a voxelated medium by using a weighted approach to fluence propagation from one layer to the next. The assumption used is that the photon fluence in a voxel is a weighted sum of the fluences in the neighboring voxels of the preceding layer. The weights are arbitrarily assigned to each voxel based on its optical properties, mainly the scattering coefficient. The accuracy of the empirical approach depends on the optimization method used to estimate the weights for each set of optical properties. The empirical approach simulates photon scatter by dividing the fluence into scattering vectors in the forward and diagonal directions, while photon absorption is simulated using the Beer Lambert's rule.¹¹ An optimization routine is used to estimate the weights assigned to each voxel by comparing with a pencil beam simulated by the Monte Carlo. In this study we estimated the weights for typical brain tissues such as Gray Matter, White Matter, Skull bone and Astrocytoma with known optical properties.¹²⁻¹⁴ These weights were then tested in homogeneous and heterogeneous brain phantoms under pencil beam and broad beam illumination. The Monte Carlo has been used as the gold standard for evaluating the performance of this algorithm. The 3D GPU based Monte Carlo, developed by the Fang group, has an acceleration of 300X over the traditional CPU based version⁶, while the Empirical approach was seen to be 700X faster than the GPU based Monte Carlo for a super-Gaussian beam.

2. MATERIALS AND METHODS

2.1 Algorithm Design

The empirical approach approximates the photon scatter from one voxel to the next by assigning weights to the scattering directions. The main goal of this algorithm is to approximate the total scattering events within a voxel into 14 component vectors. Since tissues are mostly forward propagating with anisotropies approximately equal to or greater than 0.9, it can be assumed that most photon scatter directions can be approximated into forward and diagonal vectors. Hence, each scattering event is divided into 4 scattering components: one forward component with the wt1 and 4 diagonal components with weight wt2 as shown in the figures. The fluence enters a voxel from 14 neighboring voxels. Each incoming fluence component is then scattered into one forward component and 4 diagonal components. The total fluence in each individual direction is accumulated and absorbed within a voxel based on the absorption coefficient. The remaining fluence then exits the voxel into the 14 neighboring voxels. It is important to note that the fluence entering a voxel is equal to the sum of fluence absorbed within the voxel and the fluence exiting the voxel. This is achieved by ensuring that the sum of the weights used is equal to one [i.e. $(wt1 + 4 \times wt2) = 1$].

The steps of the algorithm can be summarized as follows:

- 1) Assign the incident photon fluence (e.g. Gaussian beam) to the first layer of voxels. Here we have assumed that the photons enter the volume (of dimensions $dim1 \times dim2 \times dim3$) at $z=1$ (first layer).
- 2) Begin the propagation from layer $z=1$ to $z=dim3$.

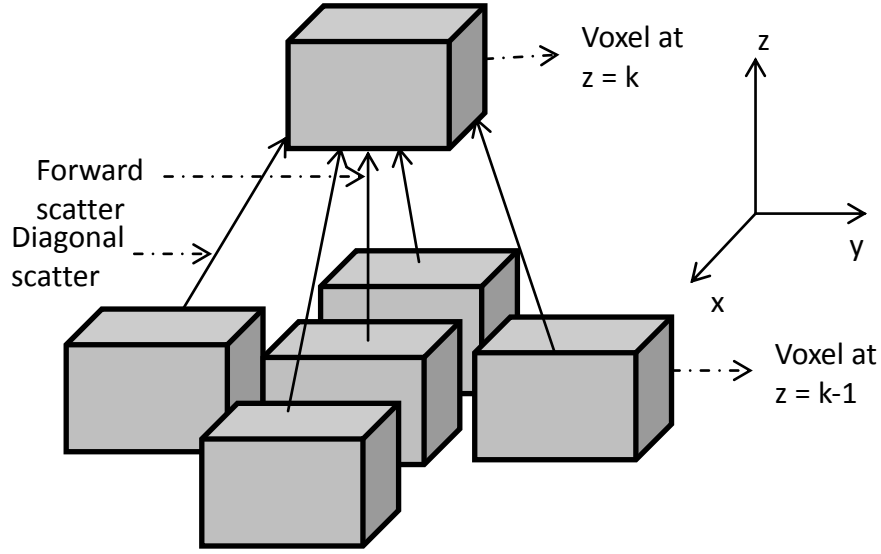


Figure 1: Step1: Modelling photon propagation. The empirical algorithm propagates photons from one layer to the next by assigning weights to fluences in voxels of the preceding layer. The figure shows forward and diagonal scatter from layer $k-1$ to k .

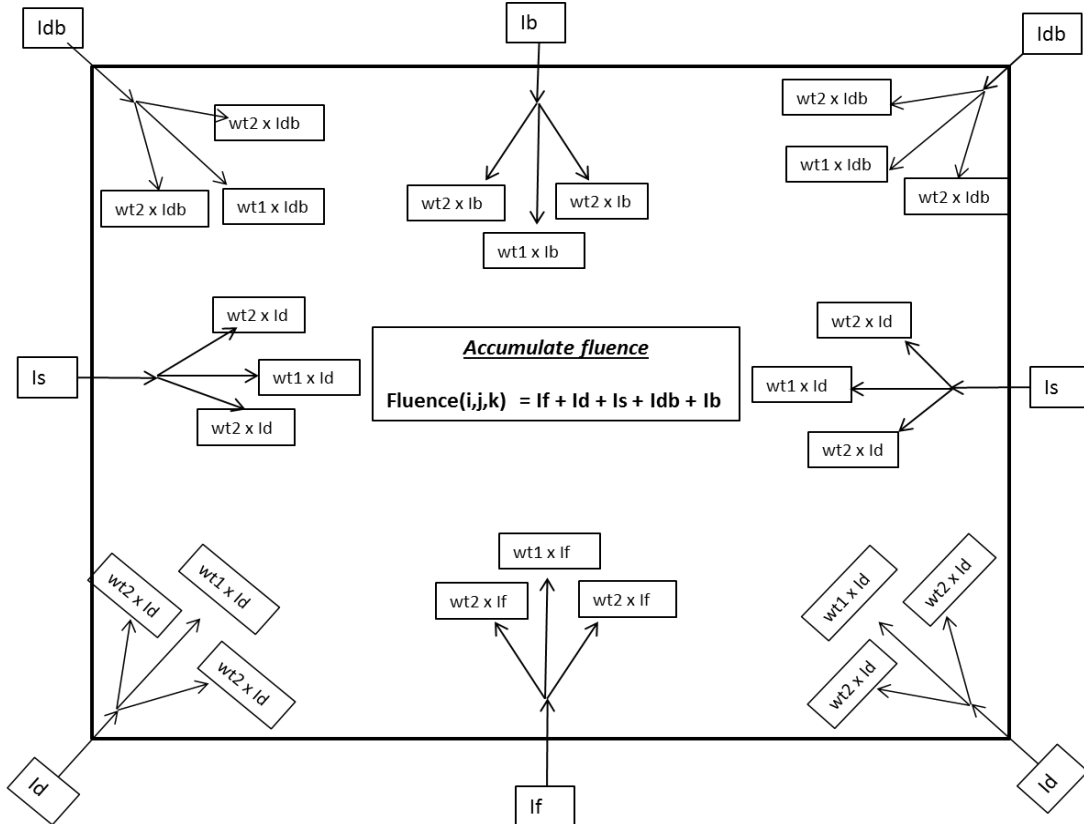


Figure2: Step2: Fluence Accumulation within a voxel. The figure shows the accumulation of directional photon fluences from neighboring voxels, namely the forward (If), diagonal upwards (Id), diagonal downwards (Idb) and side (Is) scattered component fluences. The fluence entering a voxel is scattered into 5 directions: 4 diagonal directions with the weight $wt2$ and one forward direction with the forward weight $wt1$. The weights are chosen such $(wt1 + 4 \times wt2) = 1$.

3) For every voxel in a layer $z=k$:

- a) Calculate the 14 directional components from the incident photon fluence. For the first layer the fluence is assumed to be in the forward direction. The fluence from neighboring voxels is accumulated in each direction as follows:

$$\text{Forward Component} = I_f(x,y,z) = \sum (\text{forward components} \times \text{wt1}) + \sum (\text{forward diagonal components} \times \text{wt2})$$

$$\text{Forward Diagonal Component} = I_d(x,y,z) = \sum (\text{forward components} \times \text{wt2}) + \sum (\text{forward diagonal components} \times \text{wt1}) + \sum (\text{side components} \times \text{wt2})$$

$$\text{Side Component} = I_s(x,y,z) = \sum (\text{forward diagonal components} \times \text{wt2}) + \sum (\text{side components} \times \text{wt1}) + \sum (\text{backward diagonal components} \times \text{wt2})$$

$$\text{Backward Diagonal Component} = I_{db}(x,y,z) = \sum (\text{side components} \times \text{wt2}) + \sum (\text{backward diagonal components} \times \text{wt1}) + \sum (\text{backward component} \times \text{wt2})$$

$$\text{Backward Component} = I_b(x,y,z) = \sum (\text{backward component} \times \text{wt1}) + \sum (\text{backward diagonal components} \times \text{wt2})$$

$$\text{Total Fluence} = I(x,y,z) = I_f(x,y,z) + \sum I_d(x,y,z) + \sum I_s(x,y,z) + \sum I_{db}(x,y,z) + I_b(x,y,z)$$

The forward component (I_f) refer to the direction of propagation of the main fluence beam (or ‘forward scatter’), while the backward component (I_b) refers to the 180 degree scatter (or backscatter) which is opposite to the incident photon fluence vector. The diagonal components are divided into 4 forward diagonals (I_d) and 4 backward diagonals (I_{db}). Thus each direction is associated with a neighboring voxel. The total fluence within a voxel is obtained by summing up the fluences in each component directions. Note that the above directions can be arbitrarily chosen according to the experimental setup or at the convenience of the user.

- b) Simulate photon absorption by depositing the photon fluence into the voxel based on its absorption coefficient (μ_a):
 $\text{Absorbed Fluence} = I_{abs}(x,y,z) = I(x,y,z) \times \{1 - \exp(-\mu_a \times dl)\}$
 (where dl = path length)

4) Once fluences have been accumulated over the current layer, increment z to proceed to the next layer. Thus by repeating this process for all layers and updating the directional components of fluences for every voxel, the empirical approach propagates the fluence from one layer to the next across the volume.

2.2 Optimization Phase (Pencil beam simulations)

Optical properties of the medium (scattering coefficient μ_s , anisotropy factor g , absorption coefficient μ_a , albedo a') define the photon fluence generated by the empirical approach. The weights assigned to each voxel depend on its scattering property, while the absorption coefficient determines the amount of fluence deposited and energy absorbed. The weights were derived during the optimization phase by comparing the exponential attenuation profiles of the Empirical approach to the Monte Carlo using root mean square error and coefficient of correlation criteria. Previous studies have shown the applications as well as the limitations of the diffusion equation in estimating photon fluence for media with low albedos.^{10,15-22} In this study we first tested the performance of the Empirical approach with respect to the Monte Carlo and the diffusion equation for media with different albedos from 0.7 to 0.99. The albedo (a')¹⁰ is given by the equation:

$$a' = \frac{(1 - g)\mu_s}{(1 - g)\mu_s + \mu_a} \quad (1)$$

Next, the empirical algorithm was trained to derive the forward ($wt1$) and diagonal ($wt2$) weights for brain tissues such as white matter ($\mu_a=0.005\text{mm}^{-1}$, $\mu_s=55\text{mm}^{-1}$, $g=0.85$, $a'=0.9994$), gray matter ($\mu_a=0.035\text{mm}^{-1}$, $\mu_s=70\text{mm}^{-1}$, $g=0.965$, $a'=0.9859$), skull bone ($\mu_a=0.024\text{mm}^{-1}$, $\mu_s=18.4\text{mm}^{-1}$, $g=0.9$, $a'=0.9871$) and tumor (astrocytoma) ($\mu_a=0.3\text{mm}^{-1}$, $\mu_s=500\text{mm}^{-1}$, $g=0.88$, $a'=0.995$).¹²⁻¹⁴ A pencil beam was simulated using the Monte Carlo using the known optical

properties of each of the above brain tissues.¹²⁻¹⁴ The Empirical algorithm was then trained to emulate the same exponential decay profile by incrementing the forward scattering weight from 0 to 1, while the diagonal was adjusted to ensure that $wt1 + (4 \times wt2) = 1$. The weights derived from the optimization phase were used for the broad beam simulations in homogeneous and heterogeneous phantoms.

2.3 Broad beam simulations in Homogeneous and Heterogeneous Brain phantoms

The empirical weights obtained from the pencil beam training phase were used for further simulations using broad beams in homogeneous and heterogeneous brain phantoms. The Gaussian beam generated by the Monte Carlo was matched to that of the Empirical algorithm. An optical property map was generated in which every voxel was assigned a specific weight and absorption coefficient based on the tissue property. The Gaussian beam distribution was first tested in homogenous phantoms of each of the brain tissues: skull bone, gray matter, white matter and tumor (astrocytoma). The weights derived from the pencil beam optimization phase were used in the broad beam simulation to test their validity. Next, a software phantom of a human head with 15 cm diameter was created using concentric spheres to denote the different tissue types. The incident beam had a Gaussian profile. The fluence profiles and absorption energy maps generated Monte Carlo and Empirical approach were compared. The execution times for generation of a broad beam profile was compared between the two models.

3. RESULTS

3.1 Pencil beam simulations (Optimization Phase)

In this study, the empirical software was trained in an iterative process by comparing its exponential decay profiles to that of the Monte Carlo using pencil beams in optically homogeneous media. The Empirical approach had a better fit to the Monte Carlo as compared to the diffusion equation, especially for low albedos. The weights $wt1$ and $wt2$ were derived and optimized for each of the brain tissues (white matter, gray matter, skull bone and tumor) by using the profile which best matched the Monte Carlo. The absorption coefficient assigned was the same as has been obtained from previous studies. Figure 3 shows the pencil beam simulation profiles obtained by the Monte Carlo and the Empirical algorithm.

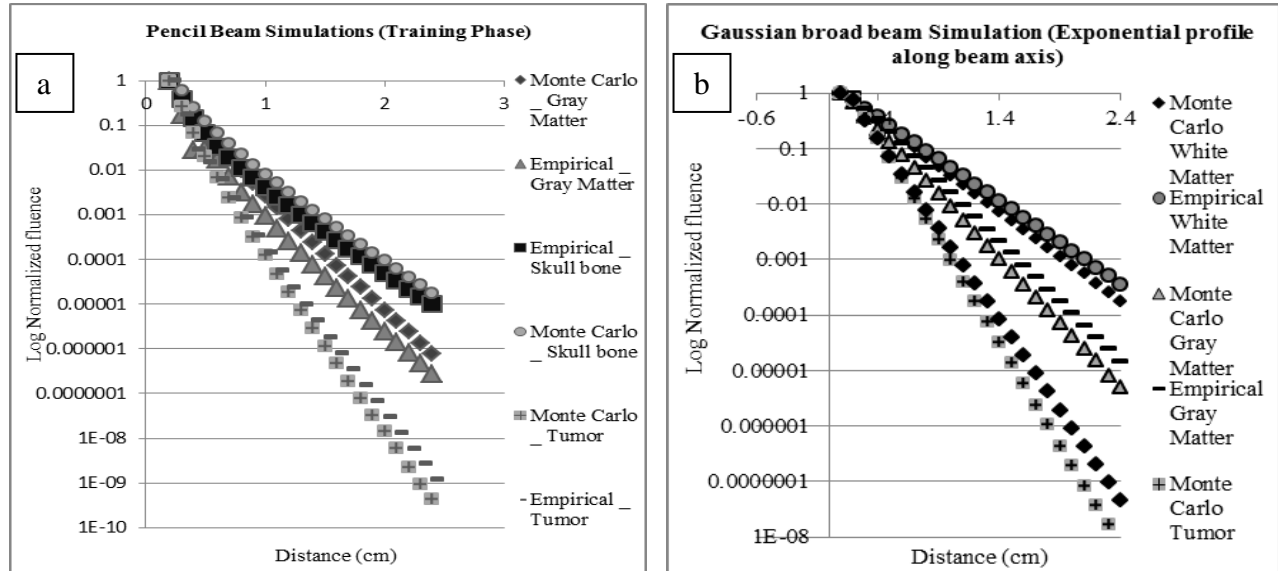


Figure 3. (a) Training Phase. The figure shows pencil beam profiles along z axis between the Monte Carlo and the Empirical algorithm. The empirical algorithm is trained to emulate the same exponential fluence attenuation as that of the Monte Carlo by adjusting and optimizing the weights $wt1$ and $wt2$. (b) Broad beam simulations: The empirical algorithm was compared to the Monte Carlo for incident Gaussian beam profiles. Overall the fluence profile of the Empirical closely followed that of the Monte Carlo.

The pencil beam simulations show that the empirical algorithm can be effectively trained to emulate the fluence attenuation for pencil beams generated using Monte Carlo in a homogeneous tissue medium. The pencil beams obtained by the empirical closely match the Monte Carlo with R-square value of 0.99. Since this study looks at the effectiveness of using the empirical approach to quantify optical drug release in the brain, we have obtained the weights mainly for brain tissues. These weights are then used to validate the fluence for broad beams such as Gaussian and super Gaussian beams.

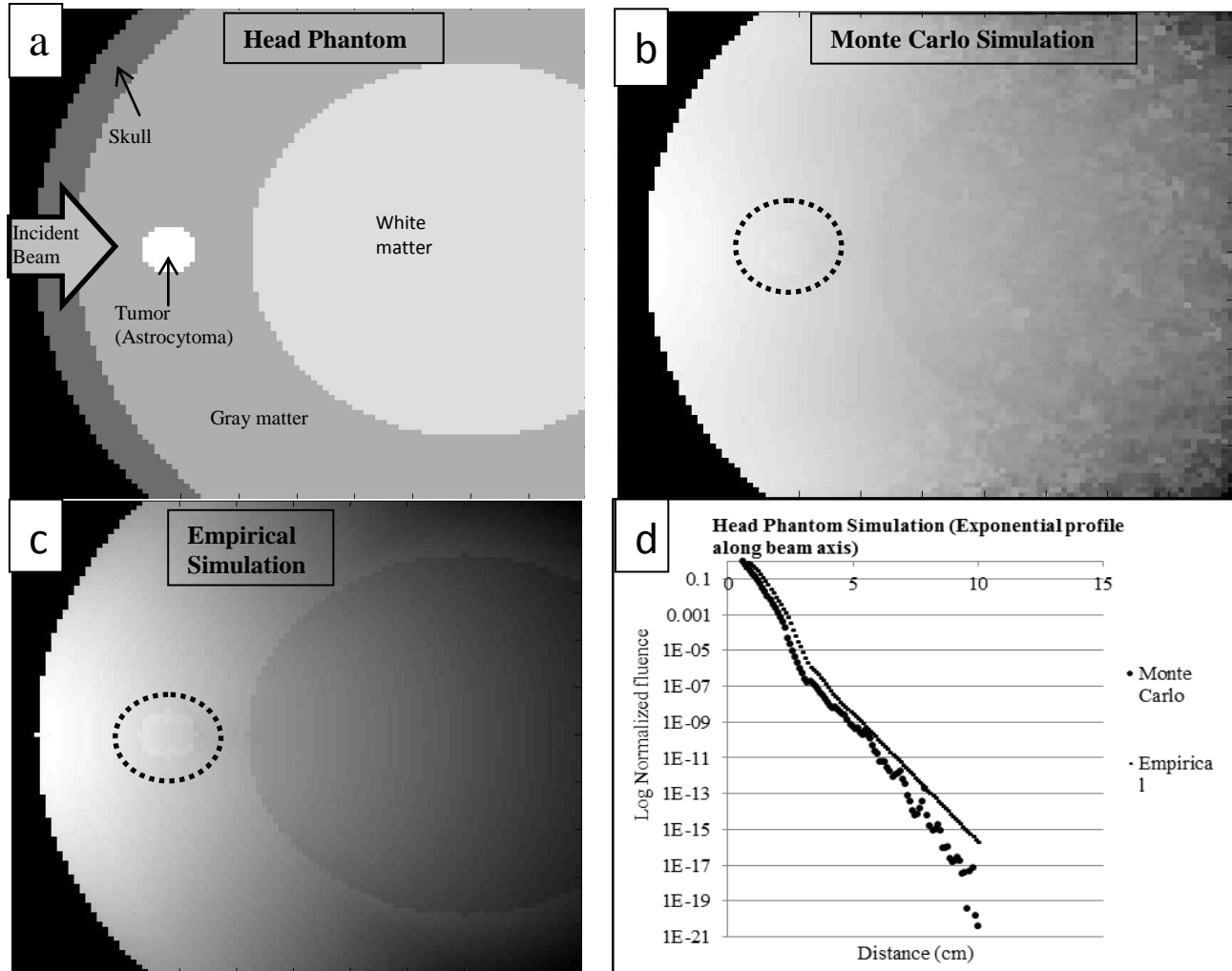


Figure 5: Validation in a Heterogeneous Head Phantom simulation. (a) Design of the head phantom. The image is obtained from the voxel properties/tissue types assigned in a 100 x 100 x 100 volume of 1mm voxel size. (b) Photon energy absorbed as obtained by the Monte Carlo simulation of a Gaussian beam traversing through the head phantom. (c) Empirical energy absorbed profile. (d) Photon fluence attenuation in along the incident beam axis at the beam center. The weights obtained from the training phase were assigned to the voxels in the empirical algorithm.

3.2 Broad beam simulations (Gaussian beam)

Figure 3(b) compares the Gaussian beam attenuation along beam axis between the Empirical and the Monte Carlo. The Gaussian beam analysis shows that the empirical approach can emulate the Monte Carlo fluence for broad beam simulations. The acceleration provided by the Empirical algorithm was approximately 700X as compared to the Monte Carlo for a broad beam. This however depends on the tissue optical properties as the Monte Carlo simulations take longer execution times for high scattering tissues and are relatively fast for low scattering media. The differences between the Monte Carlo and the Empirical approaches can be significant at larger depths and hence need to be accounted for.

3.3 Heterogeneous Brain phantom simulations (Gaussian beam)

Figure 5 shows the fluence profiles and absorption energy maps generated Monte Carlo and Empirical approach for the head phantom. The errors/differences induced by the tissue heterogeneity are seen between the two models and needs to be studied further. However it is seen that the exponential profile of the Empirical more or less follows that of the Monte Carlo. In the absorbed energy images generated in Figure 5 (b) and (c), the profile of the tumor absorption is clearly visible in the Empirical and can be demarcated within the Monte Carlo. The Monte Carlo also generates a large amount of statistical noise at larger depths which is not seen in the Empirical model. The time for execution of the Monte Carlo for a broad beam in the heterogeneous head phantom is 3.01 seconds as compared to 9 hours and 47 minutes required by the Monte Carlo. Thus the Empirical model gives a smoother approximation of the fluence profile as compared to the Monte Carlo at a fraction of the time (11701X acceleration) and thus could provide an alternative to the Monte Carlo in cases where an approximate idea of fluence distribution is needed while planning optical therapy.

4. DISCUSSION

4.1 Implications and Future Research

The current study has looked at providing an alternate voxel based approach of estimating photon fluence in 3D heterogeneous tissues besides the diffusion approximation and Monte Carlo methods. The Monte Carlo is by far the most accurate method for simulating photon deposition in tissues. However due to the large execution times, even after being implemented on parallel processing platforms, there is a need for a method for fast preliminary estimation of fluence within a certain error limit. The empirical approach is one such method which is fast and can approximate the fluence in heterogeneous tissues. By generating fluence in a 3D voxelated format, it can be easily integrated with multiple imaging modalities. More study is however necessary to understand the errors induced by the Empirical algorithm at large depths as seen in the pencil beam and broad beam fluence profiles. These errors seen can be large at depths greater than 2cm in heterogeneous phantoms. Hence the empirical approach, at this time, cannot be used for absolute quantification of photon fluence. It can however give a good approximation of the relative fluence distribution in tissues with respect to the input photon fluence. The errors in quantification can be reduced by further research into optimization methods to match the Monte Carlo. The training methodology used to derive the weights could be improved to account for the differences in the fluence profiles. Iterative routines and algorithms with merit functions can significantly enhance the accuracy of the Empirical approach.

4.2 Conclusion

The ability of the Empirical approach to approximately emulate the fluence distribution of the Monte Carlo has been studied in homogeneous and heterogeneous media. Even though the empirical algorithm cannot be used for absolute quantification, it can be used in optical therapy to evaluate the merits of different angles of illuminations and source positions which is a prerequisite for determining the placement of an optical source. The 3D GPU based Monte Carlo can then be used for absolute quantification and validation of photon energy distribution. The acceleration provided by the Empirical algorithm can be used to reduce the iterations of the Monte Carlo by identifying only a few possible illumination possibilities. Thus the Empirical algorithm has the potential to be used as a fast preliminary tool to devise optical therapies by estimating relative fluence distribution in tissues prior to validation and correction by using Monte Carlo.

REFERENCES

- [1] Mi-Ran Choi, Rizia Bardhan, Katie J. Stanton-Maxey, Sunil Badve, Harikrishna Nakshatri, Keith Stantz, Ning Cao, Naomi J. Halas, Susan E. Clare, "Delivery of nanoparticles to brain metastases of breast cancer using a cellular Trojan horse," *Cancer Nano*, 3, 47-54 (2012).
- [2] Choi MR, Stanton-Maxey KJ, Stanley JK, Levin CS, Bardhan R, Akin D, Badve S, Sturgis J, Robinson JP, Bashir R, Halas NJ, Clare SE, "A cellular Trojan Horse for delivery of therapeutic nanoparticles into tumors," *Nano Lett* 7(12), 3759–3765 (2007).

- [3] Bardhan R, Chen WX, Perez-Torres C, Bartels M, Huschka RM, Zhao LL, Morosan E, Pautler RG, Joshi A, Halas NJ, "Nanoshells with targeted simultaneous enhancement of magnetic and optical imaging and photothermal therapeutic response," *Adv Funct Mater* 19(24), 3901–3909 (2009).
- [4] Bardhan, R.; Chen, W.; Bartels, M.; Perez-Torres, C.; Botero, M. F.; McAninch, R. W.; Contreras, A.; Schiff, R.; Pautler, R. G.; Halas, N. J.; et al., "Tracking of Multimodal Therapeutic Nanocomplexes Targeting Breast Cancer In Vivo," *Nano Lett*, 10, 4920–4928 (2010).
- [5] Akshay Prabhu Verleker, Qianqian Fang, Mi-Ran Choi, Susan Clare and Keith M. Stantz, "An Optical Therapeutic Protocol to treat brain metastasis by mapping NIR activated drug release: A Pilot Study," *IEEE NSS&MIC Conf. Rec.*, M19-96 (2014), submitted for publication.**
- [6] Q. Fang and D. A. Boas, "Monte Carlo simulation of photon migration in 3D turbid media accelerated by graphics processing units," in *Opt. Express*, vol. 17, pp. 20178–20190 (2009).
- [7] N. Ren, J. Liang, X. Qu, J. Li, B. Lu, and J. Tian, "GPU-based Monte Carlo simulation for light propagation in complex heterogeneous tissues," in *Opt. Express*, vol. 18, pp. 6811–6823 (2010).
- [8] L. Wang, S. L. Jacques, and L. Zheng, "Monte Carlo modeling of light transport in multilayered tissues," in *Computer Methods and Programs in Biomedicine*, vol. 47, pp. 131–146 (1995).
- [9] D. A. Boas, J. P. Culver, J. J. Stott, and A. K. Dunn, "Three dimensional Monte Carlo code for photon migration through complex heterogeneous media including the adult human head," in *Opt. Express*, vol. 10, pp. 159–170 (2002).
- [10] Flock, S.T.; Patterson, M.S.; Wilson, B.C.; Wyman, D.R., "Monte Carlo modeling of light propagation in highly scattering tissues. I. Model predictions and comparison with diffusion theory," *Biomedical Engineering, IEEE Transactions on* vol.36, no.12, pp.1162,1168 (1989).
- [11] Beer, "Determination of the absorption of red light in colored liquids," *Annalen der Physik und Chemie*, vol. 86, 78–88 (1852).
- [12] Van der Zee, Pieter, Matthias Essenpreis, and David T. Delpy. "Optical properties of brain tissue." *OE/LASE'93: Optics, Electro-Optics, & Laser Applications in Science & Engineering*. International Society for Optics and Photonics, 1993.
- [13] M. Firbank, M. Hiraoka, M. Essenpreis, D.T. Delpy, "Measurement of the optical properties of the skull in the wavelength range 650–950 nm," *Phys. Med. Biol.*, 38, 503–510 (1993).
- [14] Cheong, Wai-Fung, Scott A. Prahl, and Ashley J. Welch. "A review of the optical properties of biological tissues." *IEEE journal of quantum electronics*, 26.12, 2166–2185 (1990).
- [15] W. M. Star, "Comparing the P3-approximation with diffusion theory and with Monte Carlo calculations of light propagation in a slab geometry," in *SPIE Proceedings on Dosimetry of Laser Radiation in Medicine and Biology*, vol. IS5, pp. 146–154 (1989).
- [16] G. Yoon, S. A. Prahl and A. J. Welch, "Accuracies of the Diffusion Approximation and its Similarity Relations for Laser Irradiated Biological Media," in *Applied Optics*, vol. 28, pp. 2250–2255 (1989).
- [17] M. J. C. Gemert, A. J. Welch, W. M. Star, M. Motamedi, and W. F. Cheong, "Tissue optics for a slab geometry in the diffusion approximation," in *Lasers Med. Sci.*, vol. 2, pp. 295–302 (1987).
- [18] H. C. van de Hulst, "Multiple Light Scattering: Tables, Formulas, and Applications," Academic, New York, Vols. 1, 2 (1980).
- [19] R. A. J. Groenhuis, H. A. Ferwerda, and J. J. T. Bosch, "Scattering and Absorption of Turbid Materials Determined from Reflection Measurements," *Appl. Opt.* 22, 2456–2467 (1983).
- [20] S. L. Jacques and S. A. Prahl, "Modeling Optical and Thermal Distribution in Tissue During Laser Irradiation," *Lasers Surg. Med.* 6, 494–503 (1987).
- [21] J. M. Steinke and A. P. Shepherd, "Diffusion Model of the Optical Absorbance of Whole Blood," *J. Opt. Soc. Am. A* 5, 813–822 (1988).
- [22] W. M. Star and J. P. A. Marijnissen, "Calculating the Response of Isotropic Light Dosimetry Probes as a Function of the Tissue Refractive Index," *Appl. Opt.* 28, 2288–2291 (1989).

An Optical Therapeutic Protocol to treat brain metastasis by mapping NIR activated drug release: A Pilot Study

Akshay Prabhu Verleker, Qianqian Fang, Mi-Ran Choi, Susan Clare and Keith M. Stantz

Abstract—Treatment of Central Nervous System (CNS) metastasis poses a critical clinical challenge due to limitations in drug uptake across the blood brain barrier and blood-cerebrospinal fluid barrier. Recent research has shown the efficacy of using macrophages as drug carriers to target metastatic sites in the brain, which can then be activated by illuminating with near infrared radiation. The goal of this research is to develop an optically targeted therapeutic treatment of metastasis, specifically for metastatic breast cancer of the brain. As a first step towards accomplishing this, we developed a 3D Monte Carlo photon transport code capable of simulating phantoms with optical properties of brain and tumor; and validated the Monte Carlo simulated photon fluence within brain phantoms using an optical dosimetry probe. The phantom studies showed good correlation (correlation coefficient $R=0.977$) between the probe measurements and the Monte Carlo simulation in a white matter phantom (reduced scattering coefficient $\mu_s=8.25\text{mm}^{-1}$, absorption coefficient $\mu_a=0.005\text{mm}^{-1}$). Our future steps will be to implement the Monte Carlo to map out photon energy distribution in the brain, and subsequent drug release, by segmenting & translating head CT image volumes to corresponding optical properties of brain tissues. To access the therapeutic response, changes in the vascular physiology of the brain due to Her2 inhibition will be measured using dynamic contrast-enhanced imaging (e.g. DCE-CT), and with Monte Carlo based optical fluence maps. An optical treatment plan, using fast Monte Carlo software, optimized with CT segmented image volumes, would significantly reduce the treatment time and allow targeted drug activation while sparing healthy tissues.

I. INTRODUCTION

TREATMENT of Central Nervous System (CNS) metastasis poses a critical clinical challenge due to limitations in drug uptake in the brain (across the blood brain barrier and blood-cerebrospinal fluid barrier) and adverse neurotoxic effects of mainstay therapies such as whole brain radiation therapy (WBRT) and stereotactic radiosurgery.¹ With non-CNS metastasis being treated successfully with receptor targeted drug delivery, aided by improved imaging and localized radiotherapy techniques, the brain remains a sanctuary for

metastasis (e.g. triple negative and HER2+ breast cancer metastasis with median survival rates of 2 to 16 months).¹ This study is part of a project which demonstrated a macrophage based “Trojan Horse” delivery of fluorescent molecules into brain metastasis² and subsequent release of the fluorescent molecules on activation *in-vivo* by NIR radiation.³ The larger goal of this collaborative project is to deliver lapatinib-gold nanocomplex laden macrophages to brain metastasis and design a therapeutic protocol to optically stimulate drug release in target tissues in the brain. In the current project, the purpose is to design an optical simulation protocol (using Monte Carlo simulations) to effectively predict the photon distribution and subsequent drug activation in the brain tissue, and validate it by using an optical dosimetry probe. With the rate/quantity of drug release being directly dependent on the optical power delivered, the Monte Carlo simulation protocol, with the ability to predict photon distribution in heterogeneous brain tissue, can be used to generate an equivalent drug release map. The optical properties of the brain can be mapped by converting the CT image densities of the brain into the corresponding optical properties of the tissue (e.g. white/gray matter, CSF, etc.), which would serve as an input to the Monte Carlo routine. The optical drug release map generated by Monte Carlo can be co-registered with CT images to improve the therapeutic efficacy of the protocol.

In order to predict the photon energy distribution in heterogeneous brain tissue, we used a GPU based 3D Monte Carlo simulation code⁴, which was modified to generate user defined beam profiles to emulate the NIR (800 nm) laser source used in our lab. Monte Carlo simulation has been used as the gold standard for photon propagation studies (in 3D heterogeneous media), with the GPU version having acceleration speeds 100 to 300 times faster than corresponding CPU versions.⁴ In order to validate and quantify the Monte Carlo generated fluence in brain tissue phantoms, we used an optical dosimetry probe to measure the photon fluence in low optical fluence regions. An optimized treatment plan using a fast Monte Carlo software to predict *in vivo* drug release, would significantly reduce the treatment time and allow the targeted drug activation while sparing healthy tissues.

In addition to designing the Optical therapeutic protocol, we also looked into the feasibility of using Dynamic Contrast Enhanced CT (DCE-CT) imaging to monitor and quantify the efficacy of treatment. The vascular structure of a tumor is complex and heterogeneous, and is seen to vary between individual tumors and during different phases of tumor growth.⁵ This heterogeneity in tumor vasculature, characterized by hypoxia, anoxia and hypoglycemia, leads to differing response to treatment due to formation of barriers to transport and distribution of drug molecules.⁵⁻⁹ Following

Manuscript received Nov 14, 2014. This work was supported in part by the DoD/BCRP Grant (PI: Dr. Clare; Northwestern University), “Delivery of Nano-Tethered Therapies to Brain Metastases of Primary Breast Cancer Using a Cellular Trojan Horse”.

Akshay Prabhu Verleker is with the School of Health Sciences, Purdue University, West Lafayette, IN 47907 USA (email: aprabhuv@purdue.edu)

Qianqian Fang is with the Martinos Center for Biomedical Imaging, Massachusetts General Hospital, Harvard Medical School, Charleston, MA 02129 USA (email: fangq@nmr.mgh.harvard.edu)

Mi-Ran Choi is with the Feinberg School of Medicine Northwestern University, Chicago, IL 60611 USA (email: mi.choi@northwestern.edu)

Susan Clare is with the Feinberg School of Medicine Northwestern University, Chicago, IL 60611 USA (email: susan.clare@northwestern.edu)

Keith M. Stantz is with the School of Health Sciences, Purdue University, West Lafayette, IN 47907 USA (email: kstantz@purdue.edu)

treatment with anti-angiogenic or cytotoxic drugs, the tumor vasculature undergoes complex physiological and biological changes some of which are adaptive in nature.⁵⁻⁹ DCE-CT has been successfully used to simultaneously quantify physiological parameters such as perfusion and vascular plasma volume in tumors after treatment with therapeutic drugs.¹⁰⁻¹² Past research has proved the feasibility of using DCE-CT in measuring the physiological response of breast tumors to anti-angiogenic therapies using the two-compartmental model.¹¹⁻¹² In the present study we used the above model to obtain parametric maps of perfusion, permeability, fractional plasma volume and fractional interstitial volume in glioma tumors grown in mice; thus demonstrating the feasibility of DCE-CT imaging to monitor brain tumor response to treatment.

II. METHODS

Step 1: The optical dosimetry probe (1.5mm diameter) was calibrated using a calorimeter (Gold standard) in low fluence regions. The probe measurements were used to validate Monte Carlo generated photon fluence in brain phantoms resembling white and gray matter, made with specific concentrations of India ink (absorber) and Intralipid (scatterer),¹³⁻¹⁴ as measured by photo-spectrometer (Gold standard), consistent with brain tissue and tumors (values) as shown in Fig 1. The source of light used was an integrating sphere connected to a pulsed NIR laser with wavelength 800 nm, frequency 200MHz, and energy 10mJ/pulse. The broad beam NIR output power emanating from the integrating sphere was 0.2083mW/mm².

Step 2: In order to apply the Monte Carlo (MC) simulation protocol to the brain, we designed a segmentation software to determine tissue boundaries in the brain using Computed tomography images. The CT image densities in Hounsfield units (HU) of the brain were translated into corresponding optical properties (absorption coefficient, scattering coefficient, and anisotropy factor) using lookup tables (Fig 2). The lookup tables were prepared from earlier studies which derived the Hounsfield units and optical properties of brain tissues such as white/gray matter.¹³⁻¹⁵ The segmentation software generated an optical map of the brain, which was given as input to the Monte Carlo. The photon energy map generated by the Monte Carlo can be co-registered with the CT image to visualize the efficacy of drug release.

Step 3: "Optical treatment protocol", voxel-based optical properties of a human head (obtained from CT scans) were input into MC code to simulate 3D fluence maps from multiple (optically coupled) light sources. This study also looked into the feasibility of monitoring effectiveness of targeted drug release by monitoring the physiology at target sites and surrounding tissues. An Orthotopic model of glioblastoma tumors were grown in mice and parametric images of perfusion, permeability, fractional plasma volume and fractional interstitial volume were derived using the two compartmental model.¹²

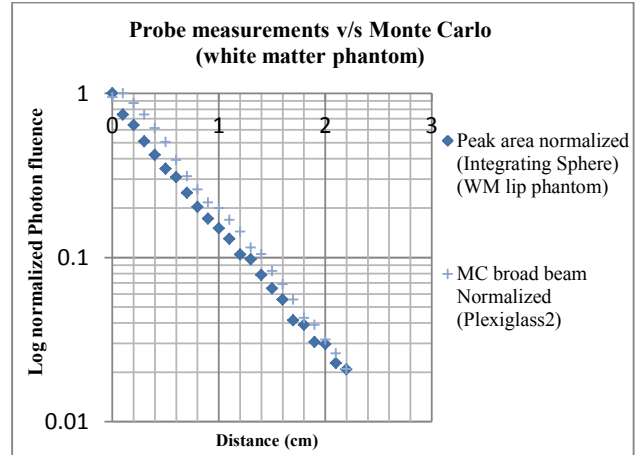


Fig. 1. Validation of Monte Carlo simulated photon fluence (1/mm²) with probe measurements (peak area in mV) in a white matter phantom. Log normalized fluence plotted v/s depth in a white matter phantom. Correlation R=1.

III. OBSERVATIONS & RESULTS

The Monte Carlo generated photon fluence was validated by probe measurements in optical brain phantoms (e.g. white matter in Figure 1). The optical fluence measured by the probe was in turn, calibrated using a calorimeter (Gold standard) and showed a linear and isotropic response to input NIR fluence at different incidence angles (<5% variation). Our MC simulation studies showed that 99% of photons are attenuated by the bone (1cm), which was confirmed by probe measurements in an empty goat skull. The segmentation code (with iterative Monte Carlo) can be used to identify regions of least bone thickness and determine the path of least attenuation to couple maximum power to brain tissues. This study proved that an optimized Monte Carlo could be successfully used to quantify photon propagation in the brain and thus predict the rate of drug release in target tissues to depths up to 5cm in brain tissues.

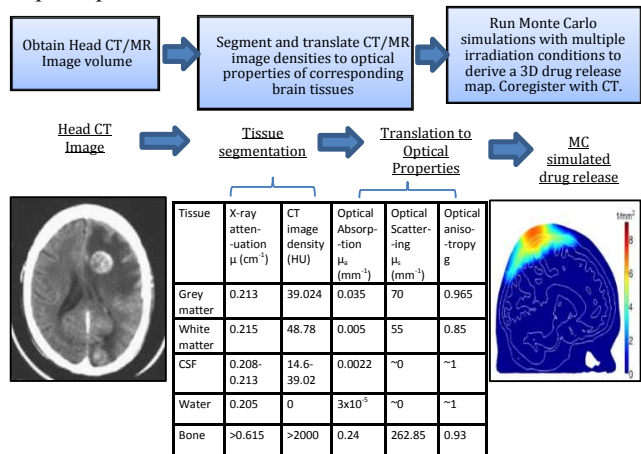


Fig. 2. Monte Carlo based treatment protocol. Head CT image densities (in Hounsfield Units/HU) are segmented and translated into optical properties of the brain tissue (white/gray matter, CSF, skull bone, etc.). Monte Carlo routine is then used to simulate light propagation through the brain. [CT image reference: <http://www.mpoullis.com/thored/rad/23.htm>]¹⁶

Our preliminary longitudinal study has indicated that DCE-CT is an effective tool to study tumor progression and physiology (Fig 3) of glioma tumors. We propose to monitor these effects by studying the change in fractional plasma volume and fractional interstitial volume, both of which are excellent indicators of vascular physiology (Fig 3).

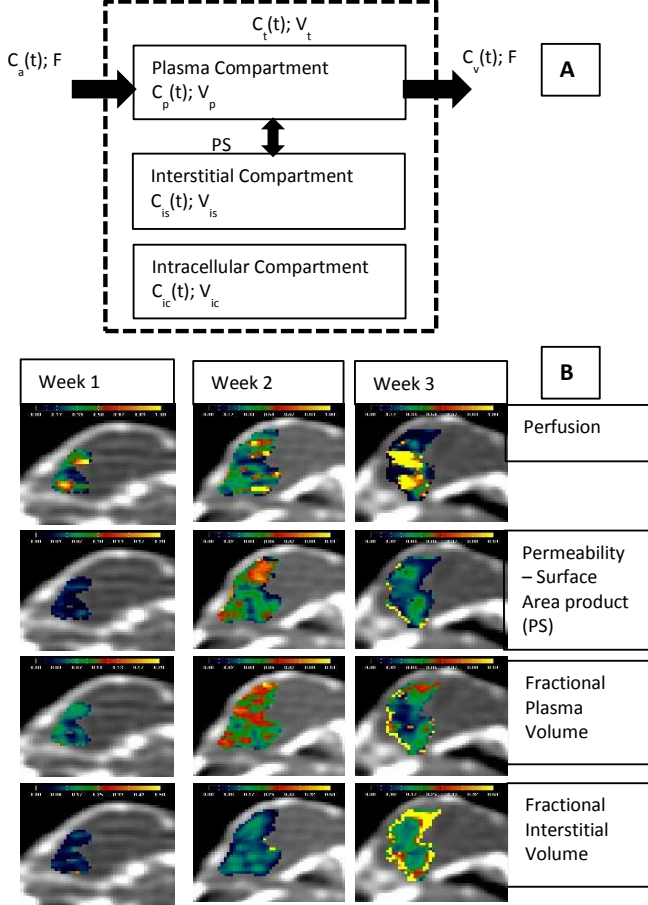


Fig. 3. Monitoring cancer therapy through Dynamic Contrast Enhanced CT (DCE-CT). (A) Schematic of two compartmental model.¹² (B) Parametric images of glioblastoma (orthotopic model) grown in mice. In this longitudinal study, parametric images were obtained of perfusion, permeability, fractional plasma volume and fractional interstitial volume of glioma tumors grown in mice using the two compartmental model. These parameters can be used to quantify the efficacy of treatment, thus proving effectiveness of using DCE-CT to monitor targeted drug therapy.

IV. DISCUSSION

In this study, we have assumed that the quantity of drug release is proportional to the optical power coupled to the tissues (as shown in previous *in-vitro* studies). Future studies will focus on quantifying the optical drug release threshold by determining the relationship between optical power coupled and amount of drug released. Further studies will involve adjusting beam profiles to optimize the coupling and localization of optical energy in the brain for maximal drug release. In order to monitor tumor response to therapy, DCE-CT will be used to further study vascular normalization¹⁷ in tumors caused by anti-angiogenic effects of lapatinib drug, which can help in optimizing therapeutic efficacy.

V. CONCLUSION

This study has successfully demonstrated the potential of using a fast voxel based Monte Carlo based routine to predict the rate of drug release in heterogeneous brain tissue by using Computed Tomography images to segment and translate tissue boundaries of the brain. An optimized therapeutic protocol with a fast Monte Carlo routine can be used to determine the best irradiation conditions for targeted drug release in brain tissue within clinically relevant time frames.

VI. ACKNOWLEDGEMENT

We would like to thank Justin Sick and Fahed Alsanea for their contribution in developing experimental setups and Michael Shaffer for his work in developing the optical dosimetry probe. We are grateful to our collaborators Naomi Halas, Amanda Goodman and Sandra Bishnoi for their contributions in developing the drug nanocomplexes for optically activated drug release.

REFERENCES

- [1] A Niwinska, et al., "Breast cancer brain metastases: differences in survival depending on biological subtype", *Ann Oncol*, 2010, 21: 942–948.
- [2] Mi-Ran Choi, et al., "Delivery of nanoparticles to brain metastases of breast cancer using a cellular Trojan horse", *Cancer Nano*, 2012; 3: 47–54.
- [3] Mi-Ran Choi, et al., "A cellular Trojan Horse for delivery of therapeutic nanoparticles into tumors", *Nano Lett*, 2007; 7(12):3759–3765.
- [4] Q. Fang, et al., "Monte Carlo simulation of photon migration in 3D turbid media accelerated by graphics processing units", *Opt. Express* 2009; vol. 17.
- [5] P. W. Vaupel, "The influence of tumor blood flow and microenvironmental factors on the efficacy of radiation, drugs and localized hyperthermia", *Klin Padiatr.*, vol. 209, 1997, 243–249.
- [6] K. D. Miller, "Issues and challenges for antiangiogenic therapies," *Breast Cancer Res. Treat.*, vol. 75, no. Suppl 1, 2002, S45–S50.
- [7] B. S. Kuszky, F. M. Corl, F. N. Franano, D. A. Bluemke, L. V. Hofmann, B. J. Fortman, and E. K. Fishman, "Tumor transport physiology: Implications for imaging and imaging-guided therapy," *AJR Am. J. Roentgenol.*, vol. 177, 2001, 747–753.
- [8] Bergers G, Hanahan D, "Models of resistance to anti-angiogenic therapy." *Nat Rev*, 2008, 8:1592Y1603.
- [9] Grepin R, Pages G, "Molecular mechanisms of resistance to tumor anti-angiogenic strategies," *J Oncol*, 2010, 1835680.
- [10] Kan Z, Phongkitkarun S, Kobayashi S, Tang Y, Ellis LM, Lee TY "Functional CT for quantifying tumor perfusion in antiangiogenic therapy in a rat model," *Radiology*, 2005, 237:1151Y1158.
- [11] Stantz, Keith M., et al. "Monitoring the longitudinal intra-tumor physiological impulse response to VEGFR2 blockade in breast tumors using DCE-CT." *Molecular Imaging and Biology*, vol. 13(6), 2011, 1183–1195.
- [12] Cao, Minsong, et al. "Developing DCE-CT to quantify intra-tumor heterogeneity in breast tumors with differing angiogenic phenotype." *Medical Imaging, IEEE Transactions on*, vol. 28(6), 2009, 861–871.
- [13] Van der Zee et al., "Optical properties of brain tissues", *OE/LASE'93: Optics, Electro-Optics, and Laser Applications in Science and Engineering*, International Society for Optics and Photonics, 1993.
- [14] Wai-Funf Cheong et al., "A review of the Optical Properties of Biological Tissues", *IEEE journal of quantum electronics*, 1990, 2166–2185.
- [15] Arimitsu Tetsuo et al., "White-Gray Matter Differentiation in Computed Tomography", *Jou rnal of Computer Assisted Tomography*, 1977, 437
- [16] Mike Poullis, "Lung Cancer, Staging," [online], <http://www.mpoullis.com/thorcd/rad/23.htm> (Accessed: 3 November 2014).
- [17] Jain, Rakesh K. "Normalization of tumor vasculature: an emerging concept in antiangiogenic therapy," *Science*, 2005, 307.5706, 58–62.

Optical dosimetry probes to validate Monte Carlo and empirical-method-based NIR dose planning in the brain

AKSHAY PRABHU VERLEKER,¹ MICHAEL SHAFFER,¹ QIANQIAN FANG,² MI-RAN CHOI,³
SUSAN CLARE,³ AND KEITH M. STANTZ^{1,*}

¹School of Health Sciences, Purdue University, 550 Stadium Mall Drive, West Lafayette, Indiana 47907, USA

²Department of Bioengineering, Northeastern University, 360 Huntington Avenue, Boston, Massachusetts 02115, USA

³Department of Surgery, Feinberg School of Medicine, Northwestern University, 303 East Superior Street, Chicago, Illinois 60611, USA

*Corresponding author: kstantz@purdue.edu

Received 18 July 2016; revised 4 October 2016; accepted 5 October 2016; posted 11 October 2016 (Doc. ID 270741); published 1 December 2016

A three-dimensional photon dosimetry in tissues is critical in designing optical therapeutic protocols to trigger light-activated drug release. The objective of this study is to investigate the feasibility of a Monte Carlo-based optical therapy planning software by developing dosimetry tools to characterize and cross-validate the local photon fluence in brain tissue, as part of a long-term strategy to quantify the effects of photoactivated drug release in brain tumors. An existing GPU-based 3D Monte Carlo (MC) code was modified to simulate near-infrared photon transport with differing laser beam profiles within phantoms of skull bone (B), white matter (WM), and gray matter (GM). A novel titanium-based optical dosimetry probe with isotropic acceptance was used to validate the local photon fluence, and an empirical model of photon transport was developed to significantly decrease execution time for clinical application. Comparisons between the MC and the dosimetry probe measurements were on an average 11.27%, 13.25%, and 11.81% along the illumination beam axis, and 9.4%, 12.06%, 8.91% perpendicular to the beam axis for WM, GM, and B phantoms, respectively. For a heterogeneous head phantom, the measured % errors were 17.71% and 18.04% along and perpendicular to beam axis. The empirical algorithm was validated by probe measurements and matched the MC results ($R^2 > 0.99$), with average % error of 10.1%, 45.2%, and 22.1% relative to probe measurements, and 22.6%, 35.8%, and 21.9% relative to the MC, for WM, GM, and B phantoms, respectively. The simulation time for the empirical model was 6 s versus 8 h for the GPU-based Monte Carlo for a head phantom simulation. These tools provide the capability to develop and optimize treatment plans for optimal release of pharmaceuticals in the treatment of cancer. Future work will test and validate these novel delivery and release mechanisms *in vivo*. © 2016 Optical Society of America

OCIS codes: (170.0170) Medical optics and biotechnology; (170.3660) Light propagation in tissues; (170.3890) Medical optics instrumentation; (260.3060) Infrared; (040.0040) Detectors.

<https://doi.org/10.1364/AO.55.009875>

1. INTRODUCTION

Optical therapy is a non-invasive technique that can be utilized to treat cancer through photodynamic therapy (PDT) techniques [1] and the triggered release of drugs from nano-complexes in metastatic tissues [2,3]. Near-infrared (NIR) light is preferred for deep tissue activation due to its low optical attenuation and thus high penetration. This study is part of a project which seeks to develop optically activated drug release in order to implement macrophage-based “Trojan horse” drug delivery to brain metastasis [2,3]. Given that the rate of release and quantity of the released drug are likely to be affected by the optical power delivered [2,3], the development of optical

simulation and dosimetry tools that can accurately determine the photon fluence in the brain and ultimately be integrated into a clinical environment is critical. In our study a GPU-based 3D Monte Carlo (MC) code is used to simulate the photon energy deposition in the brain [4–10], and an optical dosimetry probe was fabricated to validate the photon fluence in heterogeneous media consistent with the skull and brain. While the primary application is in the field of controlled drug release, these tools can also be applied to a wide range of applications, including NIR-based imaging techniques, such as photoacoustic tomography[11] and near-infrared spectroscopy [12], and in infrared neural stimulation [13] of the cochlea and neuroprosthesis.

Monte Carlo simulation methods have been used as the gold standard for photon propagation studies in heterogeneous media [4–8]. Traditional CPU-based Monte Carlo models suffer from slow computation speeds, which makes them non-viable for clinical applications, which require the simulation of a large number of photons (excess of 10^7) especially in highly attenuating (scattering) brain tissues, such as the skull and white matter. The GPU-based 3D Monte Carlo used in this study, developed by the Fang group [9], can achieve complete brain simulation of a high-fluence broad-beam source within hours compared to days for CPU-based models ($300\times$ faster) [9]. This new model features a voxel-based 3D fluence and energy distribution with significant improvements, such as efficient parallel random number generators, reflection at 3D boundaries, time-resolved simulations, fluence normalizations, and ease of integration with anatomical imaging modalities (e.g., CT, MR, ultrasound, etc.), thus improving its clinical viability and efficacy for diagnosis and therapy. To date, this code has not been validated through 3D measurements under various illumination conditions.

Application of a 3D Monte Carlo as an optical therapy planning tool in clinical practice requires rigorous validation of its physics-based model, so as to reduce the uncertainty in light dose delivery and improve diagnostic accuracy. Past studies have validated the Monte Carlo using diffusion approximation simulations in slab geometry and under limited heterogeneity conditions [8,9]. Only a few studies have attempted to rigorously validate the 3D MC fluence using dosimetry measurements in phantoms under varying illuminations with finite beam width and heterogeneity conditions [14,15]. The varying degree of accuracy can be attributed to differences in estimation of optical properties of the medium, illumination and object boundary conditions, and the ability of the Monte Carlo to accurately estimate photon distribution in complex heterogeneous boundary conditions. All of these differences need to be analyzed and optimized in order to get maximum efficiency from the Monte Carlo simulations. The use of optical dosimetry for pre-clinical validation, along with the ability to verify optical properties of phantoms used in the measurements, is essential in order to ensure therapeutic accuracy of the Monte Carlo. Additionally, any mismatch in simulation and actual measurement conditions can be addressed by this exercise to improve therapeutic confidence in the tool.

To validate the MC, the localized photon distribution in tissues was measured using a novel titanium dioxide-based optical dosimetry probe (ODP). ODPs have been extensively used in PDT to measure photon fluence as well as to deliver light locally to tissues [1,16–21]. The small size of the dosimetry probe (1.5 mm diameter) and near-isotropic response at NIR wavelength (800 nm) improves the accuracy of localized light measurement in highly scattering tissues/phantoms, compared to other dosimetry probes. It is also advantageous over standard photon measurement devices, such as calorimeters, which only measure fluence in air. In this study, the novel titanium-based probe was designed and evaluated against a standard nylon-based probe [17,20] and their linear and isotropic response analyzed. Its linear response in air was

calibrated using a calorimeter (gold standard) for absolute fluence quantification.

Translating an optical therapy planning tool into the clinic requires that simulations be performed in feasible time frames. While the GPU-based Monte Carlo takes a few hours for a complete head simulation under a single illumination condition, optimizing a treatment plan would require iterations with multiple laser sources. While a cluster of GPUs could be used to solve this problem, thereby significantly increasing costs, it prompted us to design an empirical model of photon propagation [22] to approximate 3D photon fluence in tissue-like media at a fraction of time taken by the GPU-based Monte Carlo. This model assumes the photon fluence in a voxel is the weighted sum of the fluences in the neighboring voxels in the preceding layer [22], where the weights are determined using the Monte Carlo for typical brain tissues, such as gray matter, white matter, skull bone, and astrocytoma. Previous studies have used approximate methods, such as the diffusion approximation (DE) [23,24], hybrid (MC + DE) [25], radiative transport equation [26,27], and the adding-doubling method [28], to approximate 3D photon distribution. The empirical method (EM) is an addition to the existing list of methods and mainly differs in the means by which photon scatter is calculated and has a similar speed as the diffusion approximation [29] (in seconds). While other methods rely on physics-based models based on approximations to the radiative transport equation, the empirical approach is designed to be calibrated against the Monte Carlo in a homogeneous medium for a fixed set of optical properties, before being applied in a complex medium under different illumination conditions. Hence a calibration step with a fixed set of optical properties is necessary before applying this model. It is important to note that once calibrated, this model does not require additional calibrations, which allows for its repetitive use for standard clinical applications with a fixed set of optical properties (e.g., head simulation) under differing anatomical geometries and illumination conditions. The significant improvement in the speed and reasonable accuracy inspired us to integrate it into the optical therapy planning tool along with the Monte Carlo and the titanium-based optical dosimetry probe.

In this paper, a titanium-based optical dosimetry probe was fabricated and calibrated to provide localized energy fluence measurements, and used to validate the 3D GPU-based Monte Carlo code under differing beam profiles and heterogeneous tissue phantoms. To provide an accelerated, *real-time* solution to photon transport, an empirical model was proposed and evaluated against MC simulated in tissue phantoms. Finally, the role of these new and/or improved tools in optically stimulated drug release will be discussed.

2. MATERIALS AND METHODS

A. Optical Brain Phantoms

Brain phantoms were designed to mimic the optical absorption and reduced scattering coefficients of white matter, gray matter, and skull bone (at 800 nm) [29–31] using India ink (absorber) and intralipid (scatterer) [32–35] in water ($\mu_a = 0.020\text{ cm}^{-1}$) [36]. The absorption coefficient of India ink (Higgins non-water-proof black ink) and the scattering

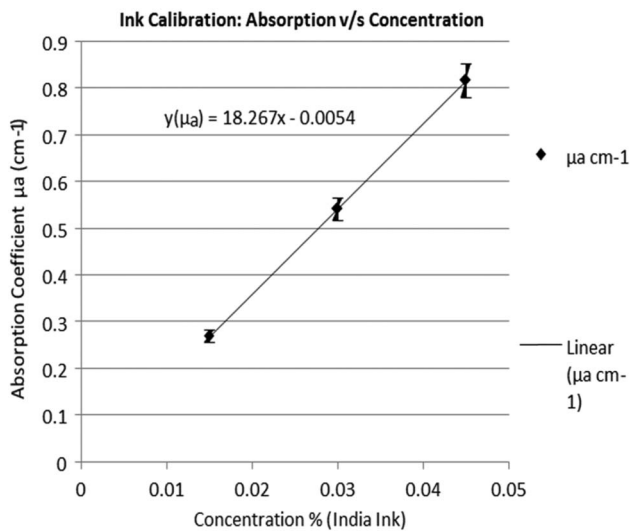


Fig. 1. Calibration curve of spectrophotometer measured absorbance versus % concentration of India ink. The error bars represent minimum and maximum absorbance.

coefficient of intralipid (Intralipid 20% from Fresenius Kabi), at 800 nm wavelength, were determined and validated using a spectrophotometer (Shimadzu UVmini 1240 Spectrophotometer), which served as the gold standard for absorbance. The scattering properties of intralipid were determined using the spectrophotometer for low concentrations (0.003%–0.012%), where $\mu_s = 9.52 \text{ cm}^{-1}\% \text{concentration}^{-1}$, compared to $9.95 \text{ cm}^{-1}\% \text{concentration}^{-1}$ as shown in previous studies by Van Staveren [33], which is within the 4.32% relative error. Figures 1 and 2 show the calibration curves of absorbance (or attenuation) versus concentration of India ink and intralipid obtained using the spectrophotometer. The linear relationship between concentration and absorbance was used to design optical phantoms with specific absorption and scattering properties of white matter, gray matter, and skull bone [29,30]. These optical properties (absorption and scattering coefficients and anisotropy factor) are shown in Table 1 and were used to design the optical brain phantoms (Table 2) using the equations derived from Figs. 1 and 2.

The linear relationship of concentration versus total attenuation is particularly useful in determining intralipid concentrations for high scattering tissues in the brain. Both homogeneous as well as heterogeneous phantoms were made using various concentrations of India ink and intralipid. The phantom composition for the homogeneous phantom was a solution of India ink and intralipid in water, while the heterogeneous phantoms were comprised of layers of 1% agar (Fisher Scientific Laboratory Grade Agar A3600-500) doped with India ink and intralipid to represent skull bone and gray matter, with a layer of white matter in aqueous solution. The scattering properties of agar and the absorption properties of India ink were also measured using the spectrophotometer for each individual sample used in the study while the scattering properties of intralipid were derived from the linear relationship in Fig. 2.

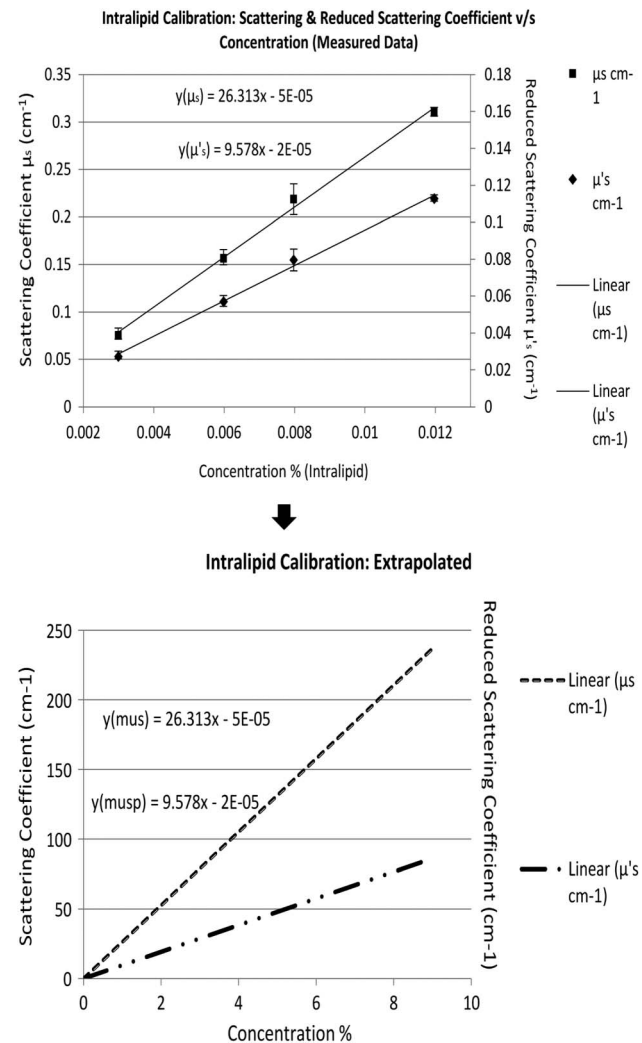


Fig. 2. Intralipid scattering: upper figure represents measured values of scattering coefficients (μ_s and μ'_s) versus % concentration of intralipid using a spectrophotometer. The error bars represent minimum and maximum values. Lower figure shows extrapolated values from the linear relationship derived from the measured values (with relative and statistical uncertainties of 4.32% and 1.8%, respectively).

B. Optical Dosimetry Probe Design and Calibration

The optical dosimetry probe consists of a spherical bulb of highly scattering material attached to an optical fiber [1,16,17,19]. The construction and fluence measurement by

Table 1. Optical Properties of Brain Tissues [29,30]

Tissue Type	Absorption Coefficient μ_a (cm ⁻¹)	Scattering Coefficient μ_s (cm ⁻¹)	Anisotropy Factor g	Reduced Scattering Coefficient μ'_s (cm ⁻¹)
White matter	0.05	550	0.85	82.5
Gray matter	0.35	700	0.965	24.5
Skull bone	0.24	184	0.9	18.4

Table 2. Phantom Composition for MC Versus Probe Comparison

Phantom Type	Tissue Type	Intralipid %	Ink %	Absorption Coefficient μ_a (cm ⁻¹)	Reduced Scattering Coefficient μ'_s (cm ⁻¹)
Liquid phantom ^{ab}	White matter	7.5	0	0.002	71.84
Liquid phantom ^a	Gray matter	2.36	0.023	0.379	22.64
Liquid phantom ^a	Skull bone	1.82	0.0156	0.26	17.44
Solid phantom ^b	Gray matter	2.56	0.0195	0.35	24.5
Solid phantom ^b	Skull bone	1.92	0.0134	0.25	18.399

^aPhantom composition used in homogeneous phantom studies.

^bPhantom composition used in heterogeneous (layered) phantom studies.

Notes: The anisotropy factor of intralipid ($g = 0.636$) was used for the phantoms.

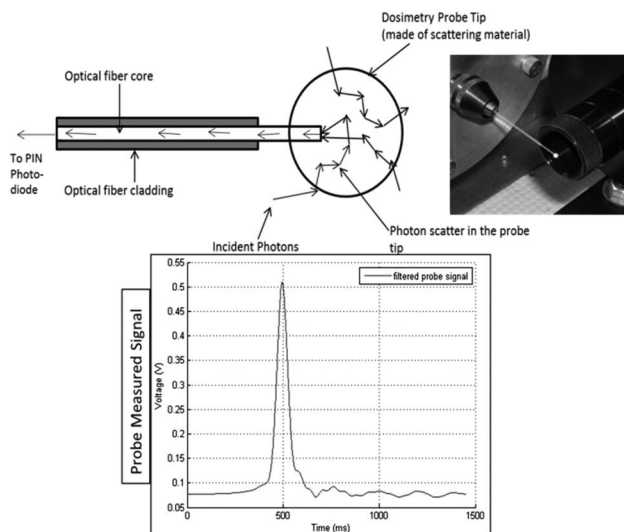
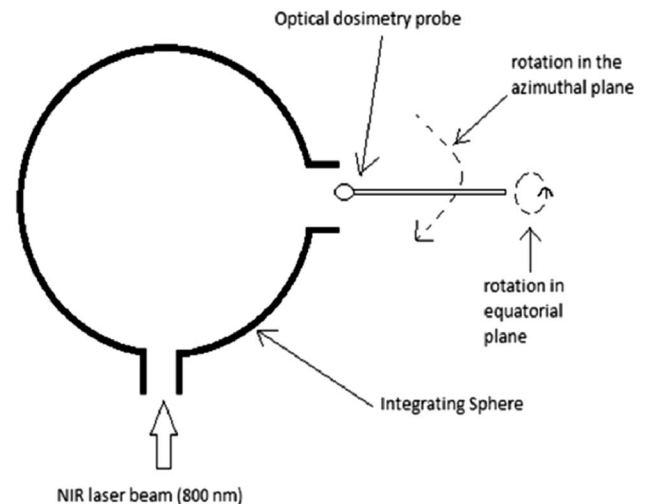
the probe are shown in Fig. 3. The optical fiber is connected to a PIN photodiode circuit (ET-2030, Electro Optics Technology Inc.) whose output voltage is read using an oscilloscope (Tektronix TDS3052B Digital Oscilloscope). Two models of optical dosimetry probes with tips made of nylon and titanium dioxide were designed [37]. The performance of the traditionally used nylon-based probes [19] was compared to that of the titanium dioxide-based probes by measuring the response to different angles of incidence in the equatorial and azimuthal planes, e.g., isotropicity response function.

The nylon spheres have been widely used for photodynamic therapy and were made of nylon due to their isotropic response [19]. These were used as the standard of reference to compare the performance of the novel titanium-based probes. The titanium-based probes have the scattering tips made of a mixture titanium dioxide (Du Pont Ti-Pure R-900) and a clear two-part epoxy (Tra-Con BA-F114) mixed in a ratio of 9.1 mg TiO₂ to 1 ml of the epoxy (mixed) [37,38]. The use of epoxy as a medium for TiO₂ is ideal as it is transparent to NIR light and ensures that light scatter in the probe tip is entirely due to TiO₂ particles. The titanium probes were selected since the particle size of titanium dioxide is around 410 nm, which results in optimal scattering at 820 nm or when the wavelength is approximately twice the particle size. Since the wavelength used in our studies is 800 nm, the titanium probes have been

designed to show a higher sensitivity than the nylon probes. The titanium-based probe tips were molded within a specially designed caste and a fiber optic cable (BFL48-400, 4 mm diameter, 0.48 numerical aperture) was inserted within the cured spheres at a depth of approximately 1/3 of the sphere's radius [37]. The nylon-based probes were approximately 3.175 mm in diameter and were machined in a multistage process [37]. The other end of the fiber optic cable was connected to a PIN photodiode (ET-2030, Electro Optics Technology Inc.) through a SMA-905 connector and the voltage output was read using an oscilloscope (Tektronix TDS3052B).

Figures 4 and 5 show the setup used to test the isotropicity of the dosimetry probes in the equatorial and azimuthal planes. The probe tip is illuminated by laser light emanating from an integrating sphere (Melles Griot two-port integrating sphere), which produces a uniform broad beam of diffuse light, which is used to characterize the probe response. The probe was rotated with angular increments of 15° in the equatorial and 10° in the azimuthal planes, and its response on the oscilloscope was measured.

The center of the probe tip was maintained at the center of rotation during the entire procedure. The isotropicity of the probe, measured by calculating its coefficient of variation, defined as the ratio of standard deviation to the mean of the rms value over all the angles, is shown in Fig. 6(a). The range of

**Fig. 3.** Design and working of the optical dosimetry probe.**Fig. 4.** Setup for calibration of the optical dosimetry probe: measuring isotropicity (in equatorial and azimuthal planes) of the probe.

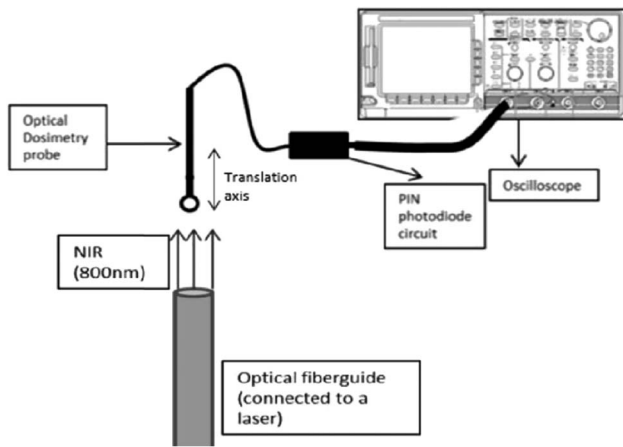


Fig. 5. Setup for calibration of the optical dosimetry probe: measuring the linearity of the probe to incident laser fluence.

angles was 0 to 360 deg for equatorial measurements and 0 to 150 deg for azimuthal measurements. The angular span for azimuthal measurements was limited due to physical limitations of the experimental setup. The individual rms voltage measured by the probe was normalized to the power measured using a calorimeter.

In the test of linearity (Fig. 5), the dosimetry probe response is validated using a calorimeter (Ophir CE, Nova 2 Ophir: 3A-P-SH-VI, aperture 12 mm) by illuminating with a pulsed laser beam of wavelength 800 nm, frequency 10 Hz, output fluence 17.64 mW/cm^2 . The probe and the calorimeter are translated along the beam axis (in air) and the photon fluence is measured at different positions. The linearity of response of the 1.5 mm titanium probe (selected due to its isotropicity) is shown in Fig. 6(b). The linearity of the probe measurement (Φ_{probe} , mV/mm^2) with respect to the calorimeter measurement ($\Phi_{\text{calorimeter}}$, mW/mm^2) was derived as follows by fitting a line on the measured data:

$$\phi_{\text{calorimeter}} = \frac{\phi_{\text{probe}} + 1.7296}{590.46}. \quad (1)$$

The probe voltage signal was filtered using a bandpass Butterworth filter to remove high-frequency noise in the probe response. The photon fluence is proportional to integral of the probe voltage output over the time of the laser pulse and was calculated by summing over the measured voltages over the pulse duration (Fig. 3). This is a novel technique used in this study and was found to be a much better representation of the probe output as compared to measuring the absolute voltage.

The probe voltage and calorimeter power were normalized to the respective surface areas [probe diameter = 1.5 mm, probe surface area (sphere) = 7.065 mm^2 , calorimeter aperture = 12 mm, calorimeter surface area (circle) = 113.04 mm^2].

C. Absolute Photon Quantification in Tissue-Like Media

The linear relationship in Eq. (1) was modified to derive the optical fluence in liquid brain phantoms. The light entering the fiber within the probe depends on the amount of multiple

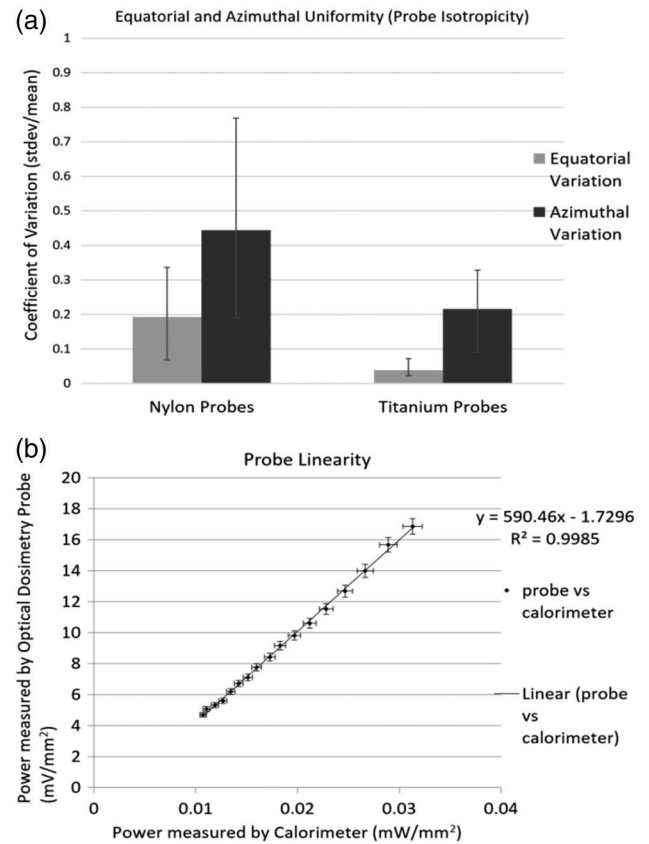


Fig. 6. (a) Probe isotropicity of titanium versus nylon probes. The coefficient of variation (stddev/mean rms voltage) was calculated for probes made of nylon and titanium. The error bars show minimum and maximum variation in individual probe response. The TiO_2 -based probes showed more isotropicity in equatorial and azimuthal directions. (b) Probe linearity: graph of total voltage (area under pulse) (mV/mm^2) measured by a 1.5 mm diameter TiO_2 probe versus the power measured by a calorimeter per unit surface area (mW/mm^2). The probe response is linear over a dynamic range of 0.01074 mW/mm^2 to 0.031316 mW/mm^2 as measured by the calorimeter. The error bars show a 3% variation (systematic error) in pulsed laser power fluctuation.

photon scattering within the spherical probe tip, which in turn depends on the ratio of the refractive index of the probe with respect to the medium [19]. The refractive index of the titanium probe tip should lie close to that of the epoxy ($n = 1.53$) [39] since the concentration of titanium ($n = 2.73$) [38] is low ($<20 \text{ mg/mL}$). Since the refractive index of air is less than that of water, the probe response in water is smaller as more light leaves the probe in water compared to air. To account for the difference in the reflectance between probe–air and probe–water interfaces a calibration factor was measured. The probe was placed inside a cuvette, 0.2 cm from the surface. First the probe response voltage was measured in air (ϕ_{air}) and then measured again by filling the cuvette with water (ϕ_{water}), without changing the position of the probe with respect to the cuvette and the laser source. By accounting for the attenuation by water ($\mu_{\text{water}} = 0.020 \text{ cm}^{-1}$; 0.2 cm path length) and the difference in the beam spread (change in refractive index for cuvette-to-air versus cuvette-to-water), the

calibration factor (CF) was determined experimentally to be 1.32, using the following equation:

$$CF = \frac{\phi_{\text{air}}(e^{-\mu_{\text{water}}L}) \left(\frac{FWHM_{\text{air}}}{FWHM_{\text{water}}} \right)}{\phi_{\text{water}}} \quad (2)$$

The FWHM values were measured for both these setups using the probe ($FWHM_{\text{air}} = 40$ mm, $FWHM_{\text{water}} = 42$ mm) and their ratio (0.9091) denotes the proportional change in fluence due to beam spread. The experimentally derived calibration factor is then used for photon quantification within tissue-like media:

$$\phi_{\text{calorimeter}} = \frac{(CF * \phi_{\text{probe}}) + 1.7296}{590.46} \quad (3)$$

where $\Phi_{\text{calorimeter}}$ is the absolute energy fluence rate in mW/mm^2 and Φ_{probe} is the fluence measured by the probe (mW/mm^2). The absolute energy fluence rate can be converted to energy fluence (Φ'_{absolute}) (J/mm^2) by integrating it over the illumination time.

D. Beam Profile Modeling Using the Monte Carlo

The original code of the GPU-based 3D MC was advanced to emit a broad-beam super-Gaussian beam profile emanating from an optical fiberguide: $\phi_{\text{SG}} = e^{-0.5(\frac{r}{\sigma})^n}$, where $r = z \tan \theta$, θ is the divergence angle, z is the depth along the beam axis, σ is the standard deviation of the super-Gaussian beam, n is the order of the super-Gaussian distribution. For these studies, the measured broad super-Gaussian beam was simulated using multiple point sources, each with a super-Gaussian output ($\sigma = 3.8$ and $n = 2.9$) for a source (fiberguide) of radius 0.3 cm. In addition to the super-Gaussian beam, a flat broad beam with radius equal to the output port of the integrating sphere (port radius 0.9 cm) was implemented, similar to other studies. The beam characteristics, phantom dimensions, and optical properties of the phantom were inputted to the MC code (and empirical model code) to emulate the illumination conditions used in the optical dosimetry setup of Fig. 7(a). A total of 10^8 photons were simulated per beam.

E. Validation of the 3D Monte Carlo in Brain Phantoms Using Optical Dosimetry

As described in Section 2.A, liquid optical phantoms, resembling white matter, gray matter, and skull bone, were designed using predetermined concentrations of India ink and intralipid. The setup for the light dosimetry in the phantoms is similar to that shown in Fig. 7(a). Cuvette dimensions were $5.3 \text{ cm} \times 4.6 \text{ cm} \times 3.1 \text{ cm}$, thickness = 0.4 cm. Two beam profiles—flat-top and super-Gaussian—were used to illuminate these phantoms with the laser/optical parametric oscillator (OPO) system tuned to 800 nm. The 3D energy fluence rate distribution was determined by translating the optical dosimetry probe positioned within the brain phantom using a three-axis micrometer stage. These measurements were compared to Monte Carlo generated data to test the validity and accuracy of the Monte Carlo code (Figs. 8–11). The error% was averaged over profiles measured and calculated at different depths within the phantom along and perpendicular to the beam axis.

In order to quantify the photon energy fluence (in J/mm^2) brain tissues, we converted the output of the Monte Carlo fluence ($\Phi_{\text{photons}}/\text{mm}^2$) as follows:

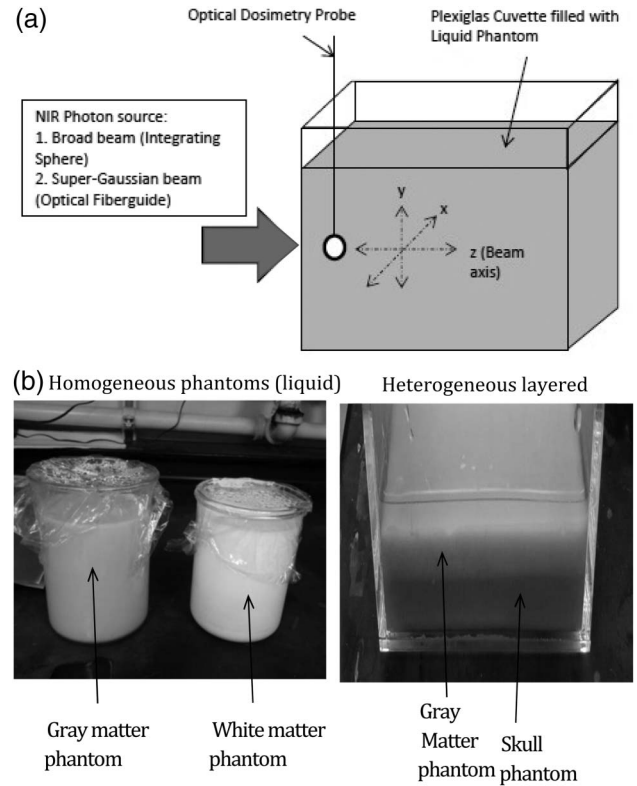


Fig. 7. (a) Setup for optical dosimetry in a liquid phantom. The optical dosimetry probe is translated within a Plexiglas cuvette filled with liquid phantom, and illuminated by an NIR source. This setup is used for intralipid calibration as well as for actual phantom studies. (b) Pictures of homogeneous liquid phantoms (left) and heterogeneous layered agar phantoms (right). In the heterogeneous phantom a white matter liquid phantom (not shown) is added on top of the gray matter solid agar layer for dosimetry measurements.

Probe versus Monte Carlo (White Matter, Gray Matter)
(Source: Integrating Sphere)

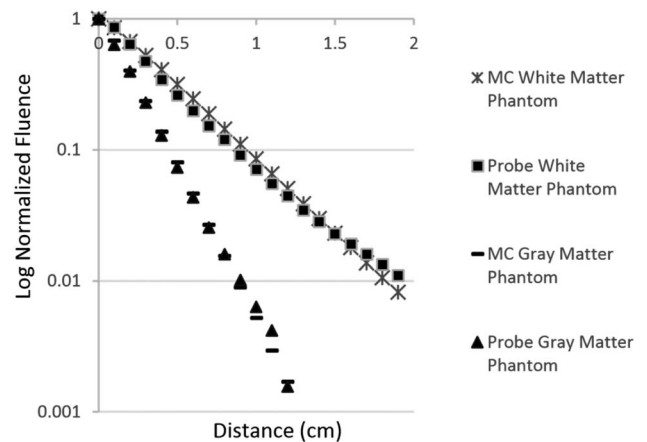


Fig. 8. Optical dosimetry in white and gray matter phantoms (cuvette dimensions: $5.3 \text{ cm} \times 4.6 \text{ cm} \times 3.1 \text{ cm}$, thickness = 0.4 cm). The photon source used is an integrating sphere connected to a pulsating laser source. The graphs show the exponential decrease of photon fluence along the beam axis in white and gray matter mimicking phantoms. The Monte Carlo generated fluence closely matches the fluence measured by the probe.

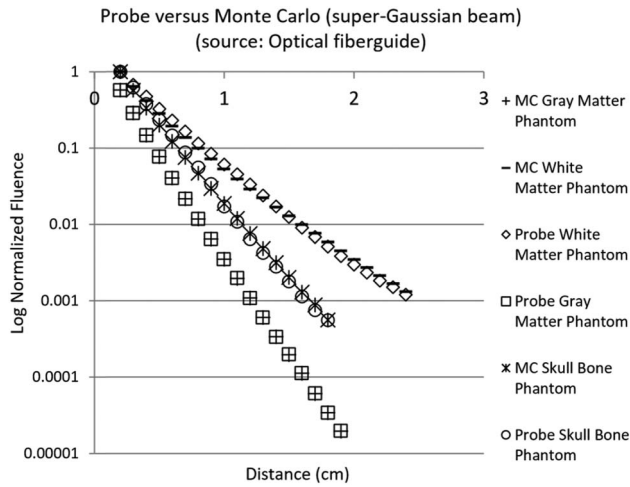


Fig. 9. Optical dosimetry in white matter, gray matter, and skull bone phantoms (cuvette dimensions: 5.3 cm × 4.6 cm × 3.1 cm, thickness = 0.4 cm). The photon source used is an optical fibreguide (connected to a pulsating laser source) with a super-Gaussian beam distribution. The Monte Carlo generated fluence closely matches the fluence measured by the probe. This shows that the Monte Carlo beam modeling can be reliably used as a reliable estimator of photon energy distribution in tissue phantoms.

$$\phi \text{ (J/mm}^2\text{)} = \phi_{\text{MC}} * \frac{hc}{\lambda}, \quad (4)$$

where h is Planck's constant, c and λ are the speed and wavelength of light in the medium. The energy deposited (E_{dose} in J/mm³) in the tissue is obtained by multiplying the photon dose with the absorption coefficient μ_a :

$$E_{\text{dose}} \text{ (J/mm}^3\text{)} = \phi_{\text{MC}} * \mu_a * \frac{hc}{\lambda}. \quad (5)$$

F. Empirical Algorithm for Photon Propagation

The empirical model approach is based on the assumption that the photon fluence in a voxel in a particular layer is a weighted sum of the fluences of neighboring voxels in the previous layer. The schematic of this algorithm is shown in Fig. 12. The steps of the algorithm can be summarized as follows:

1. Assign the incident photon beam distribution (e.g., super-Gaussian beam) to the first layer of voxels entering the tissue phantom. In this case, the direction of photon propagation is along the $+z$ direction.
2. For every voxel in a layer, calculate the 14 directional scatter components and accumulate total fluence by summing the directional fluences in each voxel:

$$\begin{aligned} I(i, j, k) = & I_f(i, j, k-1) + I_{dr}(i-1, j, k-1)wt_2 \\ & + I_{df}(i, j-1, k-1)wt_2 + I_{db}(i, j+1, k-1)wt_2 \\ & + I_{dl}(i+1, j, k-1)wt_2, \end{aligned} \quad (6)$$

$$\begin{aligned} I(i, j, k) = & I_f(i, j, k) + I_{dr}(i, j, k) \\ & + I_{dl}(i, j, k) + I_{df}(i, j, k) + I_{db}(i, j, k) \\ & + I_{sr}(i, j, k) + I_{sl}(i, j, k) + I_{sf}(i, j, k) \\ & + I_{sb}(i, j, k) + I_{dbr}(i, j, k) + I_{dbl}(i, j, k) \\ & + I_{dbf}(i, j, k) + I_{dbb}(i, j, k) + I_b(i, j, k). \end{aligned} \quad (7)$$

The nomenclature for the 14 directional fluence vectors is shown in Table 3. Equation (6) represents an example of how the forward scatter component is calculated. The coordinates i, j, k denote the x, y , and z location of the voxel. The weights wt_1 and wt_2 are forward and diagonal scattering weights. The sum of all weights is always equal to one (i.e., $wt_1 + 4 * wt_2 = 1$), so that the total fluence entering a voxel is equal to the sum of fluence absorbed and exiting the voxel. The equations used to calculate the other components can be similarly determined. The sum of all the scatter components in a voxel equals the total fluence in that voxel (arbitrary units: photons/unit volume), as shown by Eq. (7).

3. Calculate absorbed fluence (I_{abs}) using the Beer-Lambert law for a path length dl equal to the voxel length, based on the absorption coefficient (μ_a) of the voxel:

$$I_{\text{abs}(i,j,k)} = I(i, j, k) * (1 - e^{-\mu_a * dl}). \quad (8)$$

4. Calculate and accumulate the fluence over all voxels in the current layer and increment z to proceed to the next layer. Continue propagation until the fluence exits the volume.

The weights to be assigned for scatter were obtained by an iterative optimization phase, which compares the output fluence of the empirical algorithm to that generated by the Monte Carlo routine for voxels along the beam axis, as calculated by the R-square coefficient (R^2). Table 4 shows the weights (wt_1 and wt_2) obtained for a pencil beam simulation within different tissue types. Figure 11 shows an example of the match in fluence profiles between the Monte Carlo and the empirical approach.

3. RESULTS AND DISCUSSION

A. Optical Dosimetry Probe Calibration

The isotropicity (coefficient of variation) of nylon- and titanium-based optical dosimetry probes are shown in Fig. 5(a). The titanium-based probes demonstrated a significantly improved isotropicity with an equatorial coefficient of variation 0.038–0.072 versus 0.193 for the nylon and an azimuthal coefficient of variation ranging from 0.21–0.29 versus 0.44 for the nylon. This is a 2–5 × overall better isotropicity, depending on the concentration of TiO₂. Figure 6(b) shows the linearity of response of the 1.5 mm titanium probe. The measurement error in probe response was 1.7%, and 1.1% in the calorimeter readings, where the majority of this error was due to variation in the output power of the laser (3% absolute deviations). Thus, the titanium probes proved to be better suited to optical dosimetry studies compared to nylon probes and hence were used in brain phantom studies. While nylon probes have been used before, this is the first time that titanium probes were designed and shown to have a better isotropic response. Previous studies have measured the isotropicity of dosimetry probes made of Arnite (11%), nylon (11%),

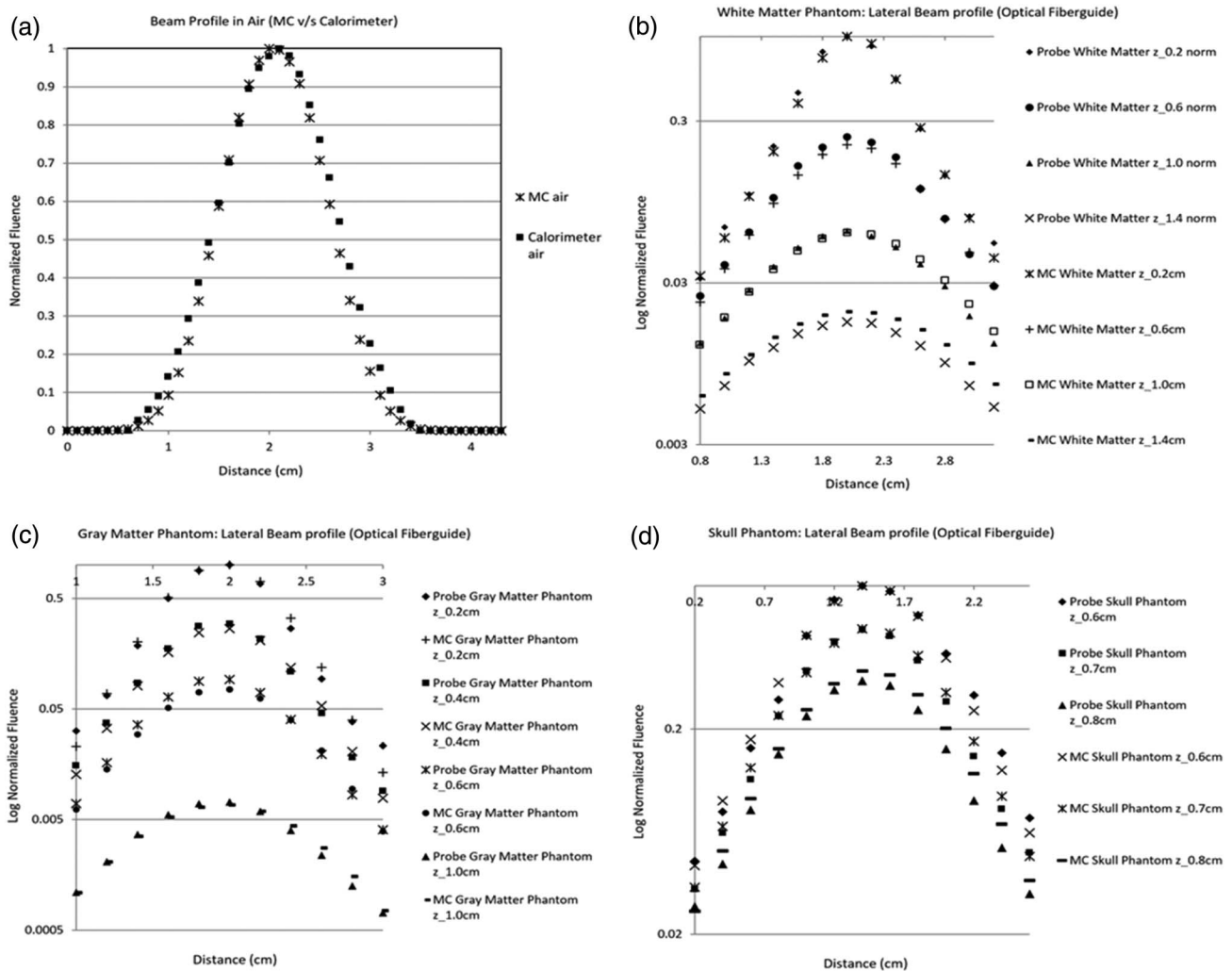


Fig. 10. Lateral beam profile measurement using optical dosimetry probe and validation by Monte Carlo in homogeneous phantoms. The laser source used was an optical fiberguide (0.3 cm diameter) connected to a pulsed NIR laser emitting at a wavelength of 800 nm. Cuvette dimensions: 5.3 cm \times 4.6 cm \times 3.1 cm, thickness = 0.4 cm. (a) Beam characterization in air using calorimeter. Optical dosimetry to measure and validate lateral beam profiles in phantoms resembling: (b) white matter, (c) gray matter, and (d) skull bone, i.e., perpendicular to the beam axis. The measurements have been normalized to the maximum value measured by the dosimetry probe in each of the respective phantoms. The Monte Carlo generated fluence closely matches the probe-measured fluence and effectively models the beam spread in tissue phantoms.

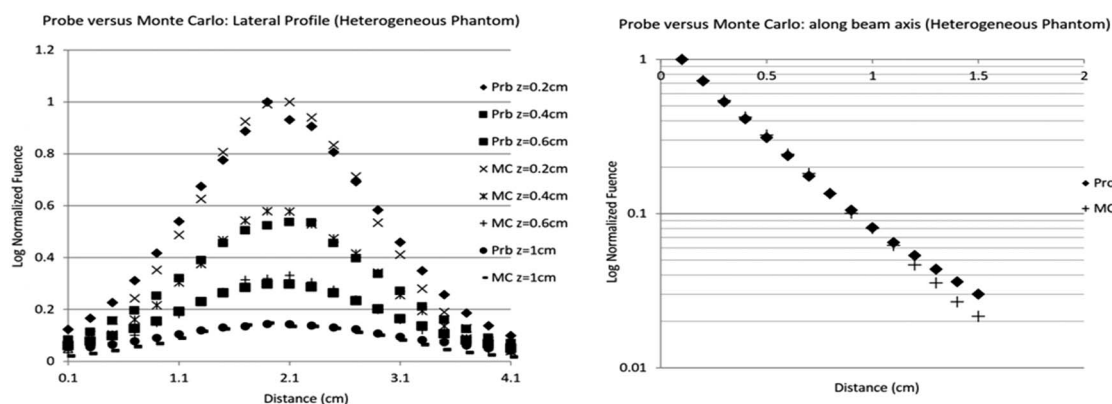


Fig. 11. Validation of Monte Carlo in a heterogeneous phantom (1.1 cm skull agar, 1.1 cm gray matter agar, and 5.9 cm white matter liquid). Lateral profile measurements (in the white matter phantom solution) are shown on the left while axial comparison is on the right. The depth shown by z is the distance from the gray matter agar surface.

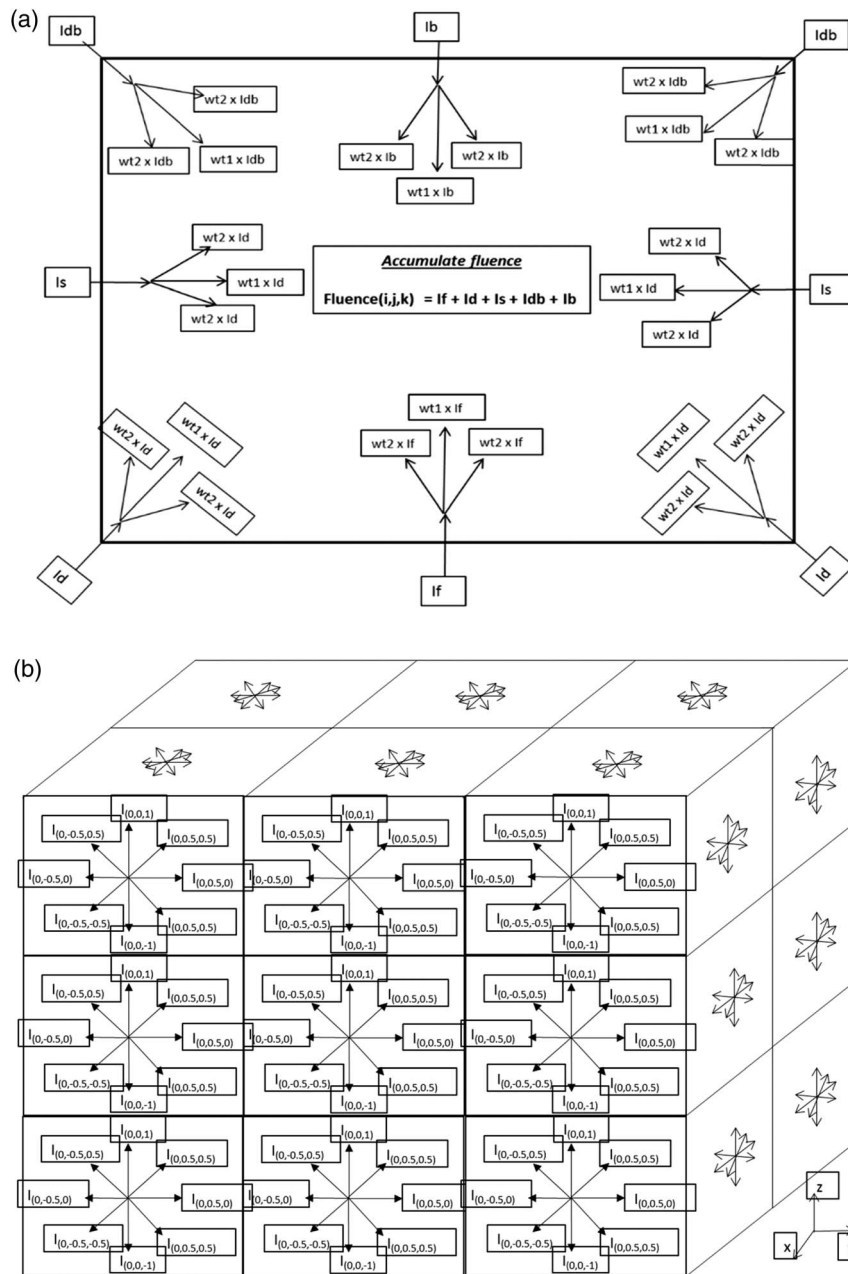


Fig. 12. Empirical method for 3D photon propagation. The fluence at each voxel in a layer is a weighted sum of the neighboring fluences in adjoining voxels. Part A shows the simplified schematic of fluence accumulation (in 2D), while the actual 3D model with directional fluence components is shown in part B of the figure. The fluence in each voxel consists of forward, backward, side, and diagonal fluence components (mentioned in Table 3). The directional fluences are first calculated in each voxel along with the total fluence, before being propagated to neighboring voxels.

Helioseal dental sealant (20%) [17,19]. Our study measured the % variation of the best titanium probe to be 13% and the best nylon probe to be 17%. The differences in probe construction and calibration setup contribute to different measured isotropicity of the same probe material (e.g., nylon) across various studies.

To quantify the photon fluence in tissues and tissue-like media, the probe voltage measured within the medium must be multiplied by a set of calibration factors to account for the change in photon acceptance and loss in the probe-medium interface with respect to the probe-air interface. Since the

refractive index of tissues is nearly the same as that of water, the calibration factor obtained for water can be used for biological media. The probe calibration factor was determined to be 1.32. The technique presented in Section 2.C [using Eqs. (1)–(3)] provides a simple and new method to determine the calibration factor experimentally.

B. Validation of Monte Carlo in Homogeneous Phantom Using the Optical Dosimetry Probe

The optical fluence measured by the ODPs in white and gray matter phantoms was compared to the Monte Carlo generated

Table 3. Vector Directions and Nomenclature Empirical Algorithm

Vector Name	Vector Component $s(x, y, z)$	Description
If	(0 0 1)	Upward vector in $+z$ direction
lb	(0 0 -1)	Downward vector in $-z$ direction
Isf	(0 1 0)	Side vector in $+y$ direction
Isb	(0 -1 0)	Side vector in y direction
Isr	(1 0 0)	Side vector in $+x$ direction
Isl	(-1 0 0)	Side vector in $-x$ direction
Idf	(0 0.5 0.5)	Upward diagonal vector in $+z$ and $+y$ direction
Idb	(0 -0.5 0.5)	Upward diagonal vector in $+z$ and $-y$ direction
Idr	(0.5 0 0.5)	Upward diagonal vector in $+z$ and $+x$ direction
Idl	(-0.5 0 0.5)	Upward diagonal vector in $+z$ and $-x$ direction
Idbf	(0 0.5 -0.5)	Downward diagonal vector in $-z$ and $+y$ direction
Idbb	(0 -0.5 -0.5)	Downward diagonal vector in $-z$ and $-y$ direction
Idbr	(0.5 0 -0.5)	Downward diagonal vector in $-z$ and $+x$ direction
Idbl	(-0.5 0 -0.5)	Downward diagonal vector in $-z$ and $-x$ direction

Table 4. Optimization of Empirical Algorithm for Brain Tissue Phantoms

Tissue Phantom	Resolution (mm)	Wt1	Wt2	R2 Coefficient
White matter	0.1	0.949461	0.012635	0.99999
Gray matter	0.1	0.87469	0.031328	0.999969
Skull bone	0.1	0.914828	0.021293	0.99979
White matter	1	0.474876	0.131281	0.99992
Gray matter	1	0.062097	0.234476	0.999828
Skull bone	1	0.245949	0.188513	0.999871

fluence maps to validate the Monte Carlo. These experiments necessitate an accurate determination of the phantom's optical properties. Figures 8 and 9 show the comparison between the probe measurements and the Monte Carlo in brain phantoms for two different illumination profiles, flat diffuse beam (integrating sphere) and super-Gaussian beam (optical fiberguide). A comparison was also made in the direction perpendicular to the beam axis, as shown in Fig. 10. From these data, the average relative % error of the Monte Carlo simulation relative to the probe measurements was 11.2% for white matter, 13.2% for gray matter, and 11.8% for skull bone along the beam axis for a range of 0.2–2.0 cm within the phantom, while perpendicular to the beam axis, the % relative error in the lateral profile was 9.4%, 12.0%, and 8.9% for white matter, gray matter, and skull bone phantoms, respectively. These systematic errors represent the level of confidence with which the Monte Carlo matches the probe measurements and validate their use in simulating optical energy distribution in media (Tables 5 and 6).

An analysis of the fluence profile within the skull phantom showed that the super-Gaussian beam fluence decreases with an

Table 5. % Mismatch Error in Homogeneous Phantom Along Beam Axis (z)

Phantom	Error% (0.2–1 cm)	Error% (1–2 cm)	Average Error%
White matter	12.13	10.5	11.27
Gray matter	13.39	30.12	13.25
Skull bone	11.39	12.28	11.81

effective attenuation coefficient of 4.81 cm^{-1} . This factor was used to estimate the effectiveness of therapy for different skull thicknesses. Based on Monte Carlo simulated data, the powers transmitted by the fiberguide source for various skull thicknesses are: 5.9 mW/cm^2 (0.4 cm thick), 2.16 mW/cm^2 (0.6 cm thick), 0.83 mW/cm^2 (0.8 cm thick), 0.33 mW/cm^2 (1 cm thick). Thus, the % power transmitted in a 1 cm thick adult skull is 1.8%, while in a pediatric skull with a thickness of 4.0 mm, 33.5% optical power would reach the soft tissue, representing 18.5 times more fluence.

C. Validation of Monte Carlo in Heterogeneous Phantom Using the Optical Dosimetry Probe

Energy fluence distribution was measured in the white matter volume of a heterogeneous head phantom, which consisted of a 1.1 cm thick skull agar phantom, a 1.1 cm thick gray matter agar phantom, and a 5.9 cm thick white matter liquid phantom (Fig. 7). The exponential decreases in energy fluence along the beam axis and the lateral beam profiles at different depths above the gray matter agar surface are shown in the right and left plots of Fig. 11. The lateral fluence profiles have been normalized to the intensity at a depth of 0.2 cm above the gray matter agar surface, while the fluence profiles along the beam axis were normalized to the fluence at $z = 0.1 \text{ cm}$ above the gray matter agar surface. The average error (relative % error) between the probe and Monte Carlo fluence was 17.7% along the beam axis and 18.0% perpendicular to the beam axis (Tables 7 and 8). These results demonstrate that the beam spread can be determined accurately by the Monte Carlo to an overall depth of nearly 4 cm given the optical coefficients of the head phantom.

Past studies have compared the Monte Carlo simulations to dosimetry probe measurements for simple beam profiles, such as flat beams or isotropic sources [14,15]. One study compared the angular radiance measured by a flat cleaved dosimetry probe to that simulated by the Monte Carlo and determined an accuracy of around 25% (see Fig. 6 in referenced publication) [14]. Another study validated the Monte Carlo in pig bronchus tissue using dosimetry probe measurements with errors up to 50% at 4 cm depth and systematic variation of 15% [15]. In past studies, the long computation times ($>24 \text{ h}$) associated with the CPU-based Monte Carlo prevented a rigorous approach to Monte Carlo validation across diverse tissue types and under different illuminations. Another source of error in these studies was the uncertainty in the estimation of tissue/phantom optical properties. In this study, we have minimized this uncertainty by independently validating the optical properties. The use of a GPU-based Monte Carlo reduces the development time (few hours) associated with optimizing the Monte Carlo for complex illumination and boundary conditions.

Table 6. % Mismatch Error in Homogeneous Phantom Perpendicular to Beam Axis

Phantom	Error% $z = 0.2$ cm	Error% $z = 0.6$ cm	Error% $z = 1.0$ cm	Error% $z = 1.4$ cm	Average Error%
White matter	10.34	13.34	9.14	4.79	9.4
Phantom	Error% $z = 0.2$ cm	Error% $z = 0.4$ cm	Error% $z = 0.6$ cm	Error% $z = 1$ cm	Average error%
Gray matter	13.45	11.52	14.29	8.97	12.06
Phantom	Error% $z = 0.6$ cm	Error% $z = 0.7$ cm	Error% $z = 0.8$ cm	Average error%	
Skull bone	8.41	5.69	12.64	8.91	

Table 7. % Mismatch Error in Heterogeneous Phantom Along Beam Axis (z)

Phantom	Error% (0.1–1 cm)	Error% (1–2 cm)	Average Error%
White matter (over skull and gray matter layers)	2.11	33.32	17.71

Table 8. % Mismatch Error in Heterogeneous Phantom Perpendicular to Beam Axis

Phantom	Error% $z = 0.2$ cm	Error% $z = 0.4$ cm	Error% $z = 0.6$ cm	Error% $z = 1$ cm	Average Error%
White matter (over skull and gray matter layers)	18.52	15.09	15.37	23.17	18.04

The use of pulsed laser beams has been shown to improve the instantaneous temperature rise and release of drug molecules tethered to nanoparticles, compared to continuous-wave lasers [42]. This will allow more instantaneous power to be coupled to the nanomolecules while reducing the chances of laser-induced adverse tissue heating. Assuming nanosecond pulse duration, the maximum permissible exposure limit of laser for skin is $3.17 \times 10^7 \text{ W cm}^{-2}$ [41,42]. Based on our MC simulations with a flat 2 cm diameter beam, the amount of

fluence coupled to the soft tissue for a 1.1 cm thick skull is $4.3 \times 10^5 \text{ W cm}^{-2}$ and $1.5 \times 10^7 \text{ W cm}^{-2}$ for neonatal heads with a 0.2 cm thick skull. Thus, a drug needs to be designed to activate at a fluence threshold, less than the maximum fluence coupled to the tissues at a specific depth where the metastasis is located. For example, a drug molecule with an activation threshold of 1 W cm^{-2} can be activated up to 3.8 cm in the white matter of a 20 cm diameter adult brain (1.1 cm thick skull plus 2 cm gray matter) and up to 4.6 cm in a 8 cm diameter neonatal brain (0.2 cm skull plus 0.2 cm gray matter). These results demonstrate that NIR activated drug release is more feasible in neonatal brains where 4.6 cm is greater than half of the brain diameter. The temporal widening of the laser pulse with depth in the brain is also seen to affect the instantaneous fluence ($\text{W} \cdot \text{cm}^{-2} \cdot \text{s}$) coupled to tissues. Based on our Monte Carlo simulations, the pulse width is seen to be 4–5 times at depths of 3–5 cm for a 1 ns wide input laser pulse. This implies a decrease in instantaneous fluence by that amount. The Monte Carlo can be used to predict the temporal beam widening in order to determine the instantaneous fluence at specific depths.

D. Empirical Versus Monte Carlo

In Figs. 12 and 13, a schematic of the EM used in these studies is presented and the corresponding weights determined by matching photon fluence results to MC data. As seen in Table 4, the weights obtained during optimization depend on the voxel size and the scattering coefficient of the medium. The scattering coefficient and the voxel size determine the number of scattering events per unit volume, which affects

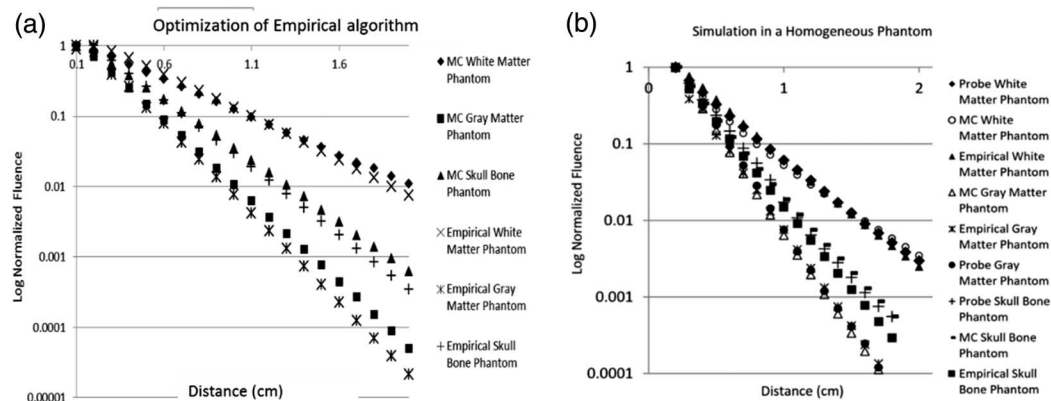


Fig. 13. (a) Optimization phase: a flat broad beam (2 cm diameter) is simulated using Monte Carlo and the empirical algorithm is optimized to match the Monte Carlo with the identical illumination conditions. (b) Comparison of the empirical algorithm with Monte Carlo and probe-measured fluence in brain phantoms resembling white matter, gray matter, and skull bone. The illumination source is a super-Gaussian beam. The empirical approach is a close approximation of the Monte Carlo and the probe over the range of optical properties of brain tissues.

the percentage scatter in the forward versus diagonal directions, thus impacting the weights (wt1 and wt2). Based on these weights, EM simulated data for homogeneous and heterogeneous phantoms were compared to Monte Carlo and ODP measurements. This comparison was performed along the beam axis, see Fig. 13(b), in homogeneous brain tissue phantoms. The average relative % error between the empirical and probe measurements for the super-Gaussian beam simulation is 10.1% for white matter, 45.2% for gray matter, and 22.1% for skull bone phantoms; while the comparison between empirical and MC is 22.6% for white matter, 35.8% for gray matter, and 21.9% for skull bone measurements. The errors between probe measurements and the empirical algorithm are cumulative in nature, and can be reduced with better optimization methods. No systemic trend was observed in these errors with % differences having both positive and negative values. Figure 14 shows a comparison between the lateral

fluence profiles generated by a Monte Carlo and the empirical models for a flat beam of 20 mm diameter in homogeneous white and gray matter tissues. A significant match is seen between the normalized fluence profiles at two different depths. Figure 15 shows a complete head simulation and the comparison between the MC and empirical fluence versus depth along the beam axis. The empirical fluence closely follows the Monte Carlo but has significant errors at object boundaries.

The Monte Carlo code is computationally expensive in spite of being based on a GPU-based platform. In order to simulate the optical properties and fine structural boundaries of brain tissues, a resolution equal to or less than 1 mm is necessary. Even though an optical map of the brain can be obtained through segmenting and translating CT and/or MR images, the dataset size of the brain becomes very large, e.g., a CT scan requires a $512 \times 512 \times 512$ matrix. This significantly increases the execution time of the Monte Carlo routine to iterate over

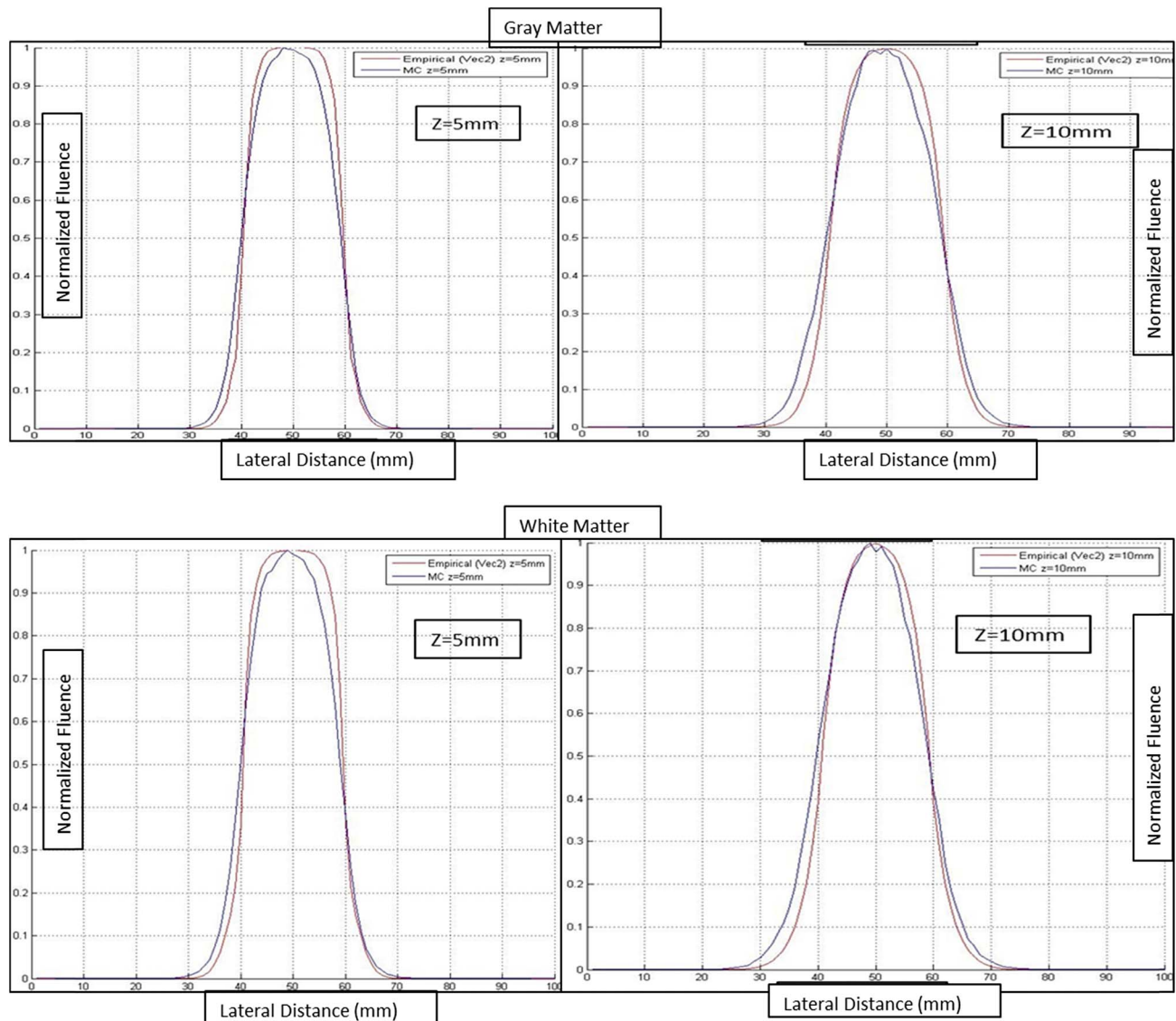


Fig. 14. Lateral beam profile comparison between normalized lateral fluence profiles of empirical (red line) and Monte Carlo (blue line) for gray matter and white matter tissue at depths of 5 and 10 mm in a homogeneous phantom. A flat broad beam (20 mm diameter) is simulated. A close match is seen between the Monte Carlo and empirical lateral beam profiles.

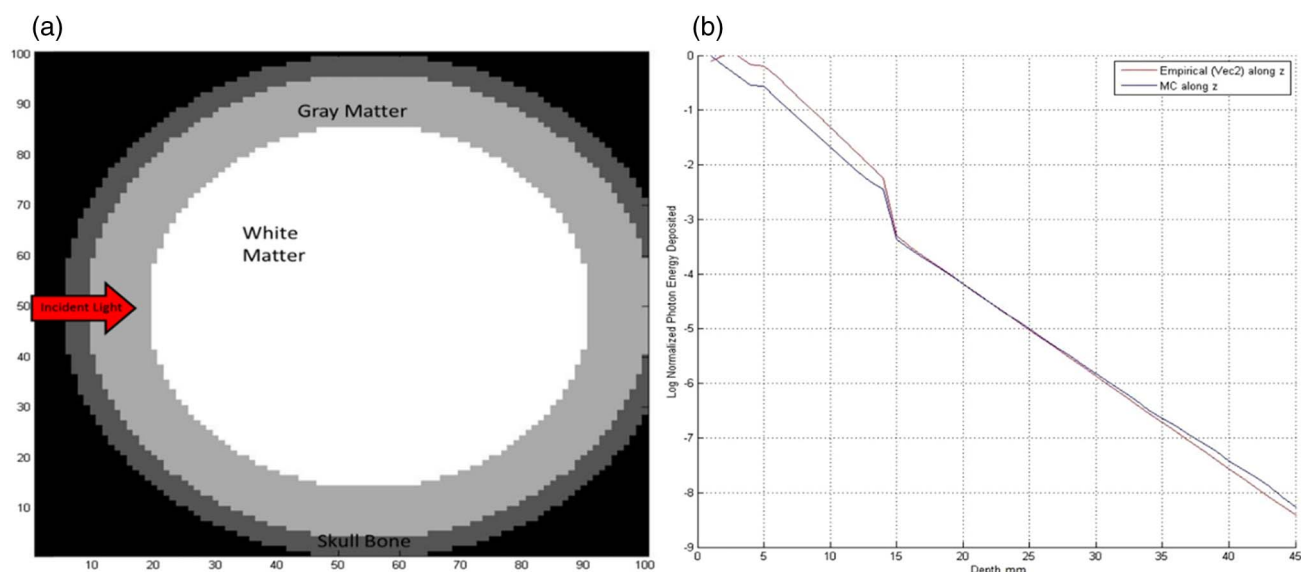


Fig. 15. (a) Simulation of a spherical head phantom with brain tissue properties shown in Table 1. Skull thickness = 4 mm; gray matter thickness = 10 mm, white matter diameter = 72 mm. Uniform illumination beam diameter = 20 mm (800 nm wavelength). (b) Comparison of fluence along the beam axis between empirical (red line) and MC (blue line) models. The empirical model achieves this simulation in 6 s while the MC takes 8 h for a total of 10^{10} photons.

various illumination conditions. The empirical approach provides an alternative to the computationally expensive Monte Carlo, and can be used to select the best illumination conditions for therapy. The speed-up achieved by the empirical algorithm was approximately $700 \times$ for a pencil beam simulation and $16,000 \times$ for a broad-beam simulation in a head phantom. Thus while a broad-beam head simulation takes 6 s with the empirical, it can take in excess of 8 h with the GPU-based Monte Carlo for a head phantom simulation of volume 1000 cm^3 . It is important to note that the number of photons to be simulated depends on the depth at which the photon distribution is to be evaluated, and the % fluence penetration (and systematic errors between MC, probe, and empirical) is independent of the number of photons simulated.

4. CONCLUSION

We validated the 3D Monte Carlo using a novel optical dosimetry probe in phantoms resembling white matter, gray matter, and skull bone. The TiO_2 -based dosimetry probe was shown to have superior linearity and isotropicity of response, and was better suited to validate the Monte Carlo using localized 3D measurement ($<25\%$ error) in tissue phantoms. The independent characterization of the probes and the optical phantoms using the calorimeter “gold standard” and spectrophotometer (respectively) further validate our results. The 3D validation of the Monte Carlo generated fluence for two different types of NIR light sources in different optical phantoms, and the ease of photon quantification to absolute dose (in mW/mm^2 or J/mm^2) demonstrates the fidelity of the Monte Carlo as a predictive tool to accurately estimate 3D photon energy distribution in complex media. The measurement and prediction accuracy can be improved with better instrumentation for probe localization and better laser beam positioning setups. The voxel-based Monte Carlo can emulate the complex

geometrical shape of tissues using imaging datasets such as CT/MRI and can now be used as a predictive clinical tool to estimate photon dose in heterogeneous brain tissues.

The empirical algorithm, validated by the 3D Monte Carlo, increases the clinical feasibility of optical therapeutic planning to narrow down the complex possibilities of illumination conditions, further compounded by the heterogeneous structure of the brain (e.g., varying skull thicknesses and densities). A limitation of using the empirical approach is that the weights assigned depend on the resolution of the medium and changing resolution requires an optimization phase to derive the weights. A rigorous validation of the empirical approach is currently under development, which is necessary for its applicability in heterogeneous tissue environments in clinical settings. Despite its limitations, it can be used as a preliminary step, with the final estimation done by the Monte Carlo to ensure high predictive accuracy.

Our ultimate goal is to design a fast Monte Carlo-based optical therapeutic protocol to treat brain metastasis. This requires voxel by voxel determination of photon energy distribution to accurately predict the rate/quantity of drug release. This study achieves the first step in the design of a tool to validate the NIR photon distribution in three dimensions in optical phantoms, where tissue structure and boundaries can be determined from imaging modalities such as MRI or CT.

Funding. Congressionally Directed Medical Research U.S. Department of Defense (DOD) Breast Cancer Research Program (W81XWH-13-1-034); National Institutes of Health (NIH)/National Institute of Biomedical Imaging and Bioengineering (NIBIB) (NIH/NIBIB R21 EB012752); Purdue Research Foundation (Grant 2014).

Acknowledgment. We thank Justin Sick for help with the optical dosimetry setup.

REFERENCES

1. J. P. A. Marijnissen, W. M. Star, J. L. van Delft, and N. A. P. Franken, "Light intensity measurements in optical phantoms and *in vivo* during HPD-photoradiation treatment, using a miniature light detector with isotropic response," in *Photodynamic Therapy of Tumours and Other Diseases*, G. Jori and C. Perria, eds. (Libreria Progetto, 1985), p. 38790.
2. M.-R. Choi, K. J. Stanton-Maxey, J. K. Stanley, C. S. Levin, R. Bardhan, D. Akin, S. Badve, J. Sturgis, J. P. Robinson, R. Bashir, N. J. Halas, and S. E. Clare, "A cellular Trojan Horse for delivery of therapeutic nanoparticles into tumors," *Nano Lett.* **7**, 3759–3765 (2007).
3. M.-R. Choi, R. Bardhan, K. J. Stanton-Maxey, S. Badve, H. Nakshatri, K. Stantz, N. Cao, N. J. Halas, and S. E. Clare, "Delivery of nanoparticles to brain metastases of breast cancer using a cellular Trojan horse," *Cancer Nano* **3**, 47–54 (2012).
4. W. M. Star, "Comparing the P3-approximation with diffusion theory and with Monte Carlo calculations of light propagation in a slab geometry," *Proc. SPIE* **IS5**, 146–154 (1989).
5. G. Yoon, S. A. Prahl, and A. J. Welch, "Accuracies of the diffusion approximation and its similarity relations for laser irradiated biological media," *Appl. Opt.* **28**, 2250–2255 (1989).
6. M. J. C. Gemert, A. J. Welch, W. M. Star, M. Motamedi, and W. F. Cheong, "Tissue optics for a slab geometry in the diffusion approximation," *Lasers Med. Sci.* **2**, 295–302 (1987).
7. L. Wang, S. L. Jacques, and L. Zheng, "Monte Carlo modeling of light transport in multilayered tissues," *Comput. Methods Prog. Biomed.* **47**, 131–146 (1995).
8. D. A. Boas, J. P. Culver, J. J. Stott, and A. K. Dunn, "Three dimensional Monte Carlo code for photon migration through complex heterogeneous media including the adult human head," *Opt. Express* **10**, 159–170 (2002).
9. Q. Fang and D. A. Boas, "Monte Carlo simulation of photon migration in 3D turbid media accelerated by graphics processing units," *Opt. Express* **17**, 20178–20190 (2009).
10. A. P. Verleker, Q. Fang, M.-R. Choi, S. Clare, and K. M. Stantz, "An optical therapeutic protocol to treat brain metastasis by mapping NIR activated drug release: a pilot study," in *IEEE Nuclear Science Symposium and Medical Imaging Conference Record* (2014), pp. M19–M96.
11. L. V. Wang, ed., *Photoacoustic Imaging and Spectroscopy* (CRC press, 2009).
12. C. E. Elwell, M. Cope, A. D. Edwards, J. S. Wyatt, D. T. Delpy, and E. O. Reynolds, "Quantification of adult cerebral hemodynamics by near-infrared spectroscopy," *J. Appl. Phys.* **77**, 2753–2760 (1994).
13. M. Chernov and A. W. Roe, "Infrared neural stimulation: a new stimulation tool for central nervous system applications," *Neurophotonics* **1**, 011011 (2014).
14. O. Barajas, Å. M. Ballangrud, G. G. Miller, R. B. Moore, and J. Tulip, "Monte Carlo modelling of angular radiance in tissue phantoms and human prostate: PDT light dosimetry," *Phys. Med. Biol.* **42**, 1675–1687 (1997).
15. L. H. P. Murrer, J. P. A. Marijnissen, and W. M. Star, "Ex vivo light dosimetry and Monte Carlo simulations for endobronchial photodynamic therapy," *Phys. Med. Biol.* **40**, 1807–1817 (1995).
16. J. P. Marijnissen and W. M. Star, "Phantom measurements for light dosimetry using isotropic and small aperture detectors," *Prog. Clin. Biol. Res.* **170**, 133–148 (1984).
17. H. J. Van Staveren, H. P. Marijnissen, M. C. Aalders, and W. M. Star, "Construction, quality assurance and calibration of spherical isotropic fibre optic light diffusers," *Lasers Med. Sci.* **10**, 137–147 (1995).
18. I. Driver, C. P. Lowdell, and D. V. Ash, "In vivo measurement of the optical interaction coefficients of human tumours at 630 nm," *Phys. Med. Biol.* **36**, 805–813 (1991).
19. J. P. A. Marijnissen and W. M. Star, "Calibration of isotropic light dosimetry probes based on scattering bulbs in clear media," *Phys. Med. Biol.* **41**, 1191–1208 (1996).
20. W. M. Star, "Light dosimetry *in vivo*," *Phys. Med. Biol.* **42**, 763–787 (1997).
21. J. P. A. Marijnissen and W. M. Star, "Performance of isotropic light dosimetry probes based on scattering bulbs in turbid media," *Phys. Med. Biol.* **47**, 2049–2058 (2002).
22. A. P. Verleker, Q. Fang, M.-R. Choi, S. Clare, and K. M. Stantz, "An empirical approach to estimate near-infra-red photon propagation and optically induced drug release in brain tissues," *Proc. SPIE* **9308**, 93080T (2015).
23. Q. Fang, S. A. Carp, J. Selb, G. Boverman, Q. Zhang, D. B. Kopans, and D. A. Boas, "Combined optical imaging and mammography of the healthy breast: optical contrast derived from breast structure and compression," *IEEE Trans. Med. Imaging* **28**, 30–42 (2009).
24. G. Yoon, S. A. Prahl, and A. J. Welch, "Accuracies of the diffusion approximation and its similarity relations for laser irradiated biological media," *Appl. Opt.* **28**, 2250–2255 (1989).
25. L. Wang and S. L. Jacques, "Hybrid model of Monte Carlo simulation and diffusion theory for light reflectance by turbid media," *J. Opt. Soc. Am. A* **10**, 1746–1752 (1993).
26. A. Joshi, J. C. Rasmussen, E. M. Seveck-Muraca, T. A. Wareing, and J. McGhee, "Radiative transport-based frequency-domain fluorescence tomography," *Phys. Med. Biol.* **53**, 2069–2088 (2008).
27. S. Chandrasekhar, *Radiative Transfer*, S. Chandrasekhar, ed. (Dover, 1960), p. 20.
28. H. C. Van de Hulst, *Multiple Light Scattering: Tables, Formulas, and Applications* (Elsevier, 2012).
29. P. Van der Zee, M. Essenpreis, and D. T. Delpy, "Optical properties of brain tissue," in *OE/LASE'93: Optics, Electro-Optics, and Laser Applications in Science and Engineering* (International Society for Optics and Photonics, 1993).
30. M. Firbank, M. Hiraoka, M. Essenpreis, and D. T. Delpy, "Measurement of the optical properties of the skull in the wavelength range 650–950 nm," *Phys. Med. Biol.* **38**, 503–510 (1993).
31. W.-F. Cheong, S. A. Prahl, and A. J. Welch, "A review of the optical properties of biological tissues," *IEEE J. Quantum Electron.* **26**, 2166–2185 (1990).
32. S. J. Madsen, M. S. Patterson, and B. C. Wilson, "The use of India ink as an optical absorber in tissue-simulating phantoms," *Phys. Med. Biol.* **37**, 985–993 (1992).
33. I. Driver, J. W. Feather, P. R. King, and J. B. Dawson, "The optical properties of aqueous suspensions of Intralipid, a fat emulsion," *Phys. Med. Biol.* **34**, 1927–1930 (1989).
34. H. J. Van Staveren, C. J. Moes, J. van Marie, S. A. Prahl, and M. J. Van Gemert, "Light scattering in Intralipid-10% in the wavelength range of 400–1100 nm," *Appl. Opt.* **30**, 4507–4514 (1991).
35. S. T. Flock, S. L. Jacques, B. C. Wilson, W. M. Star, and M. J. van Gemert, "Optical properties of Intralipid: a phantom medium for light propagation studies," *Lasers Surg. Med.* **12**, 510–519 (1992).
36. W. M. Irvine and J. B. Pollack, "Infrared optical properties of water and ice spheres," *Icarus* **8**, 324–360 (1968).
37. M. Shaffer, "Dynamic contrast enhanced photoacoustic computed tomography in MDA-MB-231 and BT-474 xenograft tumor models," Ph.D. thesis (Purdue University, 2012), pp. 54–67.
38. DuPont Titanium Technologies, "Titanium dioxide for coatings," Coatings selection brochure P200067 (2002).
39. <http://www.matweb.com/search/datasheet.aspx?MatGUID=58e86b> [last accessed June 6, 2016].
40. S. E. Clare, "Delivery of nano-tethered therapies to brain metastases of primary breast cancer using a cellular Trojan horse," AD1003801 (U.S. Department of Defense, Defense Technical Information Center, 2015).
41. A. K. Maini, *Lasers and Optoelectronics: Fundamentals, Devices and Applications* (Wiley, 2013).
42. MPE Tables, <https://workspace.imperial.ac.uk/physics/Public/physicsdocs/about/safety/files/MPE-tables.pdf> [last accessed June 14, 2016].

Understanding Resonant Light-Triggered DNA Release from Plasmonic Nanoparticles

Amanda M. Goodman,[†] Nathaniel J. Hogan,[‡] Samuel Gottheim,[†] Carrie Li,[†] Susan E. Clare,[‡] and Naomi J. Halas^{*,†,‡,§,||,⊥}

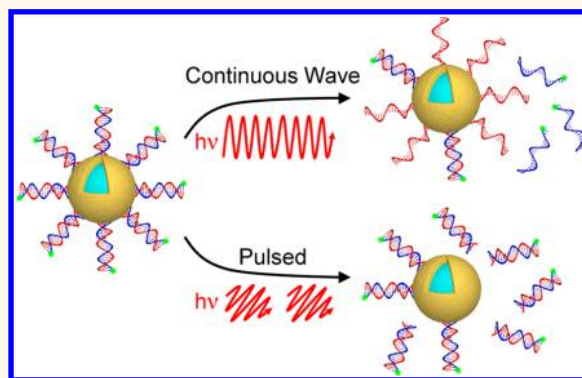
[†]Department of Chemistry, [‡]Department of Electrical and Computer Engineering, [§]Department of Physics and Astronomy, and ^{||}Department of Bioengineering, Rice University, Houston, Texas 77005, United States

[⊥]Department of Surgery, Feinberg School of Medicine, Northwestern University, Chicago, Illinois 60611, United States

S Supporting Information

ABSTRACT: Nanoparticle-based platforms for gene therapy and drug delivery are gaining popularity for cancer treatment. To improve therapeutic selectivity, one important strategy is to remotely trigger the release of a therapeutic cargo from a specially designed gene- or drug-laden near-infrared (NIR) absorbing gold nanoparticle complex with NIR light. While there have been multiple demonstrations of NIR nanoparticle-based release platforms, our understanding of how light-triggered release works in such complexes is still limited. Here, we investigate the specific mechanisms of DNA release from plasmonic nanoparticle complexes using continuous wave (CW) and femtosecond pulsed lasers. We find that the characteristics of nanoparticle-based DNA release vary profoundly from the same nanoparticle complex, depending on the type of laser excitation. CW laser illumination drives the photothermal release of dehybridized single-stranded DNA, while pulsed-laser excitation results in double-stranded DNA release by cleavage of the Au–S bond, with negligible local heating. This dramatic difference in DNA release from the same DNA–nanoparticle complex has very important implications in the development of NIR-triggered gene or drug delivery nanocomplexes.

KEYWORDS: nanoshells, DNA, laser, photothermal heating, oligonucleotide



To treat and prevent disease, light-triggered release using nanoparticle-based complexes has been shown to be a promising strategy for gene therapy^{1–15} and drug delivery.^{16–25} One popular complex consists of thiolated DNA bound to near-infrared (NIR) absorbing gold nanoparticles such as nanoshells, nanorods, or nanocages.^{12–15} Resonant illumination of the gold nanoparticle–DNA complex results in the light-triggered release of DNA from the surface of the nanoparticle.^{7–11} For gene therapy, released DNA, or in some cases RNA, can be used to prevent transcription or translation of messenger RNA (mRNA) or to inhibit protein function.^{7,26} This type of nanoparticle–DNA complex can also be used for drug delivery, where therapeutic molecules can be non-covalently bound to the DNA and released upon resonant illumination.^{23–25} While other nanoparticle platforms have been investigated for drug delivery, including liposomes^{20,27} and hydrogels,^{28,29} as well as polymeric,^{30–32} magnetic,^{33,34} and metallic nanoparticles,²⁵ these nanosystems typically rely upon changes in the intracellular environment such as pH^{32,35–37} and temperature^{29,31,35–37} to induce drug release, which can vary with cell type and location. Externally applied triggers such as

magnetic^{38,39} and electric^{40,41} fields, ultrasound,⁴² and, specifically, light,^{23,43–46} allow for precise spatial and temporal release. Controlled release of chemotherapeutic agents once the particles have been delivered specifically to a tumor site is a potential strategy to reduce the systemic toxicity of traditional chemotherapy treatments.

The experimental conditions employed for light-triggered release schemes vary widely from study to study.^{8–10,12,13,25,47} Many schemes illuminate metallic nanostructures coated in double-stranded DNA (dsDNA) with continuous wave (CW) lasers to dehybridize the dsDNA, resulting in release of single-stranded DNA (ssDNA), while the complementary strand remains tethered to the nanoparticle surface through a gold–thiol bond.^{7,8,23,48,49} Other schemes utilize pulsed (femtosecond, nanosecond, and picosecond) lasers to either dehybridize the dsDNA or break the gold–thiol bond between the DNA molecule and the nanoparticle, which results in

Received: September 27, 2016

Accepted: November 18, 2016

Published: November 18, 2016

release of the entire dsDNA.^{9,10,13,50–54} Two mechanisms have been proposed to explain these release observations: either simple melting of the dsDNA from the increased temperature of the nanoparticles or hot-electron transfer from plasmon decay causing either dehybridization or Au–S bond breaking. To improve control and tailorability of light-triggered DNA release in these systems, it is critical to understand the specific DNA release mechanisms and how they relate to the type of laser illumination used to trigger release.

In this study, we examine the specific mechanisms of NIR light-triggered DNA release from DNA-functionalized plasmonic nanoparticle complexes. Here, we use nanoshells (NS), composed of a silica core surrounded by a thin gold shell, functionalized with partially thiolated dsDNA. NS are strong absorbers of NIR light, are biocompatible, and are easily functionalized.^{55–59} We employ NIR light because it enables deep tissue penetration due to the low absorption of biological tissue in this region,⁶⁰ while high-energy visible or UV photons are strongly absorbed by bulk tissue, which can result in protein and DNA damage.⁶¹ We find that DNA release can be achieved in two distinct regimes: high-power CW illumination and low average power, high-intensity pulsed-laser excitation.

Each regime is controlled by a distinct mechanism that drives the DNA release (Scheme 1). We have observed that DNA

release through hot-electron injection.⁸ Alternatively, we have also investigated femtosecond pulsed-laser-induced release at low (25 mW range) average laser powers. DNA release is found to occur through a hot-electron transfer process, which breaks the Au–S bond, releasing dsDNA. While this mechanism has been demonstrated with high-energy UV pulsed lasers,⁵¹ to our knowledge, no previous work has demonstrated the pulsed release mechanism with NIR light. We carefully monitored the bulk temperature under these conditions and found essentially no bulk temperature increase under illumination. We also found that, for our experimental conditions, the process is also nearly independent of nanoparticle concentration. These results indicate that pulsed-laser-induced release is substantially more favorable for *in vivo* applications than CW release, where it is highly desirable to minimize nonspecific cell death and where local nanoparticle concentrations and distributions are uncontrollable and essentially unknown.

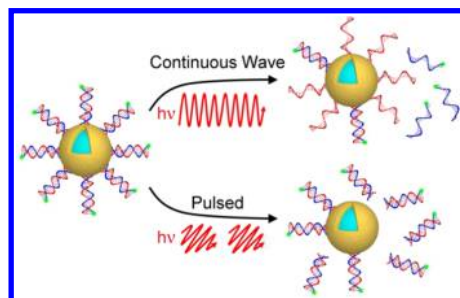
RESULTS AND DISCUSSION

Nanocomplex Synthesis and Characterization. dsDNA was formed by hybridizing a thiolated ssDNA with a nonthiolated fluorescein-tagged ssDNA. The melting temperature of the dsDNA in solution was characterized by circular dichroism (CD). Spectra show a negative peak at 246 nm and a positive peak at 278 nm, characteristic of B-form DNA (Figure S1A).^{62,63} The ellipticity (θ) at 246 nm was monitored as a function of temperature to obtain the dsDNA melting curve (Figure S1B). The first derivative of a Boltzmann fit of the CD curve showed a melting temperature (T_m) of 55.2 ± 0.7 °C, which is close to the theoretically calculated T_m of 51.3 °C in 33 mM NaCl TE buffer.⁶⁴

Nanoshells were synthesized with a 120 nm SiO₂ core and a 21 nm Au shell according to previously reported protocols.^{55,57} The NS@dsDNA nanocomplex was formed by attachment of the dsDNA to the NS surface *via* a gold–thiol bond. Functionalization of the NS surface was verified with extinction spectroscopy, transmission electron microscopy (TEM), and ζ -potential measurements. The bare NS extinction spectrum red-shifted from 775 to 781 nm after dsDNA functionalization, resulting from the change in the dielectric environment around the NS (Figure 1A). TEM images show the formation of a thin layer of DNA around the NS (Figure 1B,C). The ζ -potential decreased from -44.1 ± 0.7 to -59.4 ± 1.7 mV due to the increased negative charges associated with the phosphate backbone of the DNA (Figure 1D).

Thermal and CW Laser-Induced DNA Melting. To investigate the dehybridization temperature when dsDNA is tethered to the NS surface, a thermal release profile at 5 °C

Scheme 1. NIR-Light-Induced DNA Release^a



^aCW irradiation results in dehybridization and release of fluorescently tagged ssDNA, while pulsed irradiation results in Au–S bond breakage and release of dsDNA.

release upon CW illumination is due to a temperature increase arising from the collective heating effects of the nanoparticles, causing dehybridization and release of ssDNA. This limits the use of CW illumination *in vivo* because the high temperatures are likely to result in nonspecific cell death and also because it is highly concentration-dependent. Our findings clarify previous work, which postulated that CW illumination could drive

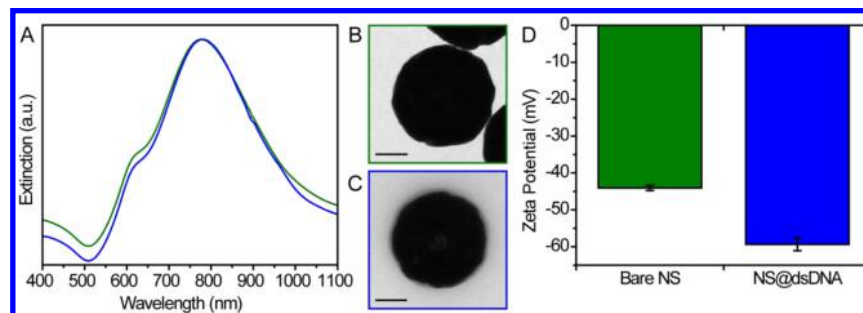


Figure 1. Nanocomplex characterization. (A) Extinction spectra of bare NS (green) and NS@dsDNA (blue), TEM images of (B) bare NS and (C) NS@dsDNA, and (D) ζ -potential of bare NS (green) and NS@dsDNA (blue). Scale bars are 50 nm.

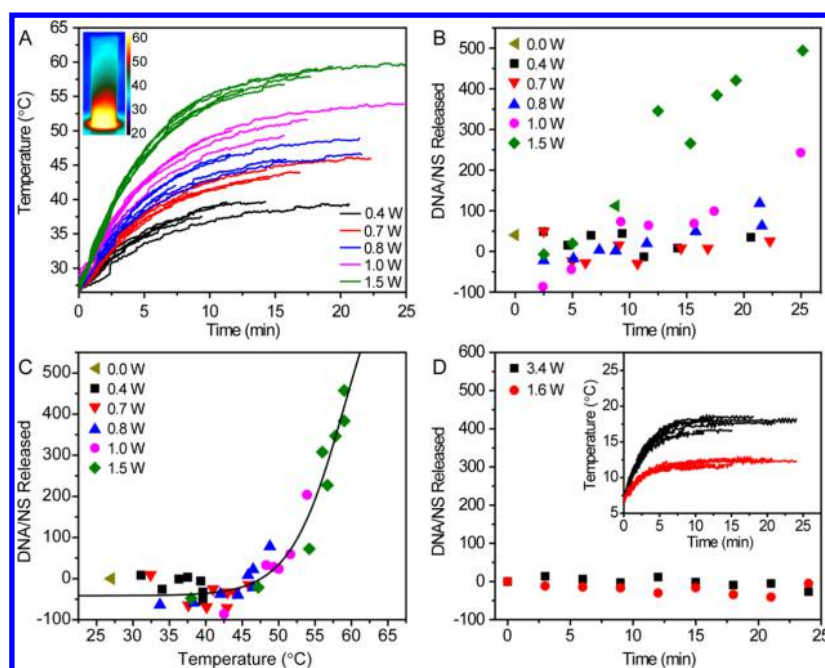


Figure 2. Investigation of CW-induced DNA release mechanism. (A) Heating profile of DNA release from solutions heated *via* a CW laser at various laser powers. Inset: Thermal image of DNA release experiment at 1.5 W. DNA release profile plotted as a function of (B) time and (C) temperature. A Boltzmann fit estimates a melting temperature of 59.1 ± 4.5 °C. (D) DNA release from solutions in a cuvette stage set to 4 °C under 1.6 (red) and 3.4 W (black) laser irradiation showing no DNA release. Inset: Corresponding heating profile showing that the solution temperature does not exceed room temperature.

increments was acquired. The nanoparticle concentration used was 1×10^9 NS/mL, a concentration range similar to the local concentration of nanoparticles in tumors (10^8 – 10^9 particles/mL).^{65,66} The NS@dsDNA solution was heated in a temperature-controlled stage. After 20 min of equilibration at each chosen temperature, an aliquot was removed and centrifuged. A fresh sample was used for each temperature point. A fluorescein tag on the nonthiolated strand was used for quantification of the released ssDNA. The fluorescence intensity of the supernatant was measured, and these data were used to obtain the amount of ssDNA released from NS using a linear standard curve (Figure S2A). The ssDNA/NS released *versus* temperature was found to follow a Boltzmann response; the DNA melting temperature achieved by heating the samples was 61.1 ± 2.3 °C (Figure S2B). The slightly higher T_m from thermal release compared well to the T_m of 55.2 ± 0.7 °C observed in CD, where the difference can be attributed to the dsDNA being anchored to the NS surface *versus* free dsDNA in solution obtained from the CD measurements. The binding of the DNA to the nanoparticle results in increased steric hindrance and a difference in local salt concentration relative to DNA in solution; these differences in local environment are sufficient to alter the temperature between those two regimes, consistent with our observations.⁶⁷

We then compared the thermal release of DNA from the NS to NIR release induced by an 808 nm wavelength CW laser. The NS@dsDNA solution was irradiated at 0.4, 0.7, 0.8, 1.0, and 1.5 W for times ranging from 1.5 to 25 min. During irradiation, the sample temperature was monitored with a thermal camera (Figure 2A, inset). When plotted as a function of time, no substantial release was observed except at laser power levels of 1.5 W, which resulted in the bulk solution temperature reaching the DNA dehybridization temperature (Figure 2B). When plotted as a function of temperature, the

CW laser-induced DNA release profile is consistent with the thermal release profile with a T_m of 59.1 ± 4.5 °C (Figure 2C).

Unlike previous reports, we observed no increased DNA release below the dehybridization temperature under CW irradiation. It is likely that this discrepancy may be due to the lower 10^9 NS/mL nanoparticle concentration used in our study, compared to higher 10^{10} NS/mL concentrations used in the other studies, where lower-temperature DNA release was reported.^{7,8,15,23} An earlier study reported by our group on collective photothermal heating by plasmonic nanoparticles showed that particle concentrations of 10^{10} NS/mL result in light absorption profiles with a decay length of around 300 μm along the laser propagation direction. It was also shown that, at these high particle concentrations, where the scattering mean free path is ~ 830 μm , multiple scattering of photons significantly increases the fraction of incident light absorbed. These two factors, the small heating volume and the enhanced absorption efficiency due to multiple scattering, result in large temperature increases and gradients at the input laser powers studied.⁶⁸ These temperature gradients can explain the previously observed release of ssDNA below the dehybridization temperature, where the temperature was probed at the bottom of the temperature gradient, not in the region of incident light. The results we report here clearly show that one must consider the full temperature profile of the absorbing medium, which may quite possibly be significantly nonuniform, in regions of high nanoparticle concentration.⁶⁸

The similarity of the CW laser-induced DNA release profile to the thermal profile, as well as the apparent dependency on nanoparticle concentration, suggests that thermal effects play a dominant role in DNA dehybridization, but they do not unambiguously separate thermal and nonthermal release mechanisms, such as hot-electron effects.^{10,69}

We performed a similar set of CW light-triggered release studies, this time keeping the entire sample below the DNA melting temperature by using a thermoelectric (Peltier effect) stage. The NS@dsDNA solution was cooled to 7 °C and illuminated from the side with an 808 nm CW laser at 1.6 and 3.4 W for durations of 3–24 min. A fresh sample was used for each time point. The temperature of the entire sample was maintained below 20 °C for all experiments (Figure 2D, inset). No release was observed for either laser power, indicating that nonthermal effects such as non-equilibrium charge transfer do not play a measurable role in release (Figure 2D). A significant fraction of hot electrons from plasmon decay should have energies equivalent to the photon energy (1.53 eV), which is 3 orders of magnitude higher than the energy required for dehybridization, $k_b(T_m - 298.15\text{ K}) \sim 3\text{ meV}$, that is, the thermal energy difference between the dehybridization temperature and room temperature. Even with cooling the stage to 7 °C, the energy requirement for dehybridization is only 4.6 meV, which is still an insignificant fraction of the energy of the hot electrons. Therefore, the absence of release when the entire sample is maintained below room temperature supports that thermal effects drive the DNA dehybridization.

Pulsed-Laser-Induced Release. The DNA release observed in the CW laser experiments provides strong evidence that the release mechanism is thermal in nature and requires significant heating to dehybridize DNA. However, it would be far more preferable to reduce or eliminate this heating requirement to avoid nonspecific damage to surrounding tissues during DNA release *in vivo*. The combination of high pulse energies and low average powers achievable with pulsed lasers is a drastically different illumination regime, capable of generating non-equilibrium heating effects local to the nanoparticle with minimal heating of the surrounding volume. Previous studies of pulsed-laser-induced DNA release have used high-energy UV lasers to break the Au–S bond⁵¹ or large powers in the NIR to melt the particles in order to release DNA.^{13,70,71} Here, we investigate the DNA release mechanism for these NIR resonant nanoshell-based complexes using pulsed NIR illumination.

NS@dsDNA solutions were irradiated for 10 min with a ~160 fs 800 nm wavelength pulsed laser at powers from 2 to 50 mW (Figure 3A). DNA release increased linearly from 2 to 25 mW. However, during experimentation, we observed above 25 mW there was color change in the solution indicating a loss of nanoshell integrity (blue shaded region). We performed experiments in triplicate up to this likely damage threshold, after which we performed one experiment at each laser power to verify *via* scanning electron microscopy (SEM) imaging the breakdown of nanoshell integrity. The linear power dependence from 2 to 25 mW, which differs distinctively from the thermal release profiles in the CW case, indicates that the DNA release under these pulsed excitation conditions is not likely due to a thermal process. In fact, no temperature increase of the solution was observed (Figure 3B).

The expected transient temperature rise of the DNA due to pulsed irradiation at these power levels is, in principle, sufficient to dehybridize the DNA. To understand the temperature experienced by the DNA during illumination, we employed finite-element method (FEM, Comsol; see Supporting Information) to calculate the spatial and temporal dependence of the temperature field of a single nanoparticle in aqueous solution. We employed both spatial and temporal averages to obtain average temperatures (Figure S3). Averaging the

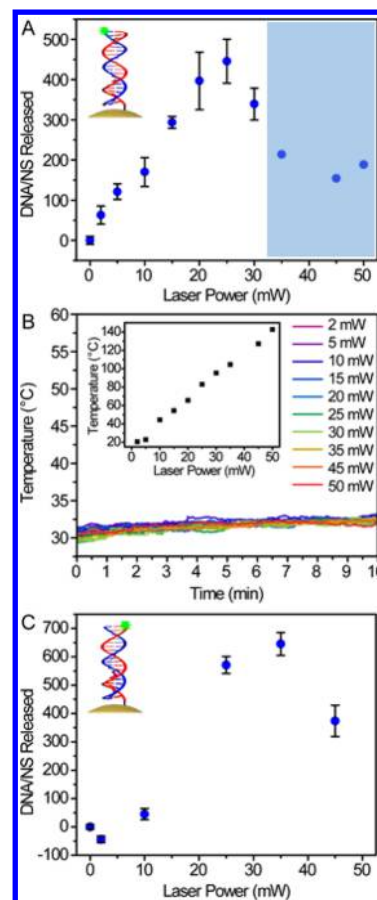


Figure 3. Femtosecond pulsed-laser-induced ssDNA release. (A) DNA release profile where the nonthiolated DNA strands are fluorescently tagged, showing linear release up to 25 mW, after which release decreases. (B) Heating profile of femtosecond pulsed-laser DNA release at laser powers from 2 to 50 mW showing no bulk solution temperature increase. Inset: Finite-element method simulation of the maximum temperature in a 6.6 nm layer around the NS. (C) DNA release profile of the control where the thiolated DNA strands are fluorescently tagged, showing the same release profile as (A), indicating Au–S bond breakage-mediated DNA release.

temperature in a shell around the nanoparticle with dimensions corresponding to the length of the dsDNA (6.6 nm) gives average temperatures ranging from essentially room temperature at 2 mW to nominally 140 °C at 50 mW (Figure 3B, inset). For laser powers where considerable release is observed (10–25 mW), the calculated temperatures fall between 45 and 80 °C, which is consistent with the T_m results from both the thermal and CW laser experiments.

To investigate the nature of the DNA release under pulsed-laser excitation, we used dsDNA with a fluorescein tag on the thiolated DNA strand. With the thiolated strand tagged with a fluorophore, if thermal or CW DNA dehybridization occurs, no fluorophore will be released into solution. However, for pulsed-laser illumination conditions, substantial fluorescence was observed with a release profile very similar to that shown in Figure 3A, increasing linearly with increasing laser power up to 35 mW (Figure 3C). Because the binding energy of the Au–S bond has been shown to be ~0.1 eV in such systems, the increased local temperature at the nanoparticle surface alone is insufficient to induce this bond breakage.⁵¹ Temperatures in excess of 890 °C ($k_b T = 0.1\text{ eV}$) would be required to thermally

break this bond, a temperature regime where nanoparticle melting and reshaping would also be expected to occur. These results strongly suggest that a nonthermal mechanism, such as non-equilibrium charge transfer of hot carriers from the metal to the DNA molecule, may induce breakage of the Au–S bond, resulting in release of the intact hybridized dsDNA molecules.

The large pulse energies generated by the femtosecond laser at the highest power levels used in these experiments can considerably increase the nanoparticle temperature such that nanoparticle reshaping occurs. Irreversible nanoparticle reshaping is the reason for the decrease in DNA release observed above 25 mW of pulsed irradiation, a conclusion supported by extinction spectroscopy and SEM of the nanoparticles before and after laser irradiation. The extinction spectra of samples irradiated at 0–25 mW display a dipole peak centered at ~ 785 nm and a well-defined higher-energy quadrupole peak at ~ 600 nm. From 30 to 50 mW, the extinction maximum red shifts to 688 nm, accompanied by the disappearance of the quadrupole plasmon peak and the appearance of a second peak at ~ 1015 nm (Figure 4A). These changes indicate loss of shell integrity

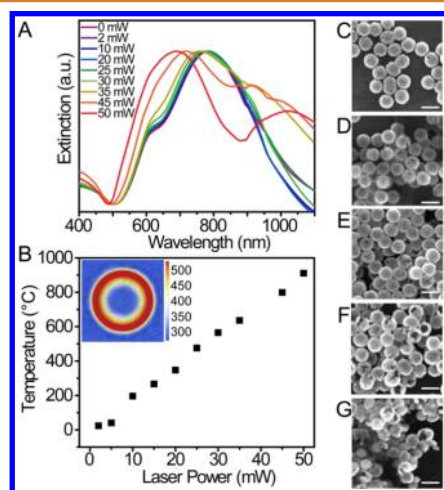


Figure 4. Nanoparticle characterization after pulsed-laser-induced DNA release. (A) Extinction spectroscopy showing a red shift in the plasmon resonance at powers above 25 mW. (B) FEM simulation of the average temperature of the Au shell after a single 150 fs laser pulse. Inset: Temperature map for 25 mW incident power 100 ps after laser pulse (scale in °C). SEM images after laser irradiation at (C) 2, (D) 25, (E) 30, (F) 35, and (G) 50 mW showing particle degradation above 25 mW. Scale bars are 200 nm.

and particle aggregation. SEM images show no change in the Au shells from 2 to 25 mW but reveal an increase in holes and cracks in the shells at 30 and 35 mW, with widespread holes in the shell at 50 mW (Figure 4C–G). These results agree well with previously reported reshaping of nanoshells under femtosecond pulsed irradiation.⁷² The fact that there is considerable DNA release in the range from 2 to 25 mW accompanied by the lack of Au shell breakdown suggests that the release is not due to reshaping or fragmentation of the Au.

FEM calculations also support the observation of Au NS reshaping and reduced DNA release for incident laser power levels at and above 30 mW. The average local temperature increase of the NS as a function of incident laser power is shown in Figure 4B. At the highest power of 50 mW, the Au shell reaches calculated temperatures around 1000 °C, close to the 1064 °C melting point of bulk Au. It is well-known that at the nanoscale the energy densities required for surface

reshaping are a fraction of the bulk melting energy density.⁷³ Our calculations show that, at 30 mW, the Au shell reaches a maximum temperature of ~ 550 °C, which appears to correspond to the onset of nanoscale reshaping for this structure. Over the range of laser powers used in our experiments, the Au is reaching between 3 and 70% of the bulk melting energy density of 195 J/g (Figure S4), with the onset of reshaping occurring at $\sim 40\%$, the same value obtained for reshaping of Au nanorods.⁷³ These values will vary depending on nanoparticle morphology and composition as well as temporal pulse width.

Time and Concentration Dependence of DNA Release. Using 25 mW of pulsed irradiation, the time to release the maximum DNA was investigated (Figure 5A).

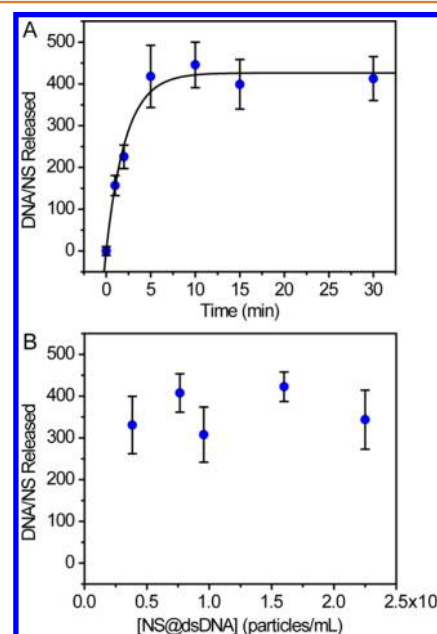


Figure 5. Time and concentration dependence of pulsed-laser-induced DNA release. Variation of release as a function of (A) irradiation time at 25 mW with 1×10^9 particles/mL fit with an exponential that reveals a time constant of 2.2 min and (B) concentration of NS@dsDNA irradiated at 25 mW and 10 min irradiation showing no appreciable change in release at different concentrations.

Approximately 40% of release occurs after 2 min of irradiation with saturation achieved after only 5 min. Achieving substantial DNA release over short irradiation times with low average powers indicates that short pulse-induced DNA release is a highly attractive strategy for therapeutic applications.

Nanoparticle uptake in tumors is known to vary widely,⁷⁴ indicating the desirability for a release method that is insensitive to nanoparticle concentration. For pulsed-laser illumination periods of less than 10 min at 25 mW, no appreciable change in the amount of DNA released per NS was observed as nanoparticle concentration was increased (Figure 5B). The relatively low average power of the laser results in negligible bulk heating. Thus, DNA release induced by ultrafast irradiation differs dramatically from CW-induced release, which depends on collective nanoparticle heating. If ultrafast induced release arises from hot carrier transfer, it should depend only on the independent interaction of each nanoparticle with the incident light field. Therefore, the magnitude

of release per nanoparticle is relatively insensitive to concentration. At high concentrations, some dependence is expected due to the attenuation of the incident laser beam; however, as our experiments illustrate, this effect is not relevant over the range of nanoparticle concentrations relevant for *in vivo* therapeutic applications.

CONCLUSION

In this study, we showed that NIR CW light-triggered DNA release is the result of thermally induced DNA dehybridization, which induces release of ssDNA. Collective heating effects characteristic of CW irradiation at the NS concentrations relevant for therapy make the DNA release highly dependent on nanoparticle concentration. At the low particle concentrations achievable in tumors, we demonstrated that the global temperature must rise above the DNA dehybridization temperature to cause DNA release. In contrast, we observed that a NIR ultrafast pulsed laser induces release of dsDNA with no measurable bulk temperature increase at lower nanoparticle concentrations. For pulsed-laser illumination, the DNA is released by inducing Au–S bond breakage. With a pulsed laser, DNA release is a single-particle phenomenon and is independent of particle concentration. These results clearly show that pulsed-laser-induced DNA release is a highly promising strategy for light-triggered therapeutic release without inducing bulk heating, making this approach more likely to preserve the integrity of healthy tissues in therapeutic applications *in vivo*.

EXPERIMENTAL METHODS

Materials. Potassium carbonate anhydrous was purchased from Fisher Scientific. Hydrogen tetrachloroaurate(III) trihydrate ($\text{HAuCl}_4 \cdot 3\text{H}_2\text{O}$), DL-dithiothreitol (DTT), and sodium chloride were purchased from Sigma-Aldrich. Aminated silica cores (120 nm diameter) in ethanol (40 mg/mL) were purchased from nanoComposix, Inc., San Diego, CA. HPLC-purified DNA strands and 10 mM Tris, pH 7.5, 0.1 mM EDTA buffer (1× TE buffer), were purchased from Integrated DNA Technologies. Water was deionized and filtered by a Milli-Q water system (18.2 M Ω -cm at 25 °C, Millipore).

DNA Purification. Prior to nanoshell functionalization, thiolated ssDNA [$\text{HS-C}_6\text{H}_{12}\text{-TATGATCTGTACAGCTTGA}$] was incubated with 10 mM DTT reducing agent in 10 mM TE buffer for 1 h at room temperature. The thiolated DNA was purified with a Sephadex G-25 column (NAP 25, GE Healthcare), eluting with TE buffer. The complementary fluorescein-tagged ssDNA [ATACTAGACAGT-GTCGAAGT-Fluor] was dispersed in 600 μL of TE buffer. DNA concentration of both strands was determined by measuring their absorbance at 260 nm. The two DNA strands were mixed in a 1:1 molar ratio with 33 mM NaCl and boiled for 4 min. The mixture was cooled slowly overnight to hybridize the strands.

Nanoshell Synthesis and Functionalization. Nanoshells were synthesized by previously published procedures with 120 nm diameter SiO_2 cores and 21 nm thick Au shells.^{55,57} The nanoshell surface was functionalized by mixing dsDNA with bare NS in a ratio of 20000 dsDNA strands/NS and stirred overnight. The particles were washed three times by centrifugation and redispersed in TE buffer, pH 7.5. Extinction spectra were obtained using a Cary 5000 UV/vis/NIR Varian spectrophotometer. ζ -Potential measurements were taken with a Malvern Zetasizer Nano ZS. TEM images were obtained on a JEOL 1230 high-contrast transmission electron microscope.

Circular Dichroism Measurements. CD spectra of 5 μM dsDNA in 33 μM NaCl TE buffer (pH 7.5) were acquired in a 1 cm path length quartz cell. Measurements were made using a JASCO J-810 spectropolarimeter equipped with a Peltier-type temperature control system at wavelengths from 200 to 320 nm. Thermal dsDNA dehybridization curves were obtained by monitoring the decrease in

ellipticity with temperature in the desired wavelength range. The temperature was varied between 25 and 90 °C in 5 °C increments with an equilibration time of 180 s. The melting CD spectra of dsDNA, which show structural transitions from the double-strand state to the single-strand state, are shown in Figure S1B. The melting curve was extracted from the change in ellipticity at 246 nm (θ_{246}), and the first derivative of a Boltzmann fit determined the T_m to be 55.2 ± 0.7 °C (Figure S1B).

Thermal Studies. While being stirred, 1 mL of 1×10^9 particles/mL NS@dsDNA was heated to the desired temperature in a $1 \times 1 \times 4$ cm methacrylate cuvette using a Peltier temperature-controlled cuvette stage. After 20 min of heating, a 300 μL aliquot was removed and immediately centrifuged at 5000g for 2 min at 6 °C to separate the released ssDNA from the particles. The process was repeated in 5 °C increments up to 65 °C. A fresh sample was used for each temperature point. Released ssDNA in the supernatant was quantified by fluorescence.

Temperature-Controlled CW Laser Release Studies. NS@dsDNA (2.5 mL of 1×10^9 particles/mL) was cooled to 7 °C using a Peltier temperature-controlled cuvette stage. While being cooled and stirred, the NS@dsDNA solution was irradiated with an 808 nm CW diode laser (Diomed, 15Plus, Angio Dynamics) at 1.6 and 3.4 W with a full width at half-maximum of 3.5 mm. The sample was irradiated from the side to minimize vaporization. Temperature was monitored with an infrared thermocouple (Omega OS-801-MT-K) with a 0.5 cm spot size. After the desired time, a 300 μL aliquot was removed and immediately centrifuged at 5000g for 2 min at 6 °C. A fresh sample was used for each time point. Fluorescence measurements were taken on the supernatant to quantify released ssDNA.

Non-temperature-Controlled CW Laser Release Studies. NS@dsDNA (1 mL of 1×10^9 particles/mL) was stirred on a custom-built plastic cuvette stage. NS@dsDNA solutions were irradiated from the side with the CW laser at 0.4, 0.7, 0.8, 1.0, and 1.5 W/cm². For each laser power, the saturation temperature was determined, and samples were then irradiated for 0, 2.5, 5, 7.5, 10, and 15 min after the saturation temperature was achieved. Samples were also taken 2.5 and 5 min after the laser was turned on, before the saturation temperature was reached. Temperature was monitored with a thermal camera (FLIR A5). After irradiation, a 300 μL aliquot was removed and immediately centrifuged at 5000g for 2 min at 6 °C. Spatial and temporal average temperatures were used as the temperature value in the analysis. Fluorescence was measured in the supernatant of all samples.

Femtosecond Pulsed-Laser Release Studies. NS@dsDNA (1 mL of 1×10^9 particles/mL) was stirred on a cuvette stage and irradiated from the side with a Ti:sapphire laser amplifier (Coherent, RegA) operating at 250 kHz with an average power of 1 W and a pulse length of ~ 150 –180 fs. The laser spot had a full width at half-maximum of 44 μm . Temperature was monitored with a thermal camera (FLIR A5). Samples were irradiated for 10 min at 2–50 mW. After irradiation, a 300 μL aliquot was removed and immediately centrifuged at 3000g for 3 min. Fluorescence measurements were taken of the supernatants. SEM images were taken of the particles before and after release (FEI Quanta 650, accelerating voltage of 25 kV).

ASSOCIATED CONTENT

Supporting Information

The Supporting Information is available free of charge on the ACS Publications website at DOI: 10.1021/acsnano.6b06510.

DNA melting temperature characterization by circular dichroism (Figure S1); DNA release profile as a function of temperature from solutions heated *via* a temperature-controlled cuvette stage (Figure S2); detailed description of FEM simulations; FEM simulation results of spatially averaged temperature as a function of time (Figure S3); and approximate energy density in the Au shell as a function of laser power (Figure S4) (PDF)

AUTHOR INFORMATION

Corresponding Author

*E-mail: halas@rice.edu.

ORCID

Naomi J. Halas: 0000-0002-8461-8494

Notes

The authors declare no competing financial interest.

ACKNOWLEDGMENTS

This work was financially supported by the Robert A. Welch Foundation (C-1220), CDMRP grant (W81 XWH-13-1-0341), AFOSR MURI grant (FA 9550-15-1-0022), and the National Science Foundation Graduate Research Fellowship under Grant No. 0940902. We thank O. Neumann and L. Zhou for helpful discussion and editing.

REFERENCES

- (1) Han, G.; You, C.-C.; Kim, B.-J.; Turingan, R. S.; Forbes, N. S.; Martin, C. T.; Rotello, V. M. Light-Regulated Release of DNA and Its Delivery to Nuclei by Means of Photolabile Gold Nanoparticles. *Angew. Chem.* **2006**, *118*, 3237–3241.
- (2) Brown, P. K.; Qureshi, A. T.; Moll, A. N.; Hayes, D. J.; Monroe, W. T. Silver Nanoscale Antisense Drug Delivery System for Photoactivated Gene Silencing. *ACS Nano* **2013**, *7*, 2948–2959.
- (3) Knipe, J. M.; Peters, J. T.; Peppas, N. A. Theranostic Agents for Intracellular Gene Delivery with Spatiotemporal Imaging. *Nano Today* **2013**, *8*, 21–38.
- (4) Yang, X.; Liu, X.; Liu, Z.; Pu, F.; Ren, J.; Qu, X. Near-Infrared Light-Triggered, Targeted Drug Delivery to Cancer Cells by Aptamer Gated Nanovehicles. *Adv. Mater.* **2012**, *24*, 2890–2895.
- (5) Zheng, J.; Nie, Y.; Yang, S.; Xiao, Y.; Li, J.; Li, Y.; Yang, R. Remote-Controlled Release of DNA in Living Cells via Simultaneous Light and Host-Guest Mediations. *Anal. Chem.* **2014**, *86*, 10208–10214.
- (6) Huang, X.; Pallaoro, A.; Braun, G. B.; Morales, D. P.; Ognyankin, M. O.; Zasadzinski, J.; Reich, N. O. Modular Plasmonic Nanocarriers for Efficient and Targeted Delivery of Cancer-Therapeutic siRNA. *Nano Lett.* **2014**, *14*, 2046–2051.
- (7) Barhoumi, A.; Huschka, R.; Bardhan, R.; Knight, M. W.; Halas, N. J. Light-Induced Release of DNA from Plasmon-Resonant Nanoparticles: Towards Light-Controlled Gene Therapy. *Chem. Phys. Lett.* **2009**, *482*, 171–179.
- (8) Huschka, R.; Zuloaga, J.; Knight, M. W.; Brown, L. V.; Nordlander, P.; Halas, N. J. Light-Induced Release of DNA from Gold Nanoparticles: Nanoshells and Nanorods. *J. Am. Chem. Soc.* **2011**, *133*, 12247–12255.
- (9) Asanuma, H.; Jiang, Z.; Ikeda, K.; Uosaki, K.; Yu, H.-Z. Selective Dehybridization of DNA-Au Nanoconjugates Using Laser Irradiation. *Phys. Chem. Chem. Phys.* **2013**, *15*, 15995–16000.
- (10) Thibaudau, F. Ultrafast Photothermal Release of DNA from Gold Nanoparticles. *J. Phys. Chem. Lett.* **2012**, *3*, 902–907.
- (11) Fukushima, H.; Yamashita, S.; Mori, T.; Katayama, Y.; Niidome, T. Sequential Release of Single-Stranded DNAs from Gold Nanorods Triggered by Near-Infrared Light Irradiation. *Chem. Lett.* **2012**, *41*, 711–712.
- (12) Jones, M. R.; Millstone, J. E.; Giljohann, D. A.; Seferos, D. S.; Young, K. L.; Mirkin, C. A. Plasmonically Controlled Nucleic Acid Dehybridization with Gold Nanoprisms. *ChemPhysChem* **2009**, *10*, 1461–1465.
- (13) Wijaya, A.; Schaffer, S. B.; Pallares, I. G.; Hamad-Schifferli, K. Selective Release of Multiple DNA Oligonucleotides from Gold Nanorods. *ACS Nano* **2009**, *3*, 80–86.
- (14) Yamashita, S.; Fukushima, H.; Akiyama, Y.; Niidome, Y.; Mori, T.; Katayama, Y.; Niidome, T. Controlled-Release System of Single-Stranded DNA Triggered by the Photothermal Effect of Gold Nanorods and Its in Vivo Application. *Bioorg. Med. Chem.* **2011**, *19*, 2130–2135.
- (15) Huschka, R.; Barhoumi, A.; Liu, Q.; Roth, J. A.; Ji, L.; Halas, N. J. Gene Silencing by Gold Nanoshell-Mediated Delivery and Laser-Triggered Release of Antisense Oligonucleotide and siRNA. *ACS Nano* **2012**, *6*, 7681–7691.
- (16) Tan, X.; Li, B. B.; Lu, X.; Jia, F.; Santori, C.; Menon, P.; Li, H.; Zhang, B.; Zhao, J. J.; Zhang, K. Light-Triggered, Self-Immulative Nucleic Acid-Drug Nanostructures. *J. Am. Chem. Soc.* **2015**, *137*, 6112–6115.
- (17) Song, J.; Hwang, S.; Im, K.; Hur, J.; Nam, J.; Hwang, S.; Ahn, G.-O.; Kim, S.; Park, N. Light-Responsive DNA Hydrogel–Gold Nanoparticle Assembly for Synergistic Cancer Therapy. *J. Mater. Chem. B* **2015**, *3*, 1537–1543.
- (18) Wen, Y.; Xu, L.; Wang, W.; Wang, D.; Du, H.; Zhang, X. Highly Efficient Remote Controlled Release System Based on Light-Driven DNA Nanomachine Functionalized Mesoporous Silica. *Nanoscale* **2012**, *4*, 4473–4476.
- (19) Kah, J. C. Y.; Chen, J.; Zubietta, A.; Hamad-Schifferli, K. Exploiting the Protein Corona around Gold Nanorods for Loading and Triggered Release. *ACS Nano* **2012**, *6*, 6730–6740.
- (20) Luo, D.; Carter, K. A.; Razi, A.; Geng, J.; Shao, S.; Giraldo, D.; Sunar, U.; Ortega, J.; Lovell, J. F. Doxorubicin Encapsulated in Stealth Liposomes Conferred with Light-Triggered Drug Release. *Biomaterials* **2016**, *75*, 193–202.
- (21) Li, N.; Yu, Z.; Pan, W.; Han, Y.; Zhang, T.; Tang, B. A Near-Infrared Light-Triggered Nanocarrier with Reversible DNA Valves for Intracellular Controlled Release. *Adv. Funct. Mater.* **2013**, *23*, 2255–2262.
- (22) Liu, J.; Detrembleur, C.; Mornet, S.; Jérôme, C.; Duguet, E. Design of Hybrid Nanovehicles for Remotely Triggered Drug Release: An Overview. *J. Mater. Chem. B* **2015**, *3*, 6117–6147.
- (23) Hushka, R.; Neumann, O.; Barhoumi, A.; Halas, N. J. Visualizing Light-Triggered Release of Molecules Inside Living Cells. *Nano Lett.* **2010**, *10*, 4117–4122.
- (24) Alexander, C. M.; Maye, M. M.; Dabrowiak, J. C. DNA-Capped Nanoparticles Designed for Doxorubicin Drug Delivery. *Chem. Commun. (Cambridge, U. K.)* **2011**, *47*, 3418–3420.
- (25) Luo, Y.-L.; Shiao, Y.-S.; Huang, Y.-F. Release of Photoactivatable Drugs from Plasmonic Nanoparticles for Targeted Cancer Therapy. *ACS Nano* **2011**, *5*, 7796–7804.
- (26) Juliano, R. L.; Ming, X.; Nakagawa, O. The Chemistry and Biology of Oligonucleotide Conjugates. *Acc. Chem. Res.* **2012**, *45*, 1067–1076.
- (27) Schroeder, A.; Heller, D. A.; Winslow, M. M.; Dahlman, J. E.; Pratt, G. W.; Langer, R.; Jacks, T.; Anderson, D. G. Treating Metastatic Cancer with Nanotechnology. *Nat. Rev. Cancer* **2012**, *12*, 39–50.
- (28) Chung, H. J.; Park, T. G. Self-Assembled and Nanostructured Hydrogels for Drug Delivery and Tissue Engineering. *Nano Today* **2009**, *4*, 429–437.
- (29) Klouda, L.; Mikos, A. G. Thermoresponsive Hydrogels in Biomedical Applications. *Eur. J. Pharm. Biopharm.* **2008**, *68*, 34–45.
- (30) Movassaghian, S.; Merkel, O. M.; Torchilin, V. P. Applications of Polymer Micelles for Imaging and Drug Delivery. *Wiley Interdiscip. Rev.: Nanomed. Nanobiotechnol.* **2015**, *7*, 691–707.
- (31) Chilkoti, A.; Dreher, M. R.; Meyer, D. E.; Raucher, D. Targeted Drug Delivery by Thermally Responsive Polymers. *Adv. Drug Delivery Rev.* **2002**, *54*, 613–630.
- (32) Gao, W.; Chan, J. M.; Farokhzad, O. C. pH-Responsive Nanoparticles for Drug Delivery. *Mol. Pharmaceutics* **2010**, *7*, 1913–1920.
- (33) Zhang, W.; Zheng, X.; Shen, S.; Wang, X. Doxorubicin-Loaded Magnetic Nanoparticle Clusters for Chemo-Photothermal Treatment of the Prostate Cancer Cell Line PC3. *Biochem. Biophys. Res. Commun.* **2015**, *466*, 278–282.
- (34) Ernsting, M. J.; Foltz, W. D.; Undzys, E.; Tagami, T.; Li, S.-D. Tumor-Targeted Drug Delivery Using MR-Contrasted Docetaxel –

Carboxymethylcellulose Nanoparticles. *Biomaterials* **2012**, *33*, 3931–3941.

(35) Nitta, S.; Numata, K. Biopolymer-Based Nanoparticles for Drug/Gene Delivery and Tissue Engineering. *Int. J. Mol. Sci.* **2013**, *14*, 1629–1654.

(36) Das, M.; Zhang, H.; Kumacheva, E. Microgels: Old Materials with New Applications. *Annu. Rev. Mater. Res.* **2006**, *36*, 117–142.

(37) Hoare, T.; Pelton, R. Highly pH and Temperature Responsive Microgels Functionalized with Vinylacetic Acid. *Macromolecules (Washington, DC, U. S.)* **2004**, *37*, 2544–2550.

(38) Alexiou, C.; Arnold, W.; Klein, R. J.; Parak, F. G.; Hulin, P.; Bergemann, C.; Erhardt, W.; Wagenpfel, S.; Lubbe, A. S. Locoregional Cancer Treatment with Magnetic Drug Targeting. *Cancer Res.* **2000**, *60*, 6641–6648.

(39) Hayashi, K.; Ono, K.; Suzuki, H.; Sawada, M.; Moriya, M.; Sakamoto, W.; Yogo, T. High-Frequency, Magnetic-Field-Responsive Drug Release from Magnetic Nanoparticle/Organic Hybrid Based on Hyperthermic Effect. *ACS Appl. Mater. Interfaces* **2010**, *2*, 1903–1911.

(40) Ge, J.; Neofytou, E.; Cahill, T. J.; Beygui, R. E.; Zare, R. N. Drug Release from Electric-Field-Responsive Nanoparticles. *ACS Nano* **2012**, *6*, 227–233.

(41) Zhu, Y.; Liu, H.; Li, F.; Ruan, Q.; Wang, H.; Fujiwara, M.; Wang, L.; Lu, G. Q. Max). Dipolar Molecules as Impellers Achieving Electric-Field-Stimulated Release. *J. Am. Chem. Soc.* **2010**, *132*, 1450–1451.

(42) Pitt, W. G.; Hussein, G. A.; Staples, B. J. Ultrasonic Drug Delivery – a General Review. *Expert Opin. Drug Delivery* **2004**, *1*, 37–56.

(43) Bariana, M.; Aw, M. S.; Moore, E.; Voelcker, N. H.; Losic, D. Radiofrequency-Triggered Release for on-Demand Delivery of Therapeutics from Titania Nanotube Drug-Eluting Implants. *Nanomedicine* **2014**, *9*, 1263–1275.

(44) Peiris, P. M.; Bauer, L.; Toy, R.; Tran, E.; Pansky, J.; Doolittle, E.; Schmidt, E.; Hayden, E.; Mayer, A.; Keri, R. A.; Griswold, M. A.; Karathanasis, E. Enhanced Delivery of Chemotherapy to Tumors Using a Multicomponent Nanochain with Radio-Frequency-Tunable Drug Release. *ACS Nano* **2012**, *6*, 4157–4168.

(45) Kim, H.; Chung, K.; Lee, S.; Kim, D. H.; Lee, H. Near-Infrared Light-Responsive Nanomaterials for Cancer Theranostics. *Wiley Interdiscip. Rev.: Nanomed. Nanobiotechnol* **2016**, *8*, 23–45.

(46) Ma, Y.; Liang, X.; Tong, S.; Bao, G.; Ren, Q.; Dai, Z. Gold Nanoshell Nanomicelles for Potential Magnetic Resonance Imaging, Light-Triggered Drug Release, and Photothermal Therapy. *Adv. Funct. Mater.* **2013**, *23*, 815–822.

(47) Jain, P. K.; El-Sayed, M. A. Plasmonic Coupling in Noble Metal Nanostructures. *Chem. Phys. Lett.* **2010**, *487*, 153–164.

(48) Reismann, M.; Bretschneider, J. C.; von Plessen, G.; Simon, U. Reversible Photothermal Melting of DNA in DNA-Gold-Nanoparticle Networks. *Small* **2008**, *4*, 607–610.

(49) Buchkremer, A.; Linn, M. J.; Reismann, M.; Eckert, T.; Witten, K. G.; Richtering, W.; von Plessen, G.; Simon, U. Stepwise Thermal and Photothermal Dissociation of a Hierarchical Superaggregate of DNA-Functionalized Gold Nanoparticles. *Small* **2011**, *7*, 1397–1402.

(50) Poon, L.; Zandberg, W.; Hsiao, D.; Erno, Z.; Sen, D.; Gates, B. D.; Branda, N. R. Photothermal Release of Single-Stranded DNA from the Surface of Gold Nanoparticles Through Controlled Denaturing and Au–S Bond Breaking. *ACS Nano* **2010**, *4*, 6395–6403.

(51) Jain, P. K.; Qian, W.; El-Sayed, M. A. Ultrafast Cooling of Photoexcited Electrons in Gold Nanoparticle–Thiolated DNA Conjugates Involves the Dissociation of the Gold–Thiol Bond. *J. Am. Chem. Soc.* **2006**, *128*, 2426–2433.

(52) Dam, D. H. M.; Culver, K. S. B.; Odom, T. W. Grafting Aptamers onto Gold Nanostars Increases *in Vitro* Efficacy in a Wide Range of Cancer Cell Types. *Mol. Pharmaceutics* **2014**, *11*, 580–587.

(53) Hrelescu, C.; Stehr, J.; Ringler, M.; Sperling, R. A.; Parak, W. J.; Klar, T. A.; Feldmann, J. DNA Melting in Gold Nanostove Clusters. *J. Phys. Chem. C* **2010**, *114*, 7401–7411.

(54) Stehr, J.; Hrelescu, C.; Sperling, R. A.; Raschke, G.; Wunderlich, M.; Nichtl, A.; Heindl, D.; Kurzinger, K.; Parak, W. J.; Klar, T. A.;

Feldmann, J. Gold NanoStoves for Microsecond DNA Melting Analysis. *Nano Lett.* **2008**, *8*, 619–623.

(55) Oldenburg, S. J.; Averitt, R. D.; Westcott, S. L.; Halas, N. J. Nanoengineering of Optical Resonances. *Chem. Phys. Lett.* **1998**, *288*, 243–247.

(56) Hirsch, L. R.; Stafford, R. J.; Bankson, J. A.; Sershen, S. R.; Rivera, B.; Price, R. E.; Hazle, J. D.; Halas, N. J.; West, J. L. Nanoshell-Mediated Near-Infrared Thermal Therapy of Tumors under Magnetic Resonance Guidance. *Proc. Natl. Acad. Sci. U. S. A.* **2003**, *100*, 13549–13554.

(57) Brinson, B. E.; Lassiter, J. B.; Levin, C. S.; Bardhan, R.; Mirin, N.; Halas, N. J. Nanoshells Made Easy: Improving Au Layer Growth on Nanoparticle Surfaces. *Langmuir* **2008**, *24*, 14166–14171.

(58) Gad, S. C.; Sharp, K. L.; Montgomery, C.; Payne, J. D.; Goodrich, G. P. Evaluation of the Toxicity of Intravenous Delivery of Auroshell Particles (Gold-Silica Nanoshells). *Int. J. Toxicol.* **2012**, *31*, 584–594.

(59) Oldenburg, S. J.; Jackson, J. B.; Westcott, S. L.; Halas, N. J. Infrared Extinction Properties of Gold Nanoshells. *Appl. Phys. Lett.* **1999**, *75*, 2897–2899.

(60) Weissleder, R. A Clearer Vision for *in Vivo* Imaging. *Nat. Biotechnol.* **2001**, *19*, 316–317.

(61) Scientific Committee on Emerging and Newly Identified Health Risks. *Light Sensitivity*; Health & Consumers DG, Directorate C: Public Health and Risk Assessment; Brussels, 2008.

(62) Agudelo, D.; Bourassa, P.; Bérubé, G.; Tajmir-Riahi, H.-A. Intercalation of Antitumor Drug Doxorubicin and Its Analogue by DNA Duplex: Structural Features and Biological Implications. *Int. J. Biol. Macromol.* **2014**, *66*, 144–150.

(63) Kankia, B. I.; Buckin, V.; Bloomfield, V. A. Hexaminecobalt-(III)-Induced Condensation of Calf Thymus DNA: Circular Dichroism and Hydration Measurements. *Nucleic Acids Res.* **2001**, *29*, 2795–2801.

(64) OligoAnalyzer program; <http://www.idtdna.com/Scitools> (accessed December 22, 2015).

(65) Ayala-Orozco, C.; Urban, C.; Knight, M. W.; Urban, A. S.; Neumann, O.; Bishnoi, S. W.; Mukherjee, S.; Goodman, A. M.; Charron, H.; Mitchell, T.; Shea, M.; Roy, R.; Nanda, S.; Schiff, R.; Halas, N. J.; Joshi, A. Au Nanomatrixshells as Efficient near-Infrared Photothermal Transducers for Cancer Treatment: Benchmarking against Nanoshells. *ACS Nano* **2014**, *8*, 6372–6381.

(66) Allen, T. H.; Krzywicki, H. J.; Roberts, J. E. Density, Fat, Water and Solids in Freshly Isolated Tissues. *J. Appl. Physiol.* **1959**, *14*, 1005–1008.

(67) Simoncelli, S.; de Alwis Weerasekera, H.; Fasciani, C.; Boddy, C. N.; Aramendia, P. F.; Alarcon, E. I.; Sciaiano, J. C. Thermoplasmonic ssDNA Dynamic Release from Gold Nanoparticles Examined with Advanced Fluorescence Microscopy. *J. Phys. Chem. Lett.* **2015**, *6*, 1499–1503.

(68) Hogan, N. J.; Urban, A. S.; Ayala-Orozco, C.; Pimpinelli, A.; Nordlander, P.; Halas, N. J. Nanoparticles Heat through Light Localization. *Nano Lett.* **2014**, *14*, 4640–4645.

(69) Brongersma, M. L.; Halas, N. J.; Nordlander, P. Plasmon-Induced Hot Carrier Science and Technology. *Nat. Nanotechnol.* **2015**, *10*, 25–34.

(70) Takahashi, H.; Niidome, Y.; Yamada, S. Controlled Release of Plasmid DNA from Gold Nanorods Induced by Pulsed Near-Infrared Light. *Chem. Commun. (Cambridge, U. K.)* **2005**, 2247–2249.

(71) Chen, C.-C.; Lin, Y.; Wang, C.; Tzeng, H.; Wu, C.; Chen, Y.-C.; Chen, C.-P.; Chen, L.; Wu, Y.-C. DNA–Gold Nanorod Conjugates for Remote Control of Localized Gene Expression by Near Infrared Irradiation. *J. Am. Chem. Soc.* **2006**, *128*, 3709–3715.

(72) Aguirre, C. M.; Moran, C. E.; Young, J. F.; Halas, N. J. Laser-Induced Reshaping of Metallo-dielectric Nanoshells under Femto-second and Nanosecond Plasmon Resonant Illumination. *J. Phys. Chem. B* **2004**, *108*, 7040–7045.

(73) Petrova, H.; Juste, J. P.; Pastoriza-Santos, I.; Hartland, G. V.; Liz-Marzan, L. M.; Mulvaney, P. On the Temperature Stability of Gold

Nanorods: Comparison between Thermal and Ultrafast Laser-Induced Heating. *Phys. Chem. Chem. Phys.* **2006**, 8, 814–821.

(74) Alkilany, A. M.; Murphy, C. J. Toxicity and Cellular Uptake of Gold Nanoparticles: What We Have Learned so Far? *J. Nanopart. Res.* **2010**, 12, 2313–2333.